The Dissertation Committee for Boxue Chen Certifies that this is the approved version of the following Dissertation:

Electrically Active Microfluidic Fibers

Committee:

Zheng Wang, Supervisor

Edward T Yu

Paul S Ho

Nanshu Lu

Yuebing Zheng

Electrically Active Microfluidic Fibers

by

Boxue Chen

Dissertation

Presented to the Faculty of the Graduate School of

The University of Texas at Austin

in Partial Fulfillment

of the Requirements

for the Degree of

Doctor of Philosophy

The University of Texas at Austin

May 2019

Dedication

To my mom, 张冬梅,

who once told me to think not if I deserve more, but if I can contribute more.

To my dad, 陈绪学,

who once told me that never hesitate to go far away,

beyond all mountains, all seas, and all countries.

Acknowledgements

Many years later, as I read this dissertation on a rainy afternoon, I am to remember that distant morning when my advisor, Professor Zheng Wang, interviewed me for graduate school admission. I first met Dr. Wang during that interview – a surprisingly caring man who told me no need to be nervous, and allowed me join his research lab at the beginning of the interview. Throughout the years, Dr. Wang has successfully directed me to view curiosity as the catalyst for my research. He has gone above and beyond to ensure that I have all the freedom to explore the joy and enthusiasm in academic world. And not only academic advising, I also deeply appreciate his tremendous help with my English, his continuous financial aid, and his valuable suggestions for my career.

I would also like to acknowledge my thesis committee, Prof. Edward Yu, Prof. Paul Ho, Prof. Nanshu Lu and Prof. Yuebing Zheng, for their support. I did my first teaching assistant under Professor Edward Yu for EE302, right after I came to US. It was a memorable experience of working with him and being immersed with hundreds of undergrads for over ten hours per week. I took two courses with Professor Paul Ho. He is the most humble professor I ever met, and I absolutely enjoyed every conversation we shared. I would also like to offer my special thanks to all of the staff in the ECE department and the Microelectronics Research Center, particularly Christine Wood and Melanie Gulick, for their enormous patience and invaluable help.

As the most-junior graduate student in LAND group, I have been fortunate to receive immense guidance and endless support from my highly talented colleagues. I cannot imagine completing this dissertation without you people. I am deeply grateful for those good old days that I spent together with Thien-An Nguyen and Ryan Cho in the

windowless fiber-drawing lab. Both of them quickly became lifelong friends and together we shared those reckless nights on gaming, camping, climbing and drinking. I am indebted to Dr. Hossein Mousavi, Dr. Ian Williamson, Dr. Hui Dong, and Dr. Danlu Wang for their valuable discussions, feedbacks and helps with COMSOL. They have perfectly demonstrated to me the benefits we receive from sharing our knowledge. As I had been guided, I was ready, excited and willing when given the opportunity to support my mentees, Ammar Hazim and Corey Kwok. Their diligence and hard work have become a great inspiration to me.

During this long journey, I had three internships with KLA, a place where I found great passion and accomplishments. Alexander Kuznetsov is the nicest manager I could ever ask for. My deepest appreciation goes to him for his suggestions to my career and his help to convert my internship work into a patent application. Thank you to Andrei Veldman for all the technical and non-technical advices I received from you. Thank you to Lu Yu for a wonderful experience under your mentorship in China. Thank you to Antonio Gellineau for giving me extreme flexibility in choosing my internship project and your continuous support after the internship. I look forward to working with you after graduation.

These past couple of years have not been the easiest. Throughout the years, I have greatly benefited from my friends. Special thanks to Bob and Diana Christensen. They are my first friends since I came to US, who are always willing to listen to me even before I can fluently speak English. Thank you to my roommates Joseph Adams and Jason Mendiola. I will remember all the moments we had together at Tigeress. Thank you to Zongyao Li for sharing so many wonderful trips with me. A shout out to my good friends Qi Ren, Peipei Zhang, Wei Yang, Hualing Zhang, Ziyuan Wang, Shiyang Wang, Neelam Agarwal, Jian Feng, Bing Ai, Hai Yan, Nish Nookala, Divya Kadiyala, KT Ho, Joseph

Nguyen, Jason Lii, Max Haroutunian, Wenjing Zhan, Weigu Li, Feng Wen, Zhicheng Xiao, Yingnan Liu, Yifan Jiang, and everyone else that I've forgotten to mention here.

Finally yet importantly, I must acknowledge my family for their unconditional love and countless encouragements. To my cousin Yandong Chen, thank you for always picking me up from the airport and never forgetting to drop me off later. To my cousin Yun Zhang, thank you for always being willing to talk to me and to encourage me over the phone. Special thanks to my dear girlfriend Wei Sun, who has been patiently listening to my endless complaints and annoyances and keeps supporting me through the toughest times. Meeting you is one of the best things that ever happened in my life. At the end, I owe my deepest gratitude to my greatest parents. I have been blessed beyond all measure that I have you both to depend on. I hope that a PhD degree could serve as testament to the considerable time and effort my parents have put into raising me.

Abstract

Electrically Active Microfluidic Fibers

Boxue Chen, Ph.D.

The University of Texas at Austin, 2019

Supervisor: Zheng Wang

In recent years, novel materials processing techniques involving PDMS and paper materials have enabled revolutionary progress in performance and capability of chip-scale microfluidics. However, microfluidic systems remain largely single-chip constructs, and are far from the level of sophistication that is typically seen in multi-chip multi-board electronic systems. A major limitation lies in the fluidic chip-to-chip interconnects, where the simple tubing materials and structures lack the pumping and monitoring functionalities that are needed in reliable microfluidic systems.

In this dissertation, we address these challenges with the new structures and materials made available by multimaterial fiber processes, which have recently emerged as a materials platform for a variety of sensing modalities. Various functionalities, such as flow actuators or sensors, are integrated into multimaterial fibers for functional chip feedlines.

Integrated fiber pumps are enabled by electrowetting-on-dielectric (EWOD) actuation to precisely manipulate liquid flow. Fiber drawing process allows creating an ultra-thin and uniform dielectric layer, and hence achieving rapid flow response and predictable flow behaviors. Fiber thermal flow sensors, on the other hand, take the

advantage of ultra-fast heat transfer at microscale to break the fundamental trade-off between sensitivity, pressure drop, measurement range, and temperature rise in conventional thermal flow sensors. Record-setting flowrate sensitivity was demonstrated over a wide measurement range and unprecedentedly low pressure drop. As a natural extension to the project of fiber flow sensors, we also present the theoretic optimization of geometric and segmentation design of fiber flow sensors to further boost sensitivity and extend measurement range. A new two-segment structure was demonstrated in simulation with greatly extended measurement range and much simpler post-drawing process. At last, we proposed a general strategy for distributed sensing, which was later applied to present distributed flow sensors. Sub-cm spatial resolution was demonstrated in simulations.

Taken as a whole, electrically active microfluidic fibers take advantage of novel materials and new device structures that deliver new functionality and significant improvements in performance. This unconventional form of devices paves the way towards a complete functional overhaul of microfluidics feed lines needed in large-scale multi-chip integration in microfluidics and opens new possibilities in lab-on-fiber technologies.

Table of Contents

List of Tables xv

List of Figures xvi

Chapter 1: Introduction 1

Chapter 2: Device Fabrication 4

2.1 Geometric Design and Material Selection 4

2.2 Preform Assembly and Thermal Drawing Process 5

2.3 Post-drawing Process 7

2.3.1 Process for lengthwise conductive characteristics 7

2.3.2 Process for crosswise capacitive characteristics 8

2.4 Device Characterization 9

2.4.1 Cross-section geometry 9

2.4.2 Channel flow resistance 9

2.4.3 Lengthwise conductance and its dependence on temperature 12

2.4.4 Crosswise capacitance and its dependence on water-column-length 14

Chapter 3: Fiber Pumps 16

3.1 Motivation of Fiber Pumps 16

3.2 Mechanisms of EWOD Actuation 17

3.2.1 Thermodynamic approach 17

3.2.2 Electromechanical approach 18

3.3 Available Force of EWOD Actuation 20

3.3.1 Circuit model of fiber pumps 20

3.3.2 Estimation of pumping force 24

3.4 Bi-directional Flow Control 25
3.4.1 Test setup for fiber pumps demonstration 25
3.4.2 Image processing in MATLAB 26
3.4.3 Demonstration of bi-directional flow control 32
3.5 Predictable Flow Behaviors 33
3.5.1 Flow dynamics model for liquid pumping 33
3.5.2 Discussions on liquid pumping curves at 300 V 35
3.5.3 Discussions on liquid pumping curves at various voltages 36
3.5.4 Operation regimes of fiber pumps 38
Chapter 4: Fiber Flow Sensors 40
4.1 Motivation of Fiber Pumps 40
4.2 Mechanisms of Thermal Flow Sensors 41
4.2.1 Thermal flow sensors and their typical response 41
4.2.2 Inherent trade-off among sensitivity, pressure drop and measurement range 43
4.3 Benefits of New Thermistor Material: CPE 45
4.4 Demonstration of Flow Monitoring 47
4.4.1 Test setup for fiber flow sensors demonstration 47
4.4.2 Measurement uncertainty 48
4.4.3 Response of fiber flow sensors 49
4.5 First-order Temperature Response Theory 50
4.5.1 Temperature response of a single-segment sensor 50
4.5.2 Temperature response of a multi-segment sensor 55
4.6 Finite Element Simulations 58

4.6.1 Simulation setup for a multi-segment sensor.....58
4.6.2 Predicted temperature distribution of a multi-segment sensor 59
4.6.3 Match between FEM and first-order theory 60
4.7 Demonstration of Multi-segment Flow Sensors 61
4.7.1 Device preparation and test condition 61
4.7.2 Responses of multi-segment flow sensors 61
Chapter 5: Optimization of Fiber Flow Sensors 66
5.1 Motivation of Optimization 66
5.2 Cross-sectional Design 68
5.2.1 Design guideline from analytic model.....68
5.2.2 Match between FEM and analytical guideline 72
5.2.3 Optimized design for cross-sectional geometry.....75
5.3 Longitudinal Design 76
5.3.1 Extended first-order temperature response theory.....77
5.3.2 FEM simulations at various segment lengths 80
5.4 Novel Multi-segment Structures.....82
5.4.1 Design of two-segment sensors 82
5.4.2 First-order temperature response theory for a two-segment sensor.....85
5.4.3 Effective length of preheating segment 88
5.4.4 Two-segment sensors with a constant temperature heater.....93
5.5 Unification of Two Temperature Distribution Theories.....95
Chapter 6: Distributed Fiber Sensors.....100
6.1 Motivation of Distributed Sensors.....100

6.1.1 Limitations of Optical Distributed Sensors 100
6.1.2 Previous work on electrical fiber sensing Over Large Area 101
6.2 Mechanisms of Fiber Distributed Sensors 103
6.2.1 Fundamental requirements of distributed sensing 103
6.2.2 Microfluidics-enabled fiber distributed sensors 104
6.2.3 Potential fiber distributed sensors and their applications 105
6.3 Electrical Current Profile of Distributed Flow Sensors 106
6.3.1 Lumped-element circuit model 107
6.3.2 First-order current distribution theory 108
6.3.3 Current distribution claculated from FEM.....111
6.3.4 Spatial resolution of fiber distributed sensors.....113
6.4 Demonstration of Distributed Fiber Flow Sensors in Simulations 115
6.4.1 Simulation Setup.....116
6.4.2 Responses of distributed sensors to flow rate 117
6.4.3 Responses of distributed sensors to droplet locations 118
6.4.4 Demonstration of scanning flowrate distribution 120
Chapter 7: Conclusion.....124
7.1 Summary.....124
7.2 Future Work.....126
7.2.1 Low voltage actuated fiber pumps.....126
7.2.2 Droplet-based flow injection with fiber pumps 126
7.2.3 Demonstration of two-segment flow sensors in experiments.....128
7.2.4 Demonstration of distributed flow sensors in experiments 128

7.2.5 Other forms of distributed sensors.....128
7.2.6 Alternative methods of breaking axial uniformity.....129
7.3 Final Remarks.....130
References.....131

List of Tables

Table 2.1. Comparison of flow resistance and sensitivity among typical flow sensors. 12

Table 3.1. Descriptions and estimates for various components in cross-sectional circuit models. 21

Table 3.2. Estimates and fitted values for effective resistance and capacitance. 24

Table 4.1. Average sensitivity of anemometers in various response regions. 45

Table 5.1. Parameter spaces for FEM simulations at various channel geometries. 72

Table 5.2. Parameter spaces for FEM simulations at various cladding geometries 73

Table 5.3. Original device parameters in FEM simulations and fitted parameters with analytic model. 88

Table 5.4. Measurement ranges of fiber sensors with constant temperature pre-heater at various temperatures from 0 to 60 ^{o}C 95

Table 5.5. Description of temperature distribution model for a long single-segment sensor. 96

Table 5.6. Description of temperature distribution model for a preheating segment. ... 97

List of Figures

Figure 2.1. Schematic view of the fiber cross section. 5

Figure 2.2. Schematics of preform assembly and fiber thermal drawing. 6

Figure 2.3. Post-drawing process for lengthwise conductive characteristics. 8

Figure 2.4. Post-drawing process for crosswise capacitive characteristics. 8

Figure 2.5. Cross-section geometry of an as-drawn fiber. Left panel: optical image of a fiber segment with a US quarter. Right panel: optical micrograph of the cross section of a fiber. 9

Figure 2.6. (a) Gravity-driven flow through the device under test. (b) Two devices under test: (top panel) a 7-cm-long Tygon tube, and (bottom panel) a 5-cm-long fiber segment connected with two 1-cm-long Tygon tubes. 11

Figure 2.7. Measured time-evolution of liquid level (colored) with corresponding fitting curves (black). Inset shows the fitted time constants for each run. 12

Figure 2.8. Measured (colored dots) and fitted (blue line) relative electrical resistance of CPE films at various temperatures. 14

Figure 2.9. Magnitude of impedance of a fiber segment filled with various water-column-length. Inset shows the derived capacitance as a function of water-column-length. 15

Figure 3.1. Schematics for the mechanism of EWOD actuation. 18

Figure 3.2. Schematics for inserting metal plate into a parallel plate capacitor. 19

Figure 3.3. Non-uniform distribution of stress tensor around half-inserted metal plate. 19

Figure 3.4. Cross-sectional circuit model of air (left panel) and water (right panel) filled fiber pumps. 21

Figure 3.5. (top panel) Schematic of fiber segment 50% filled with water; (middle panel) corresponding simplified circuit model; (bottom panel) a photograph of fiber segment 50% filled with water (yellow, color from Fluorescein Sodium soluble dye).....23
Figure 3.6. (a) Measured and (b) fitted impedance of fiber pumps filled with various amount of water. 24
Figure 3.7. Schematic view of test setup for fiber pumps demonstration. 26
Figure 3.8. Acquired images showing water/liquid interface at various locations. 26
Figure 3.9. Signal conditioning for image processing in MATLAB.....27
Figure 3.10. Five hundred of examples of 1D array signal with edge aligned to the center. 28
Figure 3.11. (top panel) An example of DoB filter for the case of k=3 and i=8; (bottom left panel) response of such DoB filter to an edge; (bottom right panel) response of such DoB filter to random noise. 29
Figure 3.12. Frequency response of a DoB filter with a window size of 7 pixels. 30
Figure 3.13. Designed band-stop FIR filter (left panel) and signal before and after filtered (right panel). 30
Figure 3.14. Nosie floor before (left panel) and after (right panel) applying band-stop FIR filter.....31
Figure 3.15. Time-lapse photographs of fiber pumping at 1-minute interval (upper panel) and extracted position of air/liquid interface at 2-second interval (lower panel). 32
Figure 3.16. Initialization and finalization sections of (a) a syringe pump and (b) a fiber pump. 33
Figure 3.17. Liquid pumping curves with different parameters. 35

Figure 3.18. Measured (dots) and fitted (line) liquid pumping curves using derived flow dynamics model. 35
Figure 3.19. Measured (dots) and corresponding fitted (lines) liquid pumping curves at different voltage 36
Figure 3.20. Initial pumping velocities at 0 mm as a function of voltage square. Red triangle symbol indicates unsteady pumping, as detailed in the inset figure. 37
Figure 3.21. Operation regimes of fiber pumps. 39
Figure 4.1. Schematics for the mechanism of thermal flow sensors. 42
Figure 4.2. Typical responses of two thermal flow sensors: (left panel) anemometers; (right panel) calorimetric flow sensors. 43
Figure 4.3. (left panel) Two conductivity mechanisms of CPE: physical contact (blue path) and tunneling (orange path); (right panel) relative change of resistivity as respect to temperature change for CPE and several metal films. 47
Figure 4.4. Schematic view of test setup for fiber flow sensors demonstration....48
Figure 4.5. Temperature (left panel) and voltage (right panel) responses of fiber flow sensors. 49
Figure 4.6. Two paths of heat conductive dissipation: through PC cladding (green arrows) and through liquid inside of fluidic channel (purple arrow). 52
Figure 4.7. Large heat loss at the contact regions. 58
Figure 4.8. Calculated temperature distribution along the length of a multi-segment fiber sensor at various flow rates using a finite-element solver....59

Figure 4.9. Calculated hot-film temperature from the finite-element solver (colored curves) and the analytical polynomial response from Equation 4 (grey curves) at various flow rates. The yellow areas denote Segment #2, #4, #6 and #8. 60
Figure 4.10. Schematic (top panel) and photograph (bottom panel) of an eight-segment sensor. 61
Figure 4.11. Temperature (left panel) and voltage (right panel) responses (dots) of multi-segment flow sensors in good agreement with FEM calculation (curves). 62
Figure 4.12. Measured temperature responses (dots) in low flow rate region in good agreement with the 1d analytical heat transfer theory. Inset compares the fitted effective segment index and the physical segment index. 63
Figure 5.1. Current (left panel) and optimized (right panel) of the temperature responses of each segment in a multi-segment sensor. 67
Figure 5.2. Current (left panel) and optimized (right panel) configuration of a multi-segment sensor. 67
Figure 5.3. Parameters to be optimized in cross-sectional design. 68
Figure 5.4. Two paths of conductive heat loss: cross-sectional heat loss (red arrow) and axial heat loss (purple arrow). 69
Figure 5.5. Hot zone (pattern-filled region) for cross sections with (left and right) and without (middle) thin cladding. The formulas on the top represent the corresponding cross-sectional heat loss. 71
Figure 5.6. Dependence of the reciprocal of sensitivity on channel geometries simulated with a FEM solver. 73
Figure 5.7. Dependence of 1/*S* on cladding geometries simulated with a FEM solver... 74

Figure 5.8. Sensitivity (blue line) and pressure drop (red line) of fiber flow sensors at various aspect ratios. 75
Figure 5.9. (a) Optimized cross sectional geometry and (b) corresponding temperature distribution at zero flow. 76
Figure 5.10. Mathematically treat a single segment as *N* segments. 77
Figure 5.11. Temperature response of a single-segment sensor with original (blue line) and extended model (red line). 78
Figure 5.12. Current distribution for sensors of various length. 79
Figure 5.13. Average current amount passing through fluidic channel region at various segment length. 80
Figure 5.14. Dependence of the reciprocal of sensitivity on segment length simulated with a FEM solver. 81
Figure 5.15. (a) Temperature responses and (b) sensitivity of nominal design (blue line) and optimized design (red line). 81
Figure 5.16. Schematic of a two-segment sensor. 83
Figure 5.17. Temperature responses of two-segment flow sensors at various fraction of current passing through an 8-mm-long pre-heating segment. 84
Figure 5.18. Temperature responses of two-segment flow sensors at various preheating segments with maximum possible fraction of current passing though the pre-heating segments. 85
Figure 5.19. Simulated (dots) and fitted (lines) temperature responses of a two-segment sensor. 87
Figure 5.20. Heat generation and dissipation for an infinitesimal segment. 89
Figure 5.21. Heat generation and dissipation at the boundary. 90

Figure 5.22. (top panel) Temperature distribution on the surface of an 8-mm-long preheating segment at zero flow. (bottom panel) a cutline plot of the 2D temperature distribution with its fitted curve. 91
Figure 5.23. Schematics of a two-segment sensor with a constant temperature heater. ... 93
Figure 5.24. Temperature responses of fiber sensors without pre-heater (blue line), with fiber segment as pre-heater (red line), and with constant temperature pre-heater (green line). 94
Figure 5.25. Temperature responses of fiber sensors with constant temperature pre-heater at various temperatures from 0 to 60 ^{o}C. 95
Figure 6.1. Schematics of a general fiber distributed sensor. 105
Figure 6.2. Schematics of cross sectional geometry for fiber distributed sensors. 107
Figure 6.3. Lumped-element circuit model for fiber distributed sensors 108
Figure 6.4. Illustrations for first-model current flow model. 109
Figure 6.5. Diagram for the method of image current sources. 110
Figure 6.6. Current disstributions of distributed fiber flow sensors. 112
Figure 6.7. Simulated (dots) and fitted (lines) current disstribution at CPE/metal interface 113
Figure 6.8. Simulation setup for step response of fiber distributed sensors. 114
Figure 6.9. Step response of fiber distributed sensors. 115
Figure 6.10. Geometry setup for the demonstration of fiber distributed sensors. 117
Figure 6.11. Temperature (a) and voltage (b) responses of fiber distributed sensors. 118
Figure 6.12. Temperature (a) and voltage (b) responses of fiber distributed sensors with droplet located at various locations. 119
Figure 6.13. Dependence of nominal resistance on droplet location for (a) a 2-cm-long segment and (b, c) a 6-cm-long segment. 120

Figure 6.14. Simulation setup for scanning flowrate distribution. 121
Figure 6.15. Measured (a) temperate and (b) voltage responses when scanning a laminar flow profile. 122
Figure 6.16. Original flow profile (red line) and reconstructed flow profile (circles) from measured temperature (left) and voltage (right) responses. 122
Figure 7.1. Electrically active microfluidic fibers as the marriage of multimaterial fibers and microfluidics. 124
Figure 7.2. Configuration of droplet-based flow injection. 127
Figure 7.3. Alternative configuration of droplet-based flow injection. 128

Chapter 1: Introduction

Microfluidics technology modulates fluids in microscale. Its popularity in life science and chemistry synthesis benefits from its precise control of liquid down to picoliter level, as well as fast heat/mass transfer within sub-mm length. [1], [2] The complexity and functionality of microfluidic systems has grown from miniaturized biochemical analysis on a single chip to multi-chip systems that can perform high-speed genetic analysis of billions of base pairs in hours. [3], [4] However, chip-to-chip and chip-to-world interconnects remain simple today, i.e. plastic tubing, due to its very different processing techniques, materials properties and insufficient knowledge of melt-processed electronics.

To address those challenges, we explore new materials and novel device structures made available by multimaterial fiber technology [5]–[7], which has recently emerged as a materials platform for a variety of sensors and actuators for light [8]–[11], heat [12], and sound [13], [14]. We take advantage of the exceptional aspect ratios and the ability of integrating flexible electronics of this process, to create kilometers of hollow fibers with various in-line sensing and actuating modalities for functional microfluidic interconnects.

This dissertation is constructed around electrically active microfluidic fibers, a hybrid technology that marries the best from both microfluidics and multimaterial fibers. We describe the design, simulation and implementation of a series of microfluidic fiber devices, enabling in-line pumping and monitoring functionalities that are needed in large-scale integration of microfluidics systems. Particularly, our work seeks to answer a few questions around this technology, either independently or simultaneously:

- Can microfluidic fibers form a closed-loop flow control system, i.e. a system consists of active flow controllers and flow monitors?

- Can devices made with microfluidic fibers outperform state-of-the-art commercial sensors/actuators?
- Can microfluidic fibers, as a hybrid technology, marry the benefits from both microfluidics and multimaterial fibers?
- Can microfluidic fibers, as a novel technology, offer new opportunities for sensing/actuating modalities that do not exist before?

Specifically, this thesis is organized as follows.

In Chapter 2[1], we present the design, fabrication and characterization of such microfluidic fibers.

In Chapter 3, we demonstrate the first implementation of active pumping functionality within a flexible fiber that is enabled by electrowetting-on-dielectric (EWOD) actuation to precisely manipulate liquid flow. We take this EWOD approach and show rapid flow response and predictable flow behaviors with integrated fiber pumps

In Chapter 4[1], we report the first fiber flow-rate sensor using unconventional thermistor materials and novel multi-segment structures. In addition to the integrated flow-sensing capability, we also show how our device platform resolves a fundamental trade-off between sensitivity, pressure drop, measurement range, and temperature rise in conventional thermal flow sensors.

In Chapter 5, we present the systematic optimization of fiber flow sensors with FEM simulations. We conduct a series of simulations to investigate the geometric effects on sensitivity. We also demonstrate a novel two-segment device structure, which achieves greatly extended measurement range with much simplified post-drawing processing.

[1] Part of the content of this chapter has previously been published as *"Integrated Fiber Flow Sensors for Microfluidic Interconnects." Advanced Materials Technologies 3.11 (2018): 1800175.*[15]

In Chapter 6, we demonstrate the first implementation of electrically active distributed sensors that are enabled by a moving droplet to locally active fiber devices. We apply this approach to fiber flow sensors, and show sub-mm level spatial resolution, as well as a complete flow velocity profiling.

Chapter 2: Device Fabrication

In this chapter[2], we describe the design and fabrication of multimaterial fiber electronics, which are later used as microfluidic interconnects. We start with the geometric design of such fiber devices and material selection. Then we present the entire fabrication process, consisting of preform assembly, thermal co-drawing and post-drawing processes. At the end, a few of characterization methods are also investigated.

2.1 Geometric Design and Material Selection

Figure 2.1 shows the basic structure of a fiber electronic device, which was produced using a thermal co-drawing process. Thanks to the exceptional aspect ratios [16], [17] and dimensional control [18] of this processing technique, we placed two extraordinarily long and thin conductive films (yellow color) adjacent to a hollow fiber core that serves as the fluid channel. We choosed carbon-black doped polyethylene (CPE) as the material for this conductive layer not only because of its moderate resistivity of 0.3~0.5 Ω·m, but also its exceptional temperature coefficient of resistivity (TCR) of 0.091 K^{-1}. Comparing to metal films, CPE films provide ~10^7 times greater nominal resistivity at room temperature, and ~20 times greater TCR, thanks to their percolation effect [19], [20].

[2] Part of the content of this chapter has previously been published as *Chen, Boxue, Corey Kwok, Thien-An Ngoc Nguyen, and Zheng Wang. "Integrated Fiber Flow Sensors for Microfluidic Interconnects." Advanced Materials Technologies 3.11 (2018): 1800175.*[15] Co-authors have participated extensively in experiment methods, and have contributed in reviewing the final manuscript.

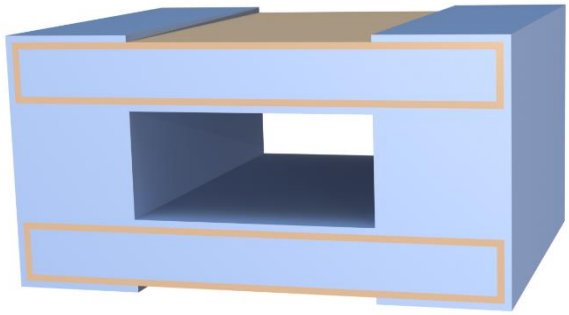

Figure 2.1. Schematic view of the fiber cross section.

The polymer films are electrically insulated from the fluid channel by a thin dielectric layer of polyethylene. Here polyethylene provides excellent compatibility with CPE, and hydrophobic surface as well. Polycarbonate was utilized as the cladding material to provide mechanical support and flexibility. Such fiber devices exhibit conductive characteristics along the length, thanks to CPE, as well as crosswise capacitive characteristics due to its structure of parallel plate capacitor.

Fiber co-drawing process allows to create kilometers of uniform fibers at a cross-section of sub-mm scale, despite that the devices are originally assembled at macroscopic scale. We adopted fiber fluidic channels with a cross-section of 1×0.5 mm with an overall fiber cross-section of 2×1 mm, to match the commonly used 1/16" ID Tygon tube. The relatively large cross section reduces the pressure drop to levels typical in feedlines of microfluidic systems, estimated to be 1.25×10^{11} kg/m^{5}s in hydrodynamic resistance [21].

2.2 Preform Assembly and Thermal Drawing Process

Figure 2.2 shows the schematic view of preform assembly and thermal drawing process. The fiber preform (23 cm x 3.8 cm x 1.9 cm) was assembled from three polycarbonate (PC, McMaster-Carr 1749K229) plates. The top and bottom PC plates were

wrapped with 500-μm-thick carbon-black-doped polyethylene (CPE, Hillas Blac-STAT conductive films) films. The middle plate was machined with a 19 mm wide through slot using CNC mill (XIMotion EC-2), which will serve as fluid channel after thermal drawing.

An 80-μm-thick polyethylene (PE, Elkay Plastics) sheet was put between fluid channel and CPE films. Two sacrificial strips of polyimide (PI, McMaster-Carr 7648A42) sheets were added on the middle of both the top and bottom surface of the assembled preform. A polycarbonate (Ajedium Films 09105-1) sheet (0.08 mm thick) was rolled around the assembled preform to hold it tight.

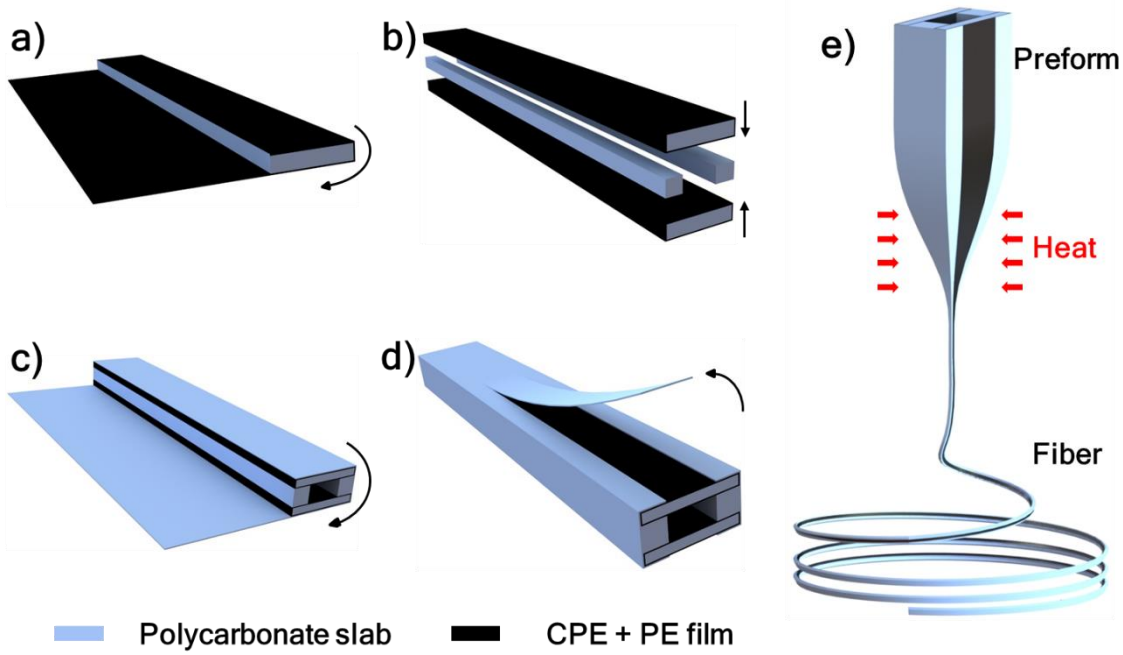

Figure 2.2. Schematics of preform assembly and fiber thermal drawing.

Assembled preform was consolidated at 160 ^{o}C for 300 minutes in a vacuum oven (Fisher Scientific Isotemp 282A) at a pressure less than 1 kPa. Two rectangular windows were created by cutting open the outermost PC sheet along the previously buried polyimide

strips (see Figure 2.2d for details). Exposed polyimide strips were also removed to uncover CPE films for connecting to external contacts.

Subsequently, consolidated preform was feed into a three-zone vertical furnace to be drawn into hundreds of meters of fibers. The temperature of furnace was set to be 150 ^{o}C (top), 290 ^{o}C (middle), and 30 ^{o}C (bootom). We adopted a 20x reduction ratio, which yields fibers with a cross-section of 2x1 mm, fluid channels of 1x0.5 mm, CPE films of 25 μm thick and dielectric layer of 3.8 μm thick.

2.3 POST-DRAWING PROCESS

As-drawn fibers cannot form good electrical contacts with external circuits due to the poor conductivity of CPE. Therefore post-drawing process is necessary. As we have mentioned earlier, our fiber devices exhibit resistive characteristics along the length, as well as crosswise capacitive characteristics due to its structure of parallel plate capacitor. Two different post-drawing processes can be applied depend on the applications.

2.3.1 Process for lengthwise conductive characteristics

An active conductive region were created from a uniform fiber by constructing two or multiple external contacts. Figure 2.3e shows an example of two external contacts that bracket the active region in between. At each contact (Figure 2.3c), we removed the exposed CPE on the bottom surface of fiber and coated all four external surfaces with silver paint (SPI Supplies 04998-AB). As a result, only the top CPE film forms electric connections with silver paint. At the active conductive region (Figure 2.3d), exposed CPE films were carefully removed from the top surface and two side surfaces with a blade. Consequently, electrical current in the active region is focused on the top CPE film adjacent to the fluid channel, and no current passes through the lower CPE film.

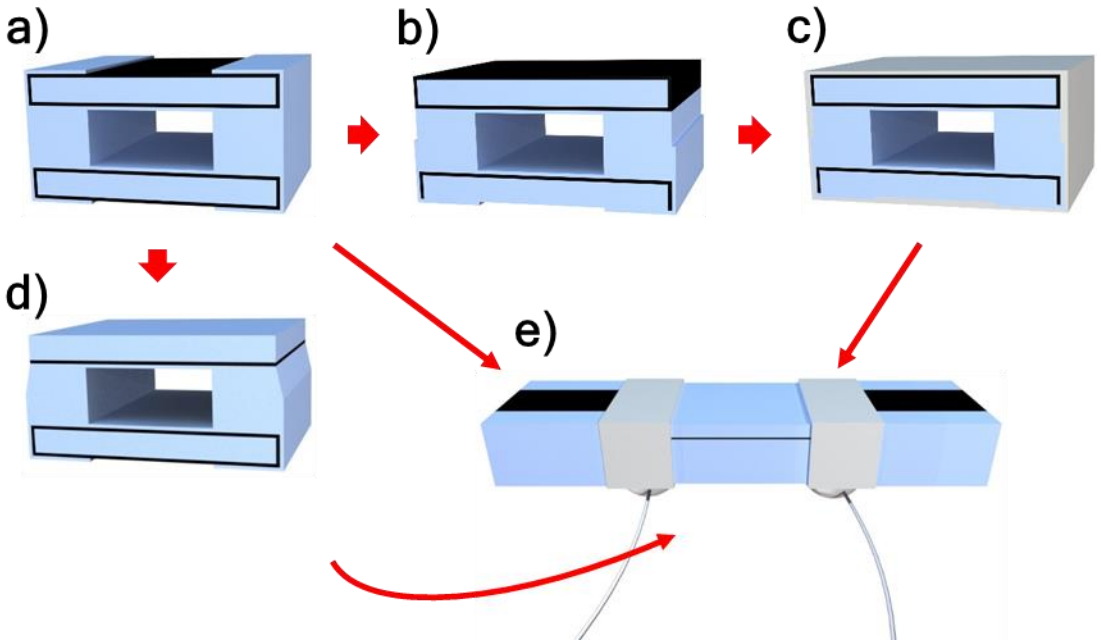

Figure 2.3. Post-drawing process for lengthwise conductive characteristics.

2.3.2 Process for crosswise capacitive characteristics

An active capacitive region were created by simply painting the top and bottom CPE film with silver paint (SPI Supplies 04998-AB).Figure 2.4 shows an example of created fiber capacitor with partially filled water. The overall capacitance equals the sum of filled region and unfilled region.

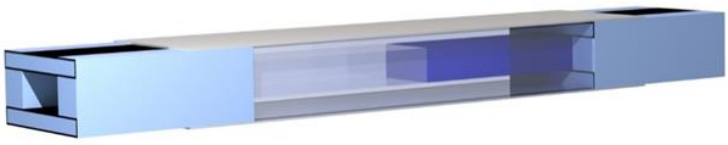

Figure 2.4. Post-drawing process for crosswise capacitive characteristics.

2.4 Device Characterization

2.4.1 Cross-section geometry

Previously, we decided to adopt a 20x reduction ratio to create fiber fluidic channels of 1×0.5 mm for a low flow resistance that is comparable with widely used 1/16”-ID Tygon tubing. The overall fiber sizes of 2×1 mm also make it easy to mount to the tubing. In Figure 2.5, we show an optical micrograph of the cross section of an as-drawn fiber, with minimal rounding at the edges. The cross-sectional dimensions of fiber and channel are very close to designed values.

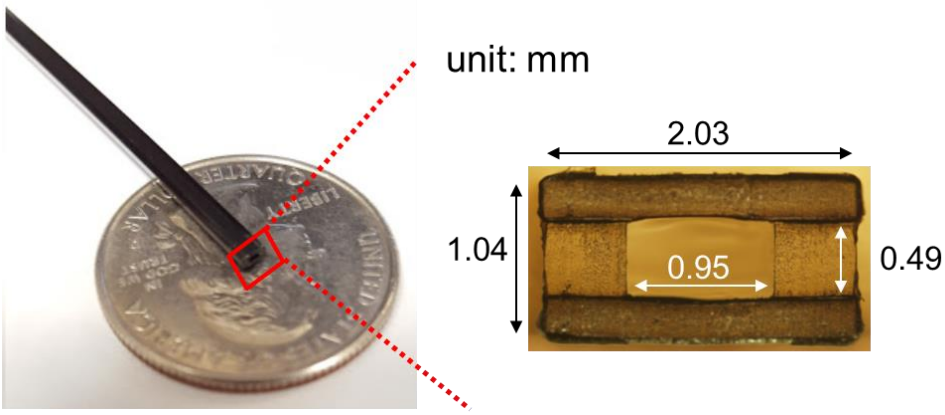

Figure 2.5. Cross-section geometry of an as-drawn fiber. Left panel: optical image of a fiber segment with a US quarter. Right panel: optical micrograph of the cross section of a fiber.

2.4.2 Channel flow resistance

For a rectangular channel of width w and height h ($w > h$), the flow resistance R can be calculated based on the following equation: [21]

$$R = \frac{12\mu L}{wh^3\left(1 - \frac{0.63h}{w}\right)} \quad (2.1)$$

,where μ is fluidic viscosity and L is length of the channel. Therefore, the flow resistance for a 1-cm-long fiber segment is estimated to be 1.25×10^9 kg/m^{4}s.

To verify this estimate, we conducted measurements of channel flow resistance based on Hagen-Poiseuille equation, which describes the linear relationship between pressure drop ΔP and volumetric flow rate Q:

$$\Delta P = R \cdot Q \tag{2.2}$$

For gravity-driven flow, pressure drop ΔP equals hydrostatic pressure $\rho g \Delta h$ caused by the weight of a fluid. ρ is the density of the fluid, and g is the gravitational acceleration constant. Δh is the height difference at two open ends of a flow system. Volumetric flow rate Q equals the product of cross-sectional area A of a container and the rate of change in liquid level h. Thus we arrive at:

$$\rho g \Delta h = -RA \cdot \frac{\mathrm{d}h}{\mathrm{d}t} \tag{2.3}$$

Integrate both sides of the equation above with respect to time t, water level can be rewritten as a function of time.

$$h(t) = c_0 + c_1 \cdot \exp\left(-\frac{2\rho g}{RA} \cdot t\right) \tag{2.4}$$

By continuously recording the liquid level at various time and fitting recorded results to the above equation, we can extract the flow resistance R.

Experimental setup (Figure 2.6a) involves two open containers, both with a cross-section of 10 x 10 cm, connected by the device under test (DUT). The time-evolution of liquid level was recorded using a digital camera (Canon T2i). Two flow channels were characterized: a 7-cm-long Tygon tube with 1/16” ID and 3/32” OD, and a 5-cm-long fiber segment connected to two 1-cm-long Tygon tube.

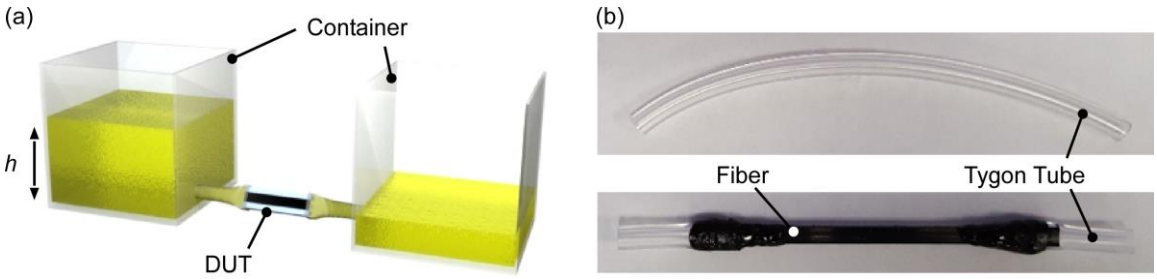

Figure 2.6. (a) Gravity-driven flow through the device under test. (b) Two devices under test: (top panel) a 7-cm-long Tygon tube, and (bottom panel) a 5-cm-long fiber segment connected with two 1-cm-long Tygon tubes.

The measurement started with the left container partially filled and the right container empty. Deionized water labelled with yellow soluble dye (Fluorescein sodium, Sigma Aldrich) freely flowed through DUT into the right container. The time-evolution of liquid level in left container *h(t)* was captured at 2 second intervals.

Figure 2.7 shows the measured time-evolution of liquid level for three runs conducted on fiber segment, and their fit to an exponential function $h(t) = c_0 + c_1 \cdot e^{-\frac{t}{\tau}}$. The near-perfect match between experimental results and fitting results is reflected by a R^2 value of greater than 0.999 and a RMSE value of less than 0.07 mm. Subsequently, the averaged time constant for a packaged fiber flow sensor (including two 1-cm-long connector tubes) is determined to be 2660 s, corresponding to a hydrodynamic resistance of 5.21×10^9 kg/(m^4·s), close to the estimate calculated from the channel geometry 6.35×10^9 kg/(m4·s).

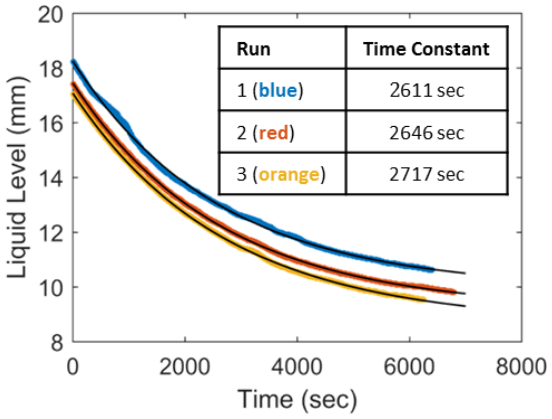

Figure 2.7. Measured time-evolution of liquid level (colored) with corresponding fitting curves (black). Inset shows the fitted time constants for each run.

Table 2.1 compares the flow resistance and the voltage sensitivity of our fiber sensor with a state-of-the-art commercial sensor (Sensirion LG 16-0430), as well as a typical MEMs sensor in recent research work [22]. As we can see, fiber sensors undoubtedly surpass the state-of-the-art industry standards as they exhibit 10 times greater sensitivity at only less than 10% pressure drop.

Table 2.1. Comparison of flow resistance and sensitivity among typical flow sensors.

	Estimated Flow Resistance	Measured Flow Resistance	Pressure Drop at 100 μL/min	Sensitivity (mV/(μL/min))
Tygon tube	4.00×10^{8} kg/(m^4·s)	8.93×10^{8} kg/(m^4·s)	1.49 Pa	--
Fiber segment	6.35×10^{9} kg/(m^4·s)	5.21×10^{9} kg/(m^4·s)	8.68 Pa	384
Sensirion LG 16-0430	--	--	125 Pa	30
PMMA channel in a MEMs flow sensor [22]	--	--	150 Pa	0.0023

2.4.3 Lengthwise conductance and its dependence on temperature

Fiber devices behave electrically conductive along the axial direction, and the conductivity decreases as temperature goes up. The conductive polymeric films, CPE, used in fibers offer ~10^7 times greater nominal resistivity at room temperature, and ~20 times

greater TCR, comparing to widely used metal films. To characterize fibers' lengthwise conductive prosperity, we measured the conductivity of CPE films after thermal drawing process and its dependence on temperature.

As-drawn fibers were prepared the same way as we described in 2.3.1. Four 1-mm-wide contact pads were constructed on the CPE films at a 2-mm-spacing to set up four-probe measurements. Two NI MyDAQ were used to record the current and the voltage across the CPE films. A thermal camera (FLIR E60) were located 30 cm above fibers to record the temperature of CPE films. Figure 2.8 presents the relative electrical resistance of CPE films at various temperature. Six runs were carried out over the same fiber segment. Run 1-3 were conducted consecutively within an hour; and run 4-6 were done on the next day. All six runs together fix into an exponential curve:

$$R/R_0 = 0.087 \cdot e^{0.091(T-25)} + 0.91, \qquad (2.5)$$

which suggests excellent repeatability. Here R_0 is the nominal resistance at 25 ^{o}C, measured to be 6.3±0.1 kΩ. Subsequently, the resistivity of CPE films is calculated to be 0.20 Ω·m, with a TCR constant of 0.091 K^{-1}.

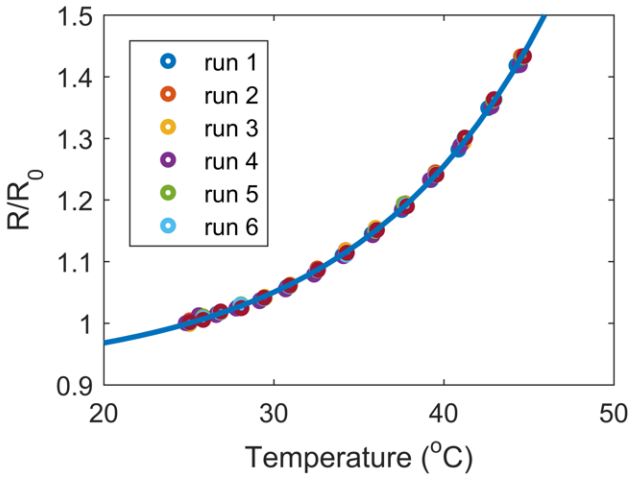

Figure 2.8. Measured (colored dots) and fitted (blue line) relative electrical resistance of CPE films at various temperatures.

2.4.4 Crosswise capacitance and its dependence on water-column-length

Fiber devices have a structure similar to parallel plate capacitors, with either air or water filling the majority room between two plates. When air fills into the fiber channel, the dielectric of fiber capacitor consists of two thin layers of PE and one thick layer of air, resulting in a low capacitance. On the other hand, when filled with water, which usually treated as a conductor, the dielectric of fiber capacitor only consists of two thin layer of PE. Consequently, fiber exhibits a high capacitance. For a fiber segment that is partially filled with water, its capacitance equals the sum of the capacitance of air region (low capacitance per unit length) and the capacitance of water region (high capacitance per unit length). As a result, the overall capacitance of a fiber is dependent on the amount of water inside of its channel, or simply the total length of water column. To characterize fibers' crosswise capacitive properties, we measured the capacitance of fiber devices with various water-column-length inside of the channel.

A 2.5-cm-long fiber segment was prepared the same way as we described in 2.3.2. The top and bottom silver paint were hooked up to a LCR meter (Hioki 3532-50 LCR HiTester). We measured the magnitude of impedance with frequencies swept from 50 Hz to 5 MHz.

As we can see in Figure 2.9, device behaves pure capacitive at low frequency (< 1 MHz). The capacitance increases as water-column-length increases. Insert shows the calculated capacitance as a function of water-column-length. The slope is found to be 23.4 pF/cm, only 3% lower than our estimates from the channel geometry.

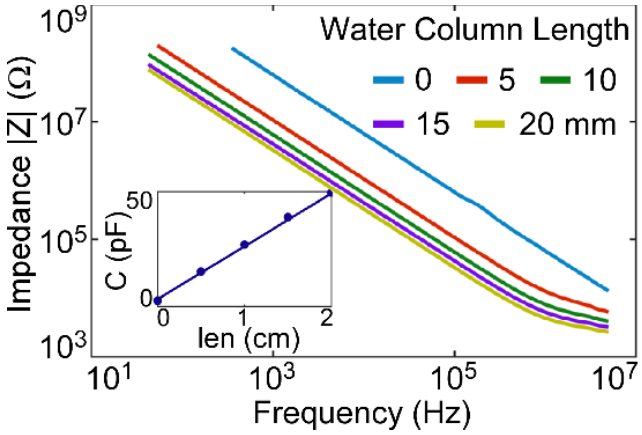

Figure 2.9. Magnitude of impedance of a fiber segment filled with various water-column-length. Inset shows the derived capacitance as a function of water-column-length.

Chapter 3: Fiber Pumps

In this chapter, we investigate fiber pumps integrate-able in microfluidics feedlines, which are enabled by electrowetting-on-dielectric (EWOD) actuation. Fiber pumps offer precise manipulation of liquid flow, with rapid flow response and predictable flow behaviors. We start our discussions with the motivation of in-line flow pumping. Then we introduce how our fiber devices can be used as pumps, and provide a lumped-element circuit model to estimate the maximum available pumping force. At last, we explore the possibility of dual-direction flow control, and demonstrate rapid flow response as well as predictable flow behaviors.

3.1 Motivation of Fiber Pumps

One of the main reason for microfluidics' popularity in life science and chemistry synthesis is its precise control of liquid down to picoliter level. [1] A flow control system is an essential component of any microfluidics system to enable precise manipulation of liquid flow. However, current widely used syringe pumps suffer from periodic pulsations and seconds-to-hours response time, especially at low flow rate and large flow systems. [23], [24] Other off-chip pumps also have their own weaknesses that prevent them from precise controlling liquid movement in microfluidic systems, such as the periodic pulsations of peristaltic pumps or undetermined flow rate in pressure controlled system. As a result, extra on-chip flow control is generally necessary for liquid manipulation down to picoliter level. [25], [26]

In general, on-chip micropumps drive liquid either mechanically or electrically. [27] A mechanical micropump usually consists of a mechanical actuator to convert electric energy to mechanical work; while an electrical pump take advantage of electrical phenomena, such as electrohydrodynamics [28], [29], electrokinetics [30], and

electrowetting [31], [32]. Among various pumping principles, electrowetting-on-dielectric (EWOD) is particularly promising because of its low power consumption, simple structure and easy control. [33], [34] However, regardless of the various pumping mechanisms, on-chip micropumps inevitably increase chip complexity, and hence reduce fabrication yield.

Overall, these substantial drawbacks associated with existing pumps limit their applications in large-scale integration of microfluidics systems, which require many portable pumps without sacrificing chip complexity. Nevertheless, the need for large-scale inter-chip flow actuating makes it important to explore new structures for flow monitoring.

3.2 Mechanisms of EWOD Actuation

3.2.1 Thermodynamic approach

Electrowetting refers to the technique to modify the wetting properties of a surface by applying a potential to it [35]. According to Lippmann-Young Equation, liquid contact angle θ is related to applied potential V by:

$$\cos\theta = \cos\theta_0 + \frac{1}{2\gamma_{LG}} cV^2 \qquad (3.1)$$

where θ_0 is the contact angle at zero potential, γ_{LG} is the interfacial energy between liquid and gas, and c is the capacitance per unit area of the dielectric layer. The equation above is the direct result from general Gibbsian interfacial thermodynamics, and does not require the existence of an insulating layer. If bare electrode is used, c refers to the unit capacitance of the electric double layer that builds up. If EWOD is used, unit capacitance of the insulating layer dominates c.

Thus, the pumping force in EWOD actuation originates from the contact angle difference between two open ends of a flow system. In Figure 3.1, the pulling force F_{pull} arises from surface tension, which equals the surface tension between liquid and gas γ_{LG}

multiplied by the length of contact line P. F_{pull} is same on both ends in Figure 3.1, but point to different directions. Combining those two pulling force, the net pumping force F_{p} becomes:

$$F_p = F_{pull} \cdot \Delta \cos\theta = \frac{1}{2} cPV^2 \tag{3.2}$$

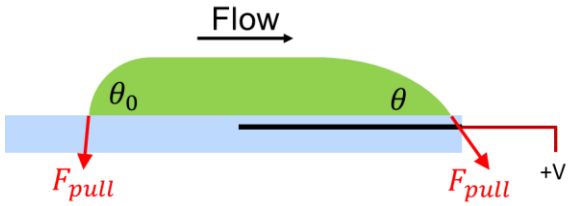

Figure 3.1. Schematics for the mechanism of EWOD actuation.

3.2.2 Electromechanical approach

Previous discussion addresses pumping force from a thermodynamics approach, which can be difficult to find an estimate. Alternatively, we can calculate the available pumping force from an electromechanical approach, where we analogize pumping liquid to inserting a conductor plate into a parallel plate capacitor. As seen in Figure 3.2, the presence of a metal plate triggers a non-uniform electric field distribution, which sequentially causes a non-uniform Maxwell stress tensor around the surface of metal plate (see Figure 3.3).

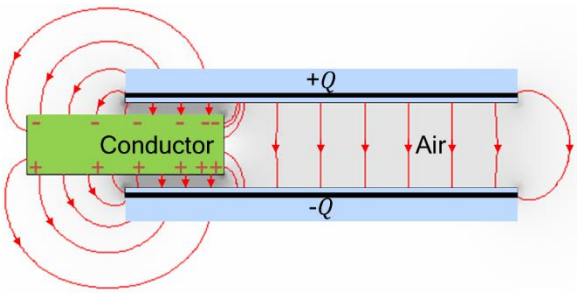

Figure 3.2. Schematics for inserting metal plate into a parallel plate capacitor.

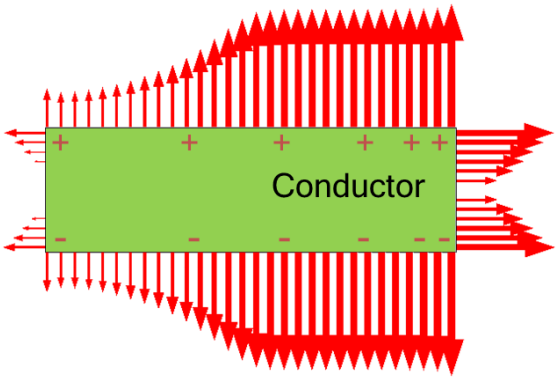

Figure 3.3. Non-uniform distribution of stress tensor around half-inserted metal plate.

Figure 3.3 reveals a horizontally symmetric distribution, as well as a vertically non-symmetric distribution of stress tensor. The net electrostatic force points inward, i.e. an attractive force is applied on the conductor plate to pull it into the capacitor. We can calculate this attractive force by integrating stress tensor over the left and right surface, or simply using virtual work principle. By this method, we consider the virtual work dU that is required to pull the conductor plate into the capacitor by a small distance of dx. dU equals the change of stored electrostatic energy in the capacitor, which is related to the change of capacitance dC by the following equation:

$$\mathrm{d}U = F_p \cdot \mathrm{d}x = \frac{1}{2}V^2 \cdot \mathrm{d}C. \tag{3.3}$$

We rewrite the above equation for an expression of pumping force F_p.

$$F_p = \frac{1}{2}\left(\frac{\mathrm{d}C}{\mathrm{d}x}\right)V^2. \quad (3.4)$$

Note that $\frac{\mathrm{d}C}{\mathrm{d}x}$ represents the change of the capacitance as the conductor plate comes in (or liquid flows in). It matches one of fibers' electrical properties that we characterized in 2.4.4. Thus, the electromechanical approach we discussed here offers an efficient way to estimate pumping force.

The capacitance C in the above equation equals the unit capacitance c multiplied by the area of the capacitor $A = P \cdot x$. Substituting that $C = cPx$, the above equation reduces to results we arrived in 3.2.1. In other words, both equations agree with each other.

Both thermodynamics approach and electromechanical approach reveal that creating a thin and uniform dielectric layer is crucial to EWOD devices. Thus previous research efforts are mainly focused on developing on-chop EWOD pumps, where such dielectric layer can be easily created by spin-coating. [33], [36]

3.3 Available Force of EWOD Actuation

In this section, we follow electromechanical approach to estimate available pumping force, which requires a better understanding of the change of capacitance as liquid flows in. To do so, we conduct a circuit model analysis for fiber electronics.

3.3.1 Circuit model of fiber pumps

The exceptional large aspect ratio makes fiber devices essentially a distributed system. A lumped-element circuit model is usually required to analyze such system. Fortunately, fiber pumps operate mostly under DC voltage and as capacitors, which means almost no current flows through the devices. In this case, a simple cross-sectional analysis can describe the system.

Figure 3.4 shows the cross-sectional circuit model for air and water-filled fiber pumps. Each model consists a few resistors and capacitors that represent different components such as CPE and water. A summary of descriptions and estimated values for those circuit elements is available in Table 3.1.

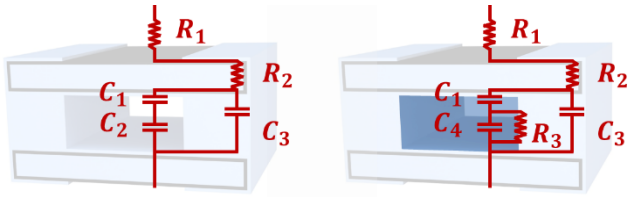

Figure 3.4. Cross-sectional circuit model of air (left panel) and water (right panel) filled fiber pumps.

Table 3.1. Descriptions and estimates for various components in cross-sectional circuit models.

Symbols	**Descriptions**	**Est. Values**
R_1	Contact and lead resistance	0.5 kΩ·cm
R_2	CPE resistance	3 kΩ·cm
R_3	Water resistance	1-10 kΩ·cm
C_1	Dielectric layer capacitance	24 pF/cm
C_2	Air channel capacitance	0.15 pF/cm
C_3	Side wall capacitance	1 pF/cm

By the circuit models in Figure 3.4, we express the overall impedance for air-fill fiber Z_a and water-filled fiber Z_w as:

$$Z_a = R_1 + R_2 + \frac{1}{\omega C_3 + \frac{\omega}{1/C_1 + 1/C_2}}; \tag{3.5}$$

$$Z_w = R_1 + R_2 + \frac{1}{\omega C_3 + \frac{1}{\frac{1}{\omega C_1} + \frac{1}{1/R_3 + \omega C_4}}}. \quad (3.6)$$

To simply the above expressions, we take a review of Table 3.1, and notice that C_1 is much greater than C_2. Z_a can be reduced to:

$$Z_a = R_1 + R_2 + \frac{1}{\omega C_3 + \omega C_2}; \quad (3.7)$$

Furthermore, assuming devices always operate under DC or low frequency ($f \ll 1$ MHz), we have the following two inequalities:

$$\omega R_3 C_4 \leq 0.75f \text{ μsec} \ll 1;$$
$$\frac{C_3}{C_1} + \omega R_3 C_3 \leq 0.042 + 0.06f \text{ μsec} \ll 1.$$

By the two inequalities above, we simplify Z_w to:

$$Z_w = R_1 + R_2 + R_3 + \frac{1}{\omega C_1}; \quad (3.8)$$

Now we can define effective resistance and effective capacitance for both air-filled and water-filled channel as follows:

$$R_a = R_1 + R_2$$
$$C_a = C_2 + C_3$$
$$R_w = R_1 + R_2 + R_3$$
$$C_w = C_1$$

We can then interpret the impedance of air-filled and water-filled channel as a simple RC circuit connected in series.

$$Z_a = R_a + \frac{1}{\omega C_a}; \quad (3.9)$$
$$Z_w = R_w + \frac{1}{\omega C_w}; \quad (3.10)$$

Note that here both Z_a and Z_w are impedance for a segment of unit length. For a segment of arbitrary length *l*, the above expressions need to be divided by *l*. Now consider

a fiber segment that is partially filled with water (length l_a) and partially air (length l_w), the overall impedance Z_t is equivalent to the parallel combination of both sections (see Figure 3.5 for details):

$$\frac{1}{Z_t} = \frac{l_a}{Z_a} + \frac{l_w}{Z_w}. \tag{3.11}$$

Combing the three equations above, we arrive at the final expression for Z_t:

$$Z_t = \frac{1}{\frac{l_a}{R_a + 1/\omega C_a} + \frac{l_w}{R_w + 1/\omega C_w}}. \tag{3.12}$$

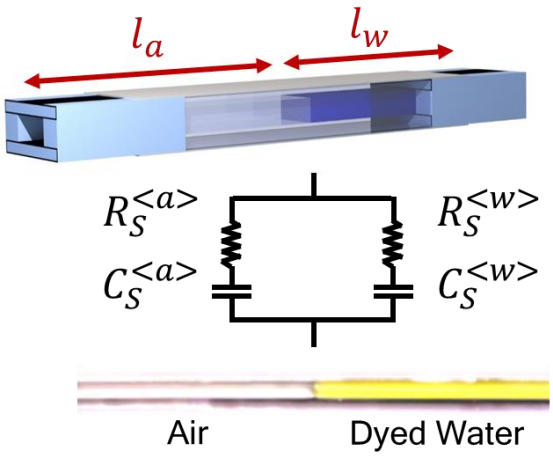

Figure 3.5. (top panel) Schematic of fiber segment 50% filled with water; (middle panel) corresponding simplified circuit model; (bottom panel) a photograph of fiber segment 50% filled with water (yellow, color from Fluorescein Sodium soluble dye)

We revisited the measurement results acquired in 2.4.4, and fitted them using the equation above. Figure 3.6 shows the measured results (left panel) together with fitted results (right panel). Nearly perfect fitting validates our circuit model. Table 3.2 lists all estimates and fitted values for each circuit components. The effective capacitance for both water and air are very close to our estimates from channel geometry. Device behaves

mostly capacitive over the frequency band in our measurements, leading to relatively larger error in the effective resistance values.

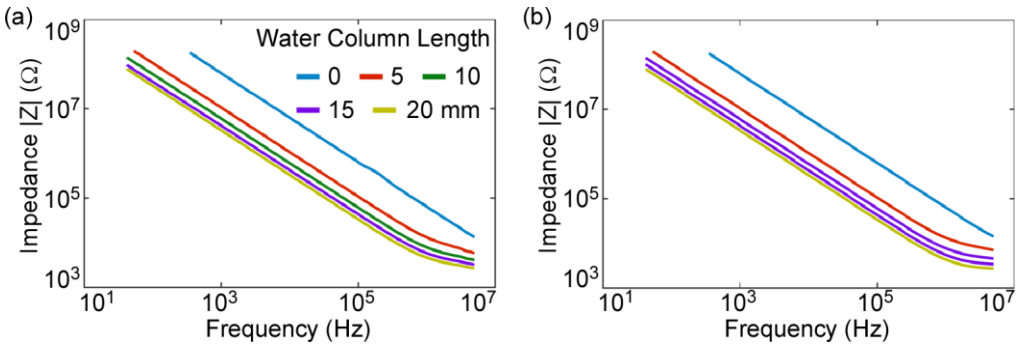

Figure 3.6. (a) Measured and (b) fitted impedance of fiber pumps filled with various amount of water.

Table 3.2. Estimates and fitted values for effective resistance and capacitance.

Symbols	Definitions	Est. Values	Fitted Values
R_a	$R_1 + R_2$	3.5 kΩ·cm	16 kΩ·cm
R_w	$R_1 + R_2 + R_3$	4-15 kΩ·cm	5.3 kΩ·cm
C_a	$C_2 + C_3$	1.15 pF/cm	1.01 pF/cm
C_w	C_1	24 pF/cm	23.4 pF/cm

3.3.2 Estimation of pumping force

In the scope of this thesis, fiber pumps only operate under DC source. As a result, we can ignore the resistance terms in the previous results, and derive out a new, much simplified equation for Z_t.

$$Z_t = \frac{1}{2\pi f(C_a l_a + C_w l_w)}. \tag{3.13}$$

Or,

$$C_t = C_a l_a + C_w l_w. \tag{3.14}$$

Here C_t is the total capacitance since no resistive terms exist anymore. Substituting that water column length $l_w = x$ and total segment length $L = l_a + l_w$, C_t becomes:

$$C_t = C_a L + (C_w - C_a)x. \quad (3.15)$$

Combing the equation above with the result from 3.2.2, we reach a final expression for pumping force:

$$F_p = \frac{1}{2}(C_w - C_a)V^2. \quad (3.16)$$

With the fitting values in Table 3.2, we estimate the pumping force to be:

- 1.12 nN at 1 V;
- 0.112 μN at 10 V;
- 11.2 μN at 100 V;
- 0.101 mN at 300 V;

3.4 Bi-directional Flow Control

3.4.1 Test setup for fiber pumps demonstration

Figure 3.7 presents a schematic view of test setup for fiber pumps demonstration. A 10-cm-long fiber segment was prepared following the same procedure as described in 2.4.4. The top and bottom silver paint were hooked with a high voltage power source (Stanford Research PS350) for a constant voltage supply. The position of liquid/air interface was recorded by a digital camera (Canon T2i) at 2-second intervals. Acquired images were processed in MATLA to extract water column length.

As we can see in Figure 3.7, water reservoir is at a lower level than fiber pumps to establish a backflow when no voltage being supplied. A thin layer of low viscosity silicone oil (Sigma Aldrich) is applied to reduce the evaporation of water and enhance the reversibity of electrowetting. [37]–[39] 300 V voltage supply is powered on and off for three cycles to demonstrate dual-direction flow control covering a length of 20 mm.

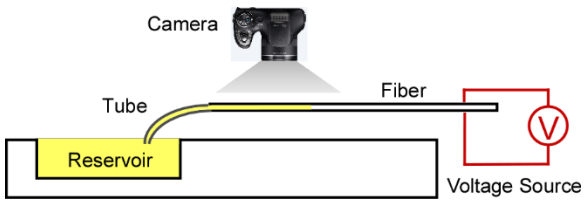

Figure 3.7. Schematic view of test setup for fiber pumps demonstration.

Figure 3.8 shows a few examples of acquired image showing various amount of water (yellow, color from Fluorescein Sodium soluble dye) inside of the channel. We would like to extract the location of water/air interface, which is an edge detection problem in digital image processing.

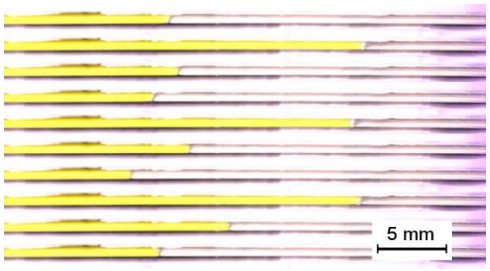

Figure 3.8. Acquired images showing water/liquid interface at various locations.

3.4.2 Image processing in MATLAB

Each of acquired images in Figure 3.8 originally contains 2592x1728 pixels. Each pixel consists of three integers of int8 type, indicating three color-spaces, i.e. red, green and blue (see Figure 3.9a). We first cropped the images to keep only the region with fibers (Figure 3.9b). Among the three color-spaces, we chosen to use blue intensity for image processing, which gives us the largest contrast because the absorption spectrum of soluble dye peaks at 460 nm. Then we converted obtained 2D array of integers to a new array of double type (Figure 3.9c). At the end, we calculated the weighting average along the

vertical direction by applying a Gaussian filter. Thus we arrived at 1D array of doubles, which would be later used for edge detection.

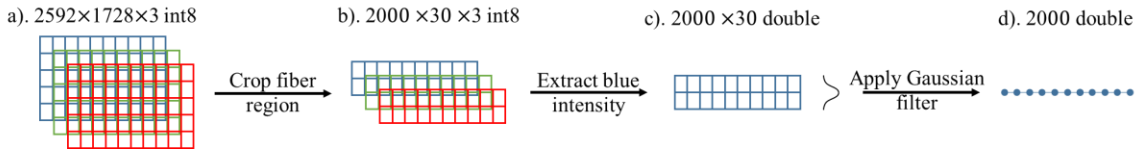

Figure 3.9. Signal conditioning for image processing in MATLAB

Sample code for signal conditioning is listed as follows:

```
% read image file
img_int = imread(filename);
% keep only region with fiber
% keep only blue intensity
img_double = im2double(img_int(Fiber_H0:Fiber_H1,
Fiber_W0:Fiber_W1, 2));
% generate Gaussian filter
filter_gauss = gausswin(1+Fiber_H1-Fiber_H0);
% apply the Gaussian filter
signal = filter_gauss'*img_double;
```

Figure 3.10 shows 500 examples of such 1D signal with liquid/air interface (or edge) aligned to the center. As we can see, air appears at a larger intensity comparing to water, because of the absorption of soluble dye in the water. All acquired curves are extremely noisy mainly due to the variation of illumination. As a result, we could not find a simple threshold of intensity to distinguish air from water. Instead, we applied a difference of box (DoB) filter to reduce the influence of noise.

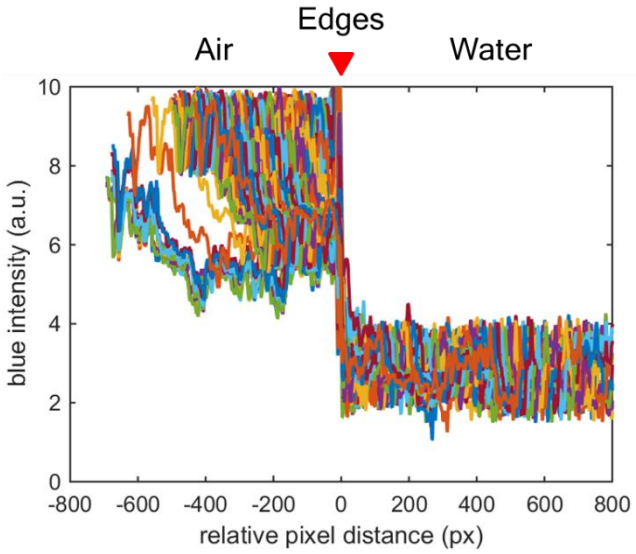

Figure 3.10. Five hundred of examples of 1D array signal with edge aligned to the center.

DoB filter is essentially a first order gradient filter, which converts an edge detection problem into maximum gradient seeking problem. The following equation shows how a DoB filter calculates the output. Basically, the sum of *k* values ahead and behind the current value are calculated independently, and then the difference of those two sums is used as the output.

$$\mathrm{DOB}^{<2k+1>}(i,x) = \sum_{m=i-k}^{i-1} x(m) - \sum_{m=i+1}^{i+k} x(m)\,. \qquad (3.17)$$

In Figure 3.11, the top panel shows an example of DoB filter for the case of k=3 and i=8. The bottom panel gives the response of such filter to an edge signal, as well as a random noise signal at similar amplitude. As we can see, edge signal results in an output ~6 times greater than the output of random noise. Thus, DoB filter converts an edge to a spike at the output, and reduces the influences of random noise.

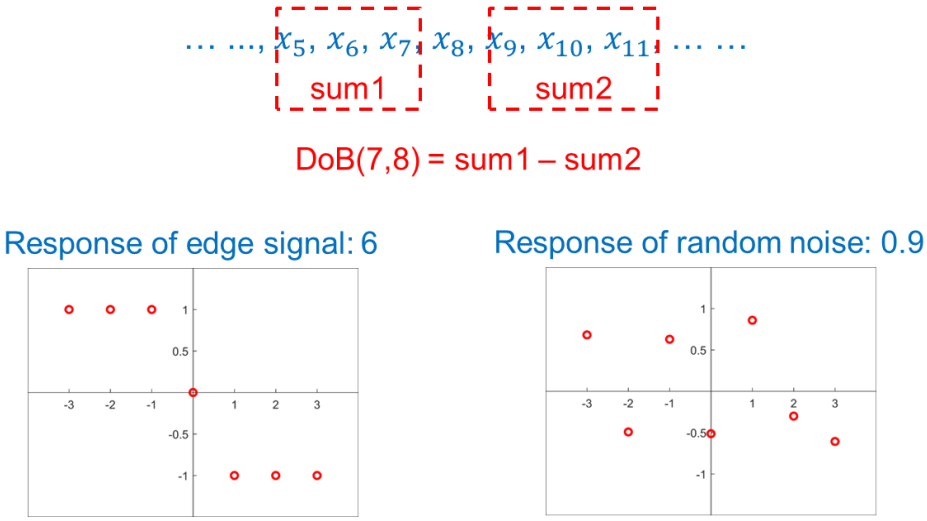

Figure 3.11. (top panel) An example of DoB filter for the case of k=3 and i=8; (bottom left panel) response of such DoB filter to an edge; (bottom right panel) response of such DoB filter to random noise.

DoB filter allows to detect an edge in input signal by searching for the maximum points in output signal. However, it is also sensitive to noise in specific frequency range, especially around frequency of 1/(2k+1). Figure 3.12 shows the frequency response, i.e. the filter output to sine-waves at various frequencies, of a DoB filter with a window size of 7 pixels. The filter output is as strong as 5 times of the strength of input signal at a frequency around 1/7 pixel^{-1}. Fortunately, our edge signal of interest does not fall into this range. Therefore, we can apply a band-stop filter to suppress the output around frequency of 1/(2k+1).

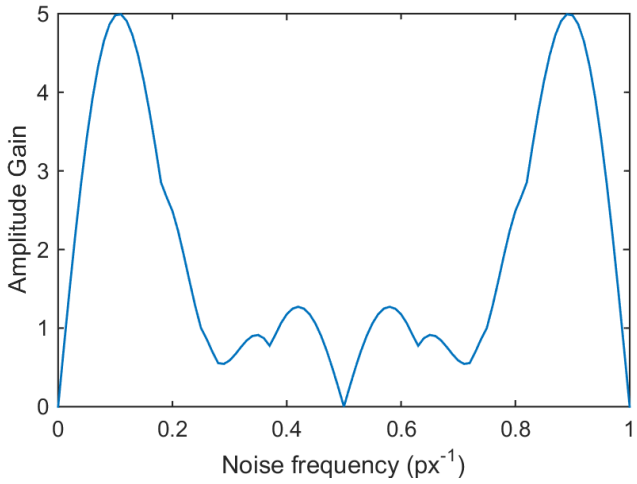

Figure 3.12. Frequency response of a DoB filter with a window size of 7 pixels.

To eliminate the influences from noise, we designed a band-stop FIR filter with a stop band from 0.02 to 0.21 pixel^{-1} (Figure 3.13 left panel). The signal before and after filtered is presented in the right panel in Figure 3.13. Obviously, less noise presents in the filtered signal, while the edge still maintains sharp.

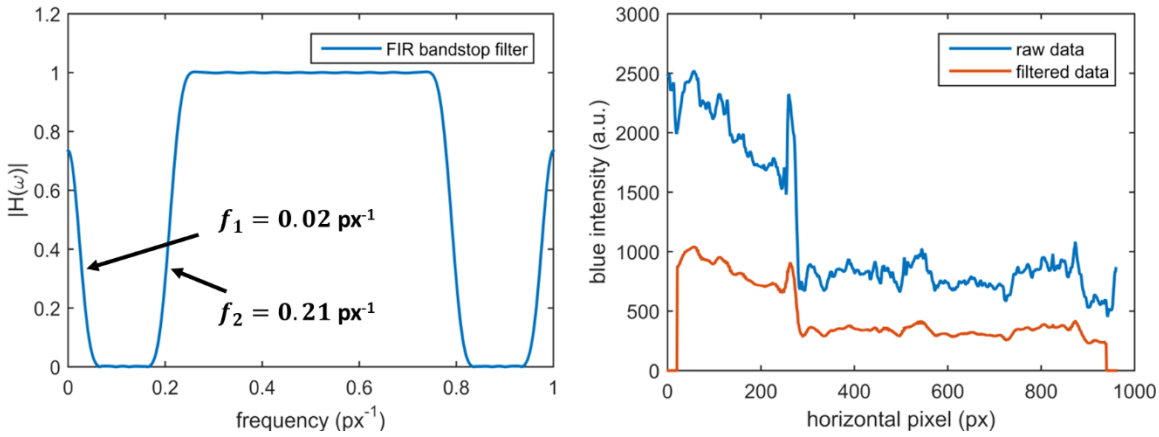

Figure 3.13. Designed band-stop FIR filter (left panel) and signal before and after filtered (right panel).

Sample code for applying DoB and FIR filter is listed as follows:

```
% create DoB filter
filter_DoB = [1,1,1,0,-1,-1,-1];
% create FIR filter
filter_FIR = fir_generate(0.02, 0.21);
% apply both filters
signal = conv2(signal, conv(filter_DoB,
filter_FIR));
```

Figure 3.14 shows the noise floor created by 500 signals before (left panel) and after (right panel) applying band-stop FIR filter. We observed a ~5 dB drop on noise floor after filtered, which significantly reduces the frequency of false detection from once per 50 images to once per 1000 images.

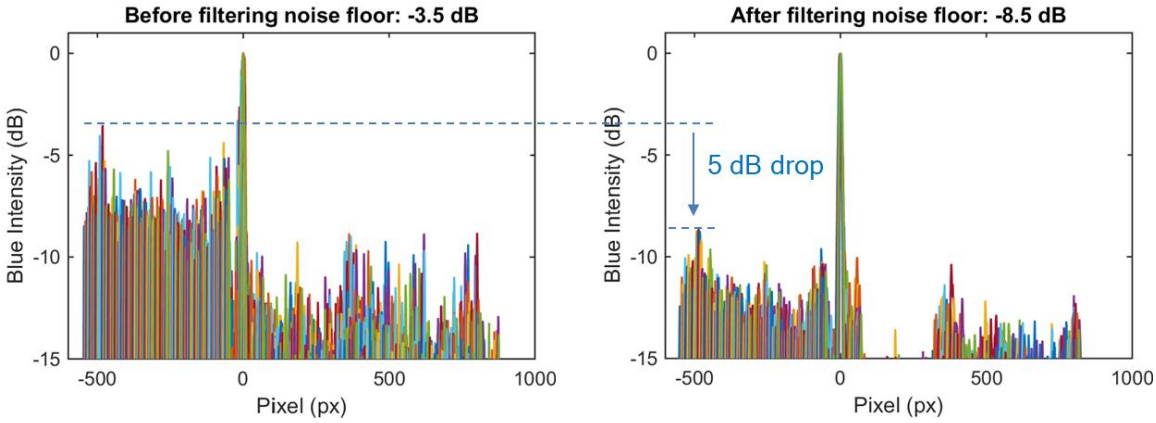

Figure 3.14. Nosie floor before (left panel) and after (right panel) applying band-stop FIR filter.

Overall, we developed an image processing algorithm to detect the interface between air and water. The algorithm mainly consists of three steps: signal pre-conditioning, FIR filtering, and DoB filtering. For N images of w by h pixels, the computational complexity is estimated to be $100 \cdot Nwh$. For a typical pumping test of 20k images, false detection occurs to less than 10 images.

3.4.3 Demonstration of bi-directional flow control

With the image processing algorithm discussed earlier, we extracted the position of air/liquid interface in each image and plotted it against time in Figure 3.15. 300 V voltage supply was powered on and off for three cycles to demonstrate bi-directional flow control over 20-mm-long region. Green regions in lower panel highlight the status of power on, where active pumping is ongoing with a max velocity of 0.4 mm/s. White regions indicate the status when power is off, and fiber pumping is passively withdrawing liquid back to the reservoir. Red circles mark the instances of which the time-lapse images were captured, demonstrating a good match between the interface extracted by eyeballing and by image processing algorithms.

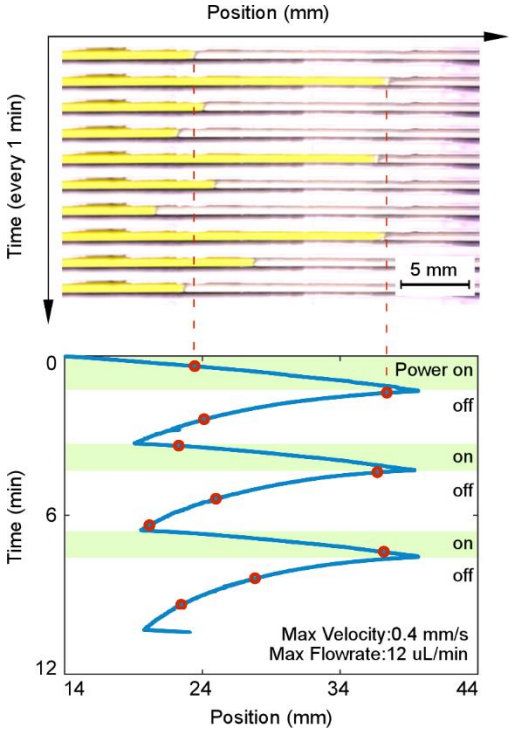

Figure 3.15. Time-lapse photographs of fiber pumping at 1-minute interval (upper panel) and extracted position of air/liquid interface at 2-second interval (lower panel).

We zoomed in the green regions in Figure 3.15, and replotted it in Figure 3.16 right panel. By contrast, the same plot for syringe is also shown in Figure 3.16 left panel. As we can see, the initialization time for commonly used syringe pump is measured to be near 20 seconds. However, it only takes fiber pumps sub-100-millisecond to initialize and finalize, thanks to its large ratio of working volume/device volume and its motorless structure.

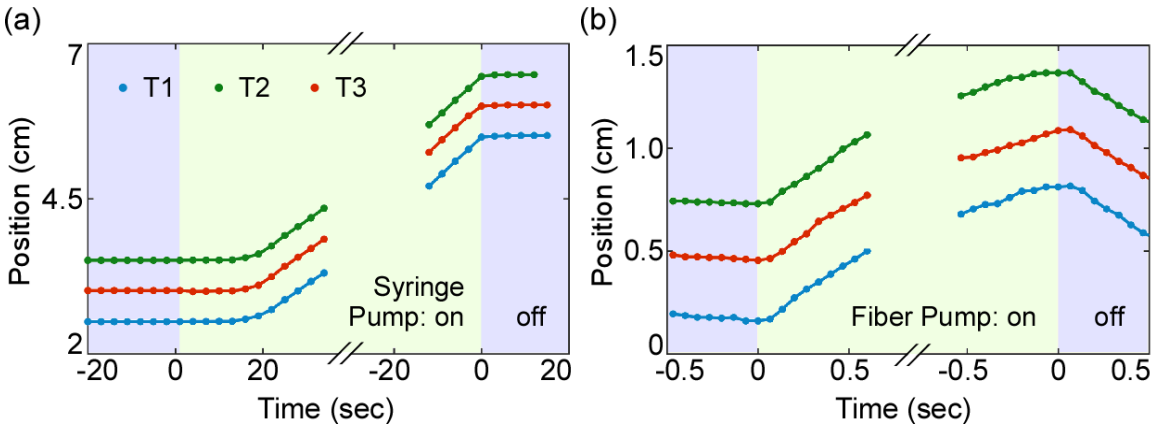

Figure 3.16. Initialization and finalization sections of (a) a syringe pump and (b) a fiber pump.

3.5 Predictable Flow Behaviors

3.5.1 Flow dynamics model for liquid pumping

Fiber pumps are in essence pressure pumps, and follow Hagen-Poiseuille equation. [40] Volumetric pumping rate Q is proportional to pressure difference ΔP at two ends:

$$Q = \frac{\Delta P}{R} = \frac{F}{R \cdot A}, \tag{3.18}$$

where R is the flow resistance of fluidic channel, dominated by the connecting tube (1-cm-long, 0.25-mm-ID) between fiber and reservoir. Pumping rate Q is proportional to flow velocity dx/dt, where x is water-column-length. The pressure difference ΔP consists of three major components: hydrostatic pressure from the height difference between fibers'

entrance and liquid reservoir ($\rho g \Delta h$); non-horizontal fiber orientation ($\rho g x \cdot \sin\alpha$); and the difference of contact angle ($PA \cdot \gamma_{LG} \cdot \Delta\cos\theta$). As a whole, ΔP can be expressed as P_0 - LP_1, where P_0 accounts for the first and the third term, whereas LP_1 represents the second term. Typically, hydrodynamic resistance R increases with longer water column. However, in our system, R is dominated by the connecting tube between fiber and reservoir, and hence remain constant R_0. Overall, the equation above becomes:

$$A \cdot \frac{\mathrm{d}L}{\mathrm{d}t} = \frac{P_0 - LP_1}{R_0},$$
$$\frac{\mathrm{d}L}{P_0 - LP_1} = \frac{\mathrm{d}t}{R_0 \cdot Area}. \tag{3.19}$$

Integrating both sides of the equation above, we arrive at the governing equation for liquid pumping:

$$t - t_0 = \left(-\frac{R_0 A}{P_1}\right) \ln(P_0 - LP_1). \tag{3.20}$$

Note that even for the same fiber pump, we might observe different liquid driving curves due to slight changes on test setup. For example, a change of fiber orientation from 0 to 1 degree upwards would cause an increase of P_1 from 0 to 1.7 Pa/cm. Figure 3.17 illustrates several liquid pumping curves with different parameters. As we can see, only 10% change on any of three parameters can significantly shift the liquid driving curves. And those changes will further pass down to change the shape of operation region, as we will discuss in next section.

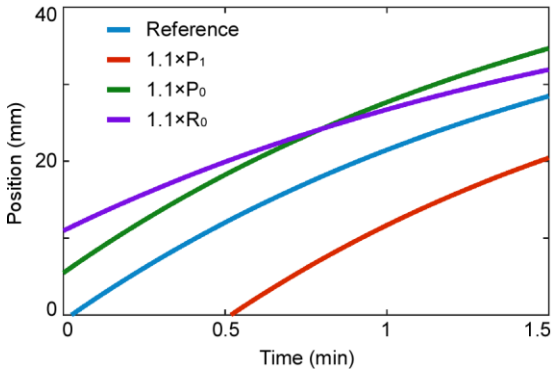

Figure 3.17. Liquid pumping curves with different parameters.

3.5.2 Discussions on liquid pumping curves at 300 V

The three liquid pumping curves at 300 V (see Figure 3.15) agree with the flow dynamics model we discussed in 3.5.1. Figure 3.18 shows the near-perfect match between measured and fitted liquid pumping curves:

$$t - t_0 = -1.66 \times \ln(30.89 - 0.41 \times L)\,. \qquad (3.21)$$

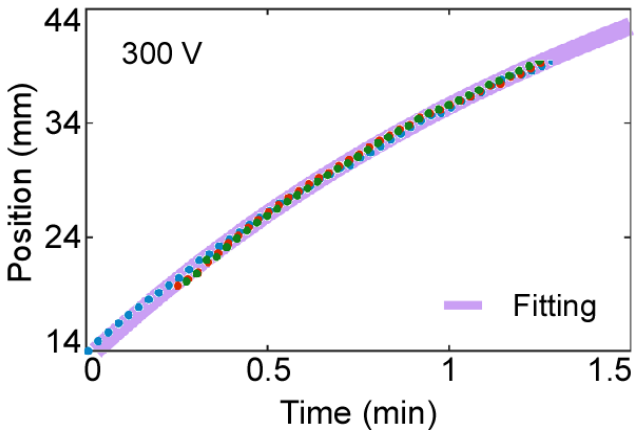

Figure 3.18. Measured (dots) and fitted (line) liquid pumping curves using derived flow dynamics model.

Comparing the formula above with the flow dynamics model we discussed in 3.5.1, fiber pumps offers a pumping pressure of at least 30.89 Pa at 300 V, without considering

withdrawing pressure at 0 V. As liquid pumps into fiber, there is a constant pressure loss of 0.41 Pa/mm, corresponding to a 2.4° upward orientation of fiber. To eliminate the withdrawing pressure from pumping pressure, we need to conduct multiple liquid pumping tests at various voltage.

3.5.3 Discussions on liquid pumping curves at various voltages

To eliminate the withdrawing pressure from pumping pressure, we measured liquid pumping curves at various voltage. As we can see in Figure 3.19, pumping velocities inevitably increases as applied voltage increases, until reaches saturation after 300 V. All liquid driving curves are fitted using the flow dynamics model we discussed in 3.5.1 with only P_0 values different. The fitted curves all follow the equation below:

$$t - t_0 = -12.5 \times \ln(P_V - 0.093 \times L)\,. \tag{3.22}$$

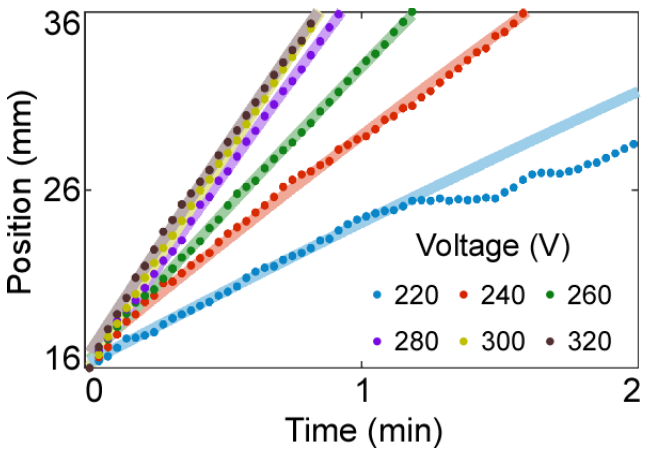

Figure 3.19. Measured (dots) and corresponding fitted (lines) liquid pumping curves at different voltage

Here P_v indicates the available pumping pressure when no liquid has filled in the pump, which follows a quadratic dependence to pumping voltage. By taking the derivative of the equation above with respect to time *t*, initial pumping velocities at 0 mm v_0 can be

derived as $P_V/(12.5 \times 0.093)$. As we mentioned before, P_V consists of hydrostatic pressure from height difference, as well as contact angle difference (electrowetting). The first term is a constant, whereas the second term follows a quadratic dependence to voltage (see 3.2.2 for details). As a results, we can express the initial velocity v_0 as a function of voltage:

$$v_0 = 0.86P_{\Delta h} + \frac{0.43}{A}\left(\frac{\mathrm{d}C}{\mathrm{d}x}\right)V^2, \tag{3.23}$$

where $P_{\Delta h}$ is hydrostatic pressure from height difference between fiber pump and reservoir, and *A* is channel area.

Figure 3.20 shows the measured initial velocities v_0 as a function of voltage square V^2. At low voltage less than 280 V, the linear relation between velocity and voltage^2 is clearly seen, which validate the equation above. As voltage goes up, velocity reaches saturation around 300 V. Overall measured velocity-voltage^2 curve in Figure 3.20 follows the same trend as well-studied contact angle saturation curves [41], [42], indicating the close connection between liquid pumping and meniscus shape.

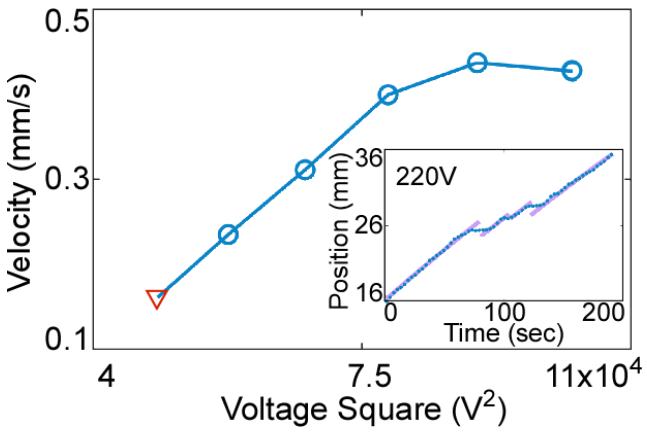

Figure 3.20. Initial pumping velocities at 0 mm as a function of voltage square. Red triangle symbol indicates unsteady pumping, as detailed in the inset figure.

Extrapolating the linear trend between 220 V and 280 V to intercept x-axis, the minimum driving voltage is obtained as 180 V. Thus we calculated the backflow pressure at 0 V ($P_{\Delta h}$) to be -14 Pa, which is equivalent to a height difference of 1.43 mm between fiber and water reservoir. For practice, a minimum driving voltage of 220 V is required to ensure a steady flow due to contact angle hysteresis [43], [44] and contact line pining [45] (Figure 3.20 inset).

3.5.4 Operation regimes of fiber pumps

The flow dynamics model we discussed in 3.5.1 has predicted that fiber pumps can only pump liquid to a certain distance L_{max}, when fiber pumps have an upward orientation (P_1>0). Beyond L_{max}, backflow pressure overwhelms pumping pressure. Other than the applied voltage, the value of L_{max} is also related to test setup, and can be calculated easily after we obtain liquid driving curves. For example, L_{max} equals 75.3 mm for the case discussed in 3.5.2.

The existence of L_{max}, together with saturation voltage and minimum driving voltage, define the operation regimes of fiber pumps. Figure 3.21 presents an illustration of operation regimes using results from 3.5.3. There are four regions in total in this diagram: saturation region, sub-threshold region, pumping region and backflow region. Liquid cannot be precisely controlled in sub-threshold region (below 220 V) or saturation region (above 300 V). At a pumping voltage of 220 V, we can precisely manipulate liquid flow between 0 and 12 cm. A higher pumping voltage allows us to have control over a wider range until the saturation is reached at 300 V. Overall, the minimum driving voltage of 220 V is still high for a lot of biomedical applications. To further explore the possibility of low-voltage pumping, we can use low-flow-resistance connecting tubes, as well as hydrophobic dielectric spacer to replace silicone oil.

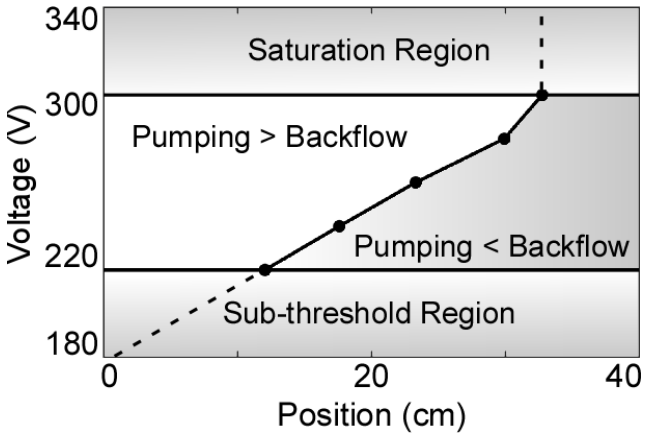

Figure 3.21. Operation regimes of fiber pumps.

To summarize this chapter, we have reported integrated fiber pumps for precise flow control in microfluidics applications, with sub-100-ms flow response and predictable flow behaviors. Bi-directional flow control was demonstrated with the maximum charging, discharging flow rate of 12 uL/min (or 0.4 uL/min) and pumping pressure of 45 Pa. Adjustable pumping velocities between 0.16 to 0.44 uL/min were also observed by controlling the potential from 220 to 300 V. Comparing to syringe pumps, our fiber pumps exhibit less than one hundredth of response time, and much more reliable flow behaviors without oscillations. This new form pumps open up many new opportunities for multi-target optic/chemical analysis and large-scale microfluidics integration.

Chapter 4: Fiber Flow Sensors

In this chapter[3], we investigate fiber flow sensors that overcome the fundamental trade-off between sensitivity, pressure drop, measurement range, and temperature rise. Significant performance improvement over conventional MEMs sensors are achieved with the use of multi-segment structures and novel thermistor materials, both made available by multimaterial fiber process. We develop a first-order 1D heat transfer model to resolve the temperature response of hot films adjacent to ultra-long fiber fluidics channel. The improved sensitivity as well as extended measurement range, as predicted by the 1D analytic model, are also corroborated by numerical simulations and experiments.

4.1 Motivation of Fiber Pumps

Thermal flow sensors have been widely used for precision flow monitoring in microfluidic systems, [46], [47] such as systems with flow cytometry and viscometry. [47], [48] They operate by deriving flow rates from the local temperature distribution of a streaming fluid near a heater (i.e. hot wire or hot film sensors). With no parts in fluid channel interfering liquid flow, their simple structures are readily integrated in MEMs devices and give rise to their popularity. Comparing to various other mechanisms of flow sensing, thermal flow sensing excels in sensitivity and power consumption, characteristics especially important in microfluidics applications. [47], [49] However, their relatively simple structures also impose a fundamental limit on measurement range, typically around two decades. [50], [51] What's worse, their high sensitivity (e.g. 1 mV/(μL·min^{-1})) relies on the use of small fluidic channels (typically less than 100 μm in size), which inevitably leads to large pressure drop (e.g. 500 Pa/mm at 100 μL·min^{-1}). [22], [51], [52] Such large

[3] Part of the content of this chapter has previously been published in *Chen, Boxue, Corey Kwok, Thien-An Ngoc Nguyen, and Zheng Wang. "Integrated Fiber Flow Sensors for Microfluidic Interconnects." Advanced Materials Technologies 3.11 (2018): 1800175.*[15] Co-authors have participated extensively in experiment methods, and have contributed in reviewing the final manuscript.

pressure drop makes it challenging to monitor the multidecade flow range (e.g. 1-1000 $\mu L \cdot min^{-1}$ [53]–[55]) in fluidic interconnects between microfluidics chips.

The inherent trade-off among measurement range, pressure drop, and sensitivity directly results from the thermodynamics of flow sensors. High flow sensitivity requires establishing a thermal boundary layer in fluids of a comparable size to the dimensions of the heater. [56] Given that the thickness of thermal boundary layer is proportional to the channel size and inverse to the square root of volumetric flow rate, small channels sizes of tens of micrometer are required for high sensitivity at small volumetric flow rates [56], [57]. Since pressure drop is inversely proportional to the fourth power of the hydrodynamic diameter of the channel [21], such small channels cause pressure drop as large as few Pascal per microliter per minute [22]. With the thickness of thermal boundary layer inverse to the square root of volumetric flow rate, the fixed sizes and locations of the heaters further limit the measurement range to around two decades. [47], [50], [51]

Overall, such substantial trade-off associated with existing thermal flow sensors makes them challenging to be used for flow monitoring at microfluidic interconnect, and limits the scale and sophistication of large-scale microfluidics systems. [46] It is thus important to explore new thermal flow sensor structures and materials that simultaneously offer minimum pressure drop and extended measurement range, without sacrificing sensitivity.

4.2 Mechanisms of Thermal Flow Sensors

4.2.1 Thermal flow sensors and their typical response

Thermal flow sensors operate by adding localized heat to a streaming fluid, and measure the resulting temperature distribution around the heater (see Figure 4.1). Typical thermal flow sensors fall into three categories: anemometers where a single element is used

as both the heater and the sensor; calorimetric flow sensors where two sensors are placed downstream and upstream the heater; and time-of-flight sensors where one heater is used to add a heat pulse and at least one downstream sensor is used to measure the time between heat pulse generation and detection. In this section, we mainly focus on the first two categories since time-of-flight utilize a very different measurement strategy.

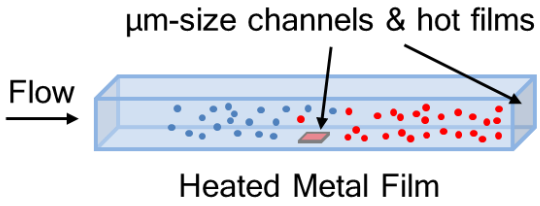

Figure 4.1. Schematics for the mechanism of thermal flow sensors.

The response of thermal flow sensors is closely tied up with the evolution of boundary layer, which refers to a region with a large gradient in velocity (hydrodynamic boundary layer) or temperature field (thermal boundary layer). The main difference between anemometers and calorimetric flow sensors is the ratio of hydrodynamic boundary layer thickness to the streamwise extension of the sensor. For anemometers, this ratio is much less than 1 ($\delta \ll 1$), whereas for calorimetric flow sensors it is much greater than 1. As a result, anemometers response linearly to the square root of flow velocity, while calorimetric sensors response linearly to flow velocity.

Figure 4.2 shows typical responses of an anemometer and a calorimetric flow sensor. As we can see, anemometers response towards a lower voltage as velocity goes up, and get saturated around 10 m/s. The temperature response of anemometers can be derived from total injected heat Q and total heat dissipation rate of $\alpha+\beta\sqrt{U}$, where α denotes conductive heat dissipation rate and $\beta\sqrt{U}$ refers to convective heat dissipation rate:

$$T - T_0 = \frac{Q}{\alpha + \beta\sqrt{U}}. \tag{4.1}$$

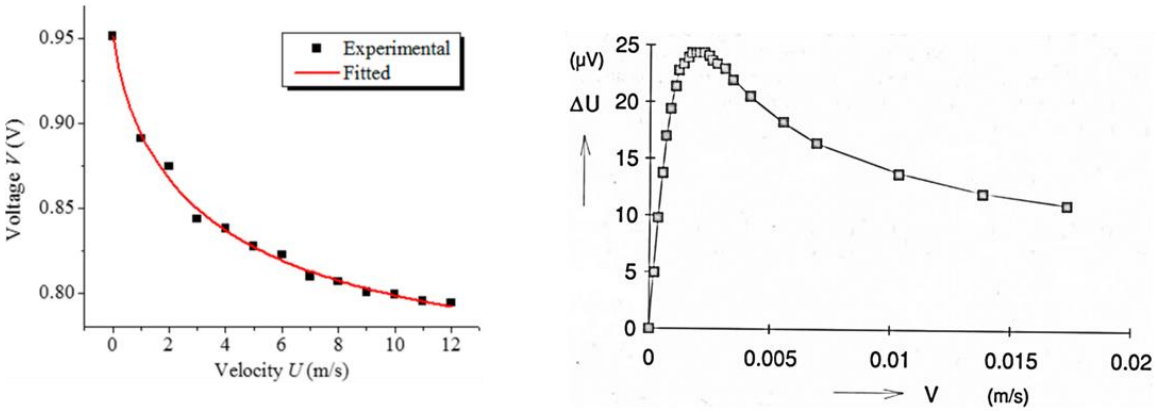

Figure 4.2. Typical responses of two thermal flow sensors: (left panel) anemometers; (right panel) calorimetric flow sensors.

Calorimetric flow sensors, however, mostly operate at much lower velocities. Its response splits into two regions: a linear response region, and a decline region. The response curve peaks when thermal boundary layer thickness equals the streamwise extension of the sensor, which can found by [56]:

$$Q_{max} = A \cdot \frac{2D_T}{l}. \tag{4.2}$$

Typically, people only use the linear response region for device operation, which ends when the thermal boundary is comparable to the streamwise extension of the sensor.

4.2.2 Inherent trade-off among sensitivity, pressure drop and measurement range

Ideal thermal flow sensors exhibit large sensitivity, wide measurement range and low pressure drop simultaneously, which is extremely challenging due to the inherent trader-off among those parameters. Specially, this trade-off consists of two arguments: firstly existing thermal flow sensors rely on small channels to achieve high sensitivity, which evidently causes large pressure drop; secondly the temperature rise of thermal flow

sensors, which approximately equals the product of sensitivity and measurement range, is usually limited. In this section, we will address both arguments in more details.

The sensitivity of existing thermal flow sensors typically are directly related to flow velocity *U*. Thus when considering the sensitivity for volumetric flow rate Q (Q=AU), small channels help to achiever larger sensitivity (S=$\Delta T/(A\Delta U)$). Taking an anemometer for example, we express its sensitivity based on its response curve given earlier:

$$S = \frac{\Delta T}{A\Delta U} = \frac{\alpha\beta\Delta T}{2\left(\alpha + \beta\sqrt{U}\right)^2\sqrt{U}}. \tag{4.3}$$

Its sensitivity peaks at zero flow rate. Take the limit of the equation above as U approaches to zero, we arrive at the maximum sensitivity for anemometer:

$$S_{max} = \frac{1}{A^{0.5}} \cdot \frac{\beta\Delta T}{2\alpha\sqrt{Q}}. \tag{4.4}$$

The results shows that the sensitivity of anemometer is inverse to the square root of channel area. Similarly, for a calorimetric sensor, the sensitivity equals the ratio of temperature rise ΔT to the range of linear region Q_{max}:

$$S = \frac{\Delta T}{Q_{max}} = \frac{1}{A} \cdot \frac{l\Delta T}{2D_T}. \tag{4.5}$$

Basically, the sensitivity of either anemometers or calorimetric sensors increases as we shrink the channel size. However, shrinking channel size is highly unfavorable when it comes to pressure drop. For laminar flow, the pressure drop is inverse to the square of channel area:

$$\Delta P = \frac{1}{A^2} \cdot 8\pi\mu LQ, \tag{4.6}$$

where μ is fluid dynamic viscosity and *L* is channel length. For typical micro-size channels of 100-μm-ID and 1-cm-length, MEMs sensors brings an extra pressure drop as high as 6000 Pa at 100 μL/min. Such large pressure drop absolutely limits the number of flow monitoring units that can be cascaded in large-scale microfluidics systems.

Other than high pressure drop, high sensitive flow sensors are also limited in their dynamic range. For anemometers, their sensitivity decreases very fast as moving into high flow velocities. Table 4.1 lists the average sensitivity of anemometer for various response regions, as predicted by its response curve. As we see from the table, the sensitivity drops to only one sixteenth as flow rate moves to next decade, and continues to drop to less than one hundredth as flow rate moves from $0\sim1$ to $9\sim49$.

Table 4.1. Average sensitivity of anemometers in various response regions.

Response Range (unit: ΔT)	Flowrate Range (unit: $\boldsymbol{A}\cdot(\boldsymbol{\alpha}/\boldsymbol{\beta})^{\boldsymbol{2}}$)	Avg. Sensitivity (unit: $\boldsymbol{\beta^2\Delta T/(\alpha^2 A)}$)
0.5~1	0~1	1/2
0.25~0.5	1~9	1/32
0.125~0.25	9~49	1/320

Calorimetric sensors also suffers the limitation of measurement range. In general, they operate at much lower flow rate comparing to anemometers. Their measurement range is limited by the width of linear region, as shown in Figure 4.2, which ends at the point where thermal boundary layer spreads to the end of the streamwise extension of sensors.

Overall, both forms of thermal sensors are subject to the trade-off among sensitivity, pressure drop and measurement range. In later sections of this chapter, we employ unconventional thermistor materials CPE to break the trade-off between sensitivity and pressure drop. Then we construct a novel multi-segment structure to decouple the trade-off between sensitivity and measurement range.

4.3 Benefits of New Thermistor Material: CPE

To decouple the trade-off between sensitivity and pressure drop, we need to consider other methods to boost sensitivity without shrinking channel sizes. The sensitivity (S=$\Delta V/\Delta Q$) of thermal flow sensors breaks into two components, a device related factor

($\Delta T/\Delta Q$) and a material related factor ($\Delta V/\Delta T$). Previous research efforts have been mostly focused on the optimization of first factor, where numerous device geometries and operation regimes have been proposed. Without change device geometries, Bársony et. al. reported using greater temperature rise (100~500 ^{o}C) to increase the sensitivity of thermal flow sensors. [58] This method, although very effective, is extremely unfriendly to many biomedical applications, which only tolerate limited temperature rise of less than 40 K [59]. Instead, we decide to take a different approach, the first time implementation of conductive polymeric films CPE in thermal flow sensors to boost $\Delta V/\Delta T$. The resistivity of thermistor materials is often described by temperature coefficient of resistance α (TCR), which denotes the relative change of resistance $\mathrm{d}R/R$ with a given change of temperature $\mathrm{d}T$. Thus, under constant current mode, we rewrite the sensitivity as:

$$S = \frac{\Delta V}{\Delta T} \cdot \frac{\Delta T}{\Delta Q} = \alpha I R_0 \cdot \frac{\Delta T}{\Delta Q}. \tag{4.7}$$

The equation above reveals that sensitivity is proportional to TCR value, as well as nominal resistance. Thus, a new thermistor material with much greater TCR value and nominal resistance could significantly improve the sensitivity without sacrificing channel dimensions.

CPE films conduct electrons through two mechanisms: physical contact (low electrical resistance) of carbon black particles (CBs) and tunneling (high resistance) between two close but separated CBs (see Figure 4.3 left panel for details). [20] Consequently, thermal expansion significantly influence its conductivity by changing the average between CBs. As we have measured in 2.4.3, CPE provides a nominal sheet resistance of 6.3 kΩ/□, ~10 million times greater than that of metals (e.g. gold) [47], as well as a TCR constant of 0.091 K^{-1}, ~20 times greater than that of metals. The right panel in Figure 4.3 shows how the relative resistivity of CPE rockets up while metal films only

change a little. By the equation given above, CPE could offer 200 million greater sensitivity than metal films in MEMs sensors with the same geometry, although MEMs sensors usually use thinner films and smaller channels.

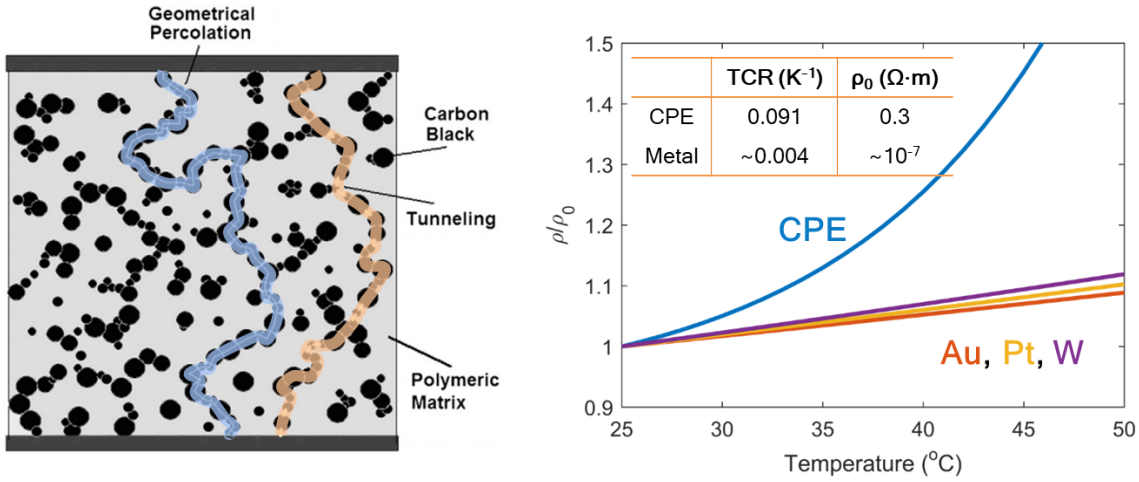

Figure 4.3. (left panel) Two conductivity mechanisms of CPE: physical contact (blue path) and tunneling (orange path); (right panel) relative change of resistivity as respect to temperature change for CPE and several metal films.

4.4 Demonstration of Flow Monitoring

4.4.1 Test setup for fiber flow sensors demonstration

Figure 4.4 presents a schematic view of test setup for fiber flow sensors demonstration. We prepared a 5-cm-long fiber flow sensors from as-drawn fibers by following the procedures as described in 2.4.3. Two surface contacts were constructed that bracket a 2-mm-long sensing area. The fiber segment was suspended in air to emulate the typical thermal environment of microfluidic feed lines. Steady-state flow rates from 5 to 1000 μL/min was established with a syringe pump (Kent Scientific GenieTouch). The fiber sensor was driven in constant-DC-current mode from a power supply (LKB Bromma 2197) through the metal wires near the opposite ends of the sensing area. Voltage response of

fiber sensors were recorded using a NI MyDAQ (195509F-01L), and temperature responses were measured by a thermal camera (FLIR E60) located 30 cm above the sensor. Sampling rate for temperature and voltage recording are 30 Hz and 1 Hz, respectively. The entire test setup was sealed in a 50x60x70 cm plastic enclosure to minimize the temperature fluctuation from air currents. Figure 4.4

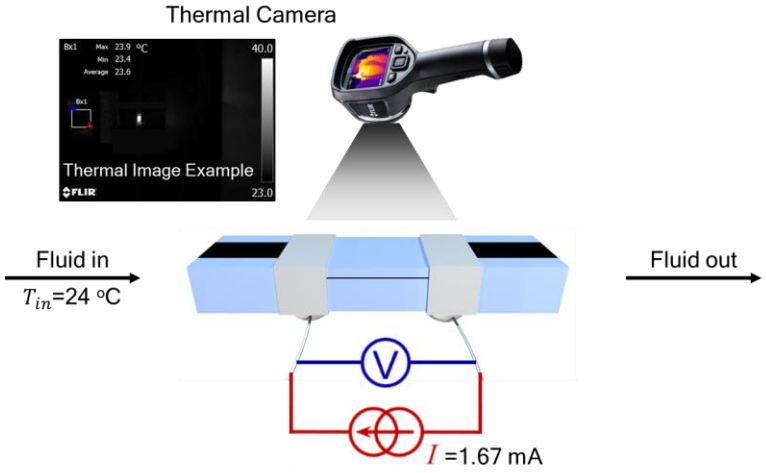

Figure 4.4. Schematic view of test setup for fiber flow sensors demonstration

4.4.2 Measurement uncertainty

The uncertainty of flow rate is calculated from the RMSE of fitting Q_s/Q_m to be 1, where Q_s is the set value of flow rate on syringe pump and Q_m is the measured value of flow rate calculated from the oscillation frequency of pump motor, which translates into the measurable oscillation of temperature and voltage signal.

Measured temperature and voltage response contains low-frequency oscillation signals, which are eliminated by a high pass filter with a cut-frequency at 35 times the

oscillation frequency of pump motor. Afterwards, the uncertainty of temperature and voltage measurements are determined by 3 times the standard deviation of filtered signals.

4.4.3 Response of fiber flow sensors

Figure 4.5 shows measured temperature and voltage response of fiber flow sensors. With a heating current of 1.67 mA and the temperature for ambient air and incoming liquid both at 24 ^{o}C, fiber flow sensor exhibits a linear dependence on flow rate between 0 and 20 μL/min. Temperature and voltage sensitivity are measured to be -0.47 K/(μL·min^{-1}) and -0.38 V/(μL·min^{-1}), respectively, with the latter being a record for thermal flow sensors to the best of our knowledge. Considering fiber sensors using only 20-degree temperate rise and 9-Pa pressure drop, fiber flow sensors vastly outperform state-of-the-art MEMs flow sensors (see Table 2.1 for details).[22], [58] Beyond 20 μL/min, both temperature and voltage response saturate, which indicates a limited measurement range yet to be extended. To better understand such saturation and extend the measurement range of fiber flow sensors, we developed a first-order heat transfer model to describe the temperature response of fiber flow sensors.

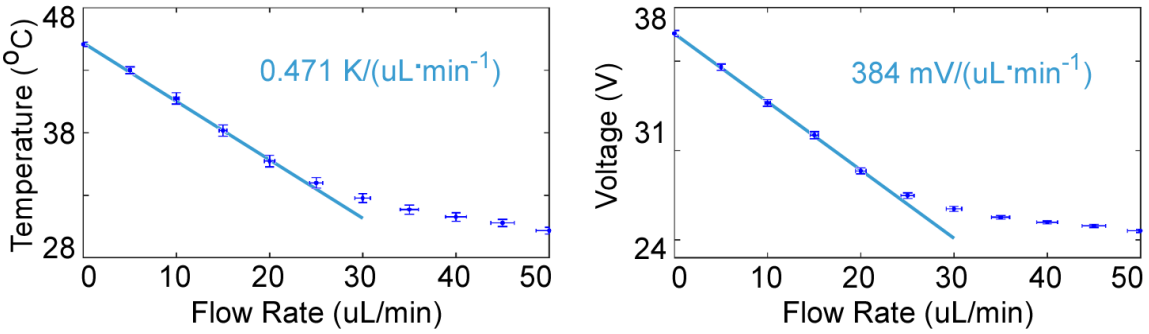

Figure 4.5. Temperature (left panel) and voltage (right panel) responses of fiber flow sensors.

4.5 First-order Temperature Response Theory

4.5.1 Temperature response of a single-segment sensor

Fiber flow sensors operate in constant-current mode. At equilibrium, heat generation rate equals heat dissipation rate. For a given current I, CPE film produces a temperature-dependent Joule heating of $I^2R(T)$, where $R(T)$ is the electrical resistance of CPE at temperature T. The heat dissipation consists of two mechanisms: conductive cooling through fiber cladding into ambient air and the metal wires that interface the fiber sensor to the external circuits, and convective cooling into the streaming liquid inside of the channel. We arrive at a closed-form solution to the temperature response of fiber sensors by making the following simplifications:

1. We linearize the temperature-dependent resistivity near a constant sensor temperature T' (T' will be defined later in Equation S8), from

$$R(T) = R_0 \cdot \left(0.087 \cdot e^{0.091 \cdot (T-25)} + 0.91\right)$$

to

$$R(T) = R(T') + \alpha \cdot R(T') \cdot (T - T')$$

For the test of a single-segment sensor, T' is 45 °C and α is 0.034; whereas for the test of a six-segment sensor, T' is 40 °C and α is 0.025. This simplification introduces an error less than 9% over the entire temperature range (24-45 °C), and less than 3% within the sensitive region (35-45 °C).

2. We approximate the temperature distribution of the liquid, $T_{\text{liquid}}(x)$, along the axial direction of a fiber segment of length l, to be a linear function of x, interpolated from the liquid temperatures at the entrance T_{in} and the exit T_{out}.

$$T_{\text{liquid}}(x) = T_{\text{in}} + (T_{\text{out}} - T_{\text{in}}) \cdot x/l$$

This linear approximation is sufficiently good for sensor segments less than 2 mm long. More accurate results for both shorter and longer segments will discussed later in next chapter.

3. We assume the temperature of CPE hot film within a segment is constant.

Consider a sensor segment with liquid at rest (zero flow rate), Joule heating is dissipated entirely through conductive cooling into the PC cladding (green arrows in Figure 4.6) and the liquid (purple arrow in Figure 4.6). Our one-dimensional theory uses two constants, total heat transfer rate H_0 and heat transfer rate through PC cladding H_1, to describe those two paths of heat dissipation, therefore reducing a 3D problem into 1D problem:

$$H_0 = \int_S h_0 \, \mathrm{d}S = l \int_P h_0 \, \mathrm{d}P$$
$$H_1 = \int_S h_1 \, \mathrm{d}S = l \int_P h_1 \, \mathrm{d}P,$$

where h_0 and h_1 are heat transfer coefficient (W/(m^{2}K)) for H_0 and H_1, respectively. The integration over the perimeter of the hot-film $\int_P h\mathrm{d}P$ is treated as a constant because of the identical cross-sections of fiber sensors, and hence both H_0 and H_1 are proportional to hot-film length *l*. Hot-film temperature reaches its maximum T_0 at zero flow rate,

$$I^2 R(T_0) = H_0(T_0 - T_{RT}), \tag{4.8}$$

allowing H_0 to be determined from measured zero flow temperature T_0, room temperature T_{RT}, and injected current *I*.

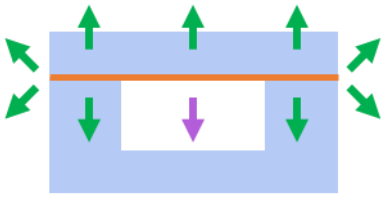

Figure 4.6. Two paths of heat conductive dissipation: through PC cladding (green arrows) and through liquid inside of fluidic channel (purple arrow).

At a non-zero flow rate, flow-rate dependent convective cooling needs to be considered. For a given flow rate Q, film temperature $T_x(Q)$ is determined by solving the equation:

$$I^2R\big(T_x(Q)\big) = H_1 \cdot (T_x(Q) - T_{RT}) + \frac{Nu}{D} \cdot K \cdot \Big(T_x(Q) - T_{liquid}(Q)\Big), \qquad (4.9)$$

where K is a flow-rate-independent constant that characterizes the heat conduction rate from film to the liquid. Nu is Nusselt number, i.e. the ratio of convective to conductive heat transfer rate. D is the hydrodynamic diameter of fluidic channel, and approximately equals $2wh/(w+h)$ for a rectangular channel. Note that a different constant H_1 is used here in place of H_0 in Eq. 4.8 for the direct heat transfer from hot film to PC cladding, since H_0 also includes the conductive heat transfer through the liquid to PC cladding (see Figure 4.6).

To simplify our derivation, we define an effective zero-flow temperature T':

$$T' \equiv T_0 + \frac{(H_0 - H_1) \cdot (T_0 - T_{RT})}{H_1 - \alpha \cdot H_0 \cdot (T_0 - T_{RT})}, \qquad (4.10)$$

which leads to a helpful relation similar to Equation 4.8 but with H_0 replaced by H_1,

$$I^2R(T') = H_1 \cdot (T' - T_{RT}). \qquad (4.11)$$

Of the convective heat loss into the liquid (the second term of the right-hand side of Eq. 4.9), only a fraction η is absorbed by the liquid and contributes to its temperature rise from entrance temperature T_{in} to exit temperature T_{out}.

$$\eta \cdot \frac{Nu}{D} \cdot K \cdot \left(T_x - T_{liquid}(Q)\right) = Q \cdot C_{p,v} \cdot (T_{out} - T_{in}) \tag{4.12}$$

Substituting Eq. 4.12 into the second term of the right-hand side of Eq. 4.9, we arrive at:

$$\eta \cdot \left(I^2R - H_1(T_x - T_{RT})\right) = Q \cdot C_{p,v} \cdot (T_{out} - T_{in}). \tag{4.13}$$

The film temperature T_x at a given flow rate Q can then be solved as:

$$T_x = \frac{\left(0.5\eta NuK + QC_{p,v}D\right)(I^2R(T_x) + H_1T_{RT}) + QC_{p,v}NuKT_{in}}{\left(0.5\eta NuK + QC_{p,v}D\right)H_1 + QC_{p,v}NuK}. \tag{4.14}$$

In fiber flow sensors, H_1 is mostly limited by free heat convection to air, and $(Nu/D)\cdot K$ represents the forced heat convection to liquid. Hence, $(Nu/D)\cdot K$ is much greater than H_1. Thus Eq. 4.14 can be written as

$$T_x = \frac{0.5\eta H_1\left(1 - \alpha \cdot (T' - T_{RT})\right) \cdot T' + QC_{p,v} \cdot T_{in}}{0.5\eta H_1\left(1 - \alpha \cdot (T' - T_{RT})\right) + QC_{p,v}}. \tag{4.15}$$

To further simplify this expression, we define a saturation flow rate Q_0 as:

$$Q_0 \equiv \frac{0.5\eta H_1\left(1 - \alpha \cdot (T' - T_{RT})\right)}{C_{p,v}} = \frac{0.5\eta l \int_P h_1 \, \mathrm{d}P\left(1 - \alpha \cdot (T' - T_{RT})\right)}{C_{p,v}}. \tag{4.16}$$

Here Q_0 represents the transition flow rate between linear regime and saturation regime, which will be clear in later discussions. Hence, Equation S13 becomes a simple expression:

$$T_x(Q) = T' - \frac{Q/Q_0}{(1 + Q/Q_0)} \cdot (T' - T_{in}). \tag{4.17}$$

It is worth noting that for low flow rates, η becomes strongly dependent on flow rate, which causing Q_0 also be Q-dependent. Our one-dimensional theory here assumes a largely Q-independent η, and thus its accuracy requires the following minimal flow rate (according to finite-element analysis): for a single-segment sensor, Q_0 can be treated as Q-

independent when flow rate is greater than 5 uL/min; for an eight-segment sensor, flow rate needs to be greater than 5 (for Segment #2) to 20 uL/min (for Segment #7).

Eq. 4.17 predicts three regimes in the temperature response of fiber flow sensors: a dead regime when $Q \to 0$; a linear regime when $Q \ll Q_0$; and a saturation regime when $Q \gg Q_0$.

Regime 1: dead regime

At near zero flow rate ($Q \to 0$), practically all of the heat flux into the liquid dissipates into unheated cladding materials ($\eta \to 0$). The sensor exhibits nearly zero temperature sensitivity.

Regime 2: linear regime

At the low flow rate limit ($0 \ll Q \ll Q_0$), T_x is proportional to flow rate Q.

$$T_x(Q) = T' - T_{in} \cdot Q/Q_0. \tag{4.18}$$

The transition between dead regime and linear regime is defined by the flow rate where the linear response curve intersects the zero-flow sensor temperature ($T_0 = T' - T_{in} \cdot Q/Q_0$), which is solved as:

$$Q_{\min} = \frac{T' - T_0}{T_{in}} Q_0. \tag{4.19}$$

Regime 3: saturation regime

At the high flow rate limit ($Q \gg Q_0$), T_x gradually approaches the entrance temperature of liquid T_{in}. The transition between linear regime and saturation regime locates at the saturation flow-rate Q_0, where sensor temperature can be determined by:

$$T_{1/2} \equiv T_x(Q_0) = 0.5 \cdot (T' + T_{in}). \tag{4.20}$$

The saturation occurs when the convective cooling far exceeds the conductive cooling and the thermal boundary layer extends beyond the streamwise extension of the

sensor. [56] Eq. 4.16 reveals that the saturation flow rate Q_0 can be increased with longer sensors, although one has to sacrifice temperature sensitivity (dT/dQ) for a given temperature rise (T'-T_{in}).

Fortunately, we can decouple this fundamental trade-off between flow sensitivity and the saturation flow rate by partitioning a long hot film into multiple, independent segments, allowing high sensitivity at various flow rates to be measured off different segments. To understand this multi-segment structure, we extended our first order temperature response theory for multi-segment sensors.

4.5.2 Temperature response of a multi-segment sensor

Furthermore, we can extend our previous model to solve the temperature response recursively for a sensor consists of N consecutive segments. The film temperature at segment i, $T_x^{(i)}$, can be expressed by Eq. 4.17 as:

$$T_x^{(i)} = T' - \frac{Q/Q_0}{(1+Q/Q_0)} \cdot \left(T' - T_{in}^{(i)}\right). \tag{4.21}$$

Note that the entrance temperature of liquid $T_{in}^{(i)}$ is heated up be previous segment, and equals the exit temperature of previous adjacent segment.

$$T_{in}^{(i)} = T_{out}^{(i-1)}.$$

Now considering the next adjacent segment (i+1), similarly to Eq. 4.21, we have the film temperature $T_x^{(i+1)}$ written as:

$$T_x^{(i+1)} = T' - \frac{Q/Q_0}{(1+Q/Q_0)} \cdot \left(T' - T_{in}^{(i+1)}\right). \tag{4.22}$$

Subtract Eq. 4.21 from Eq. 4.22, and substitute that $T_{in}^{(i+1)} = T_{out}^{(i)}$. We may obtain:

$$T_{out}^{i} - T_{in}^{i} = \frac{1+Q/Q_0}{Q/Q_0}\left(T_x^{(i+1)} - T_x^{(i)}\right). \tag{4.23}$$

Combing Eq. 4.23 and Eq. 4.9, we can solve out the film temperature $T_x^{(i+1)}$ as a function of the film temperature of previous segment $T_x^{(i)}$:

$$T_x^{(i+1)} = \frac{1}{1+Q/Q_0}T' + \frac{Q/Q_0}{1+Q/Q_0}T_x^{(i)}. \quad (4.24)$$

By Eq. 4.24, the temperature response for N-segment fiber sensors can be determined recursively as:

$$T_N = T' - \left(\frac{Q/Q_0}{1+Q/Q_0}\right)^N \cdot (T' - T_{in}). \quad (4.25)$$

Max-sensitive flow rate

Equation 4.25 reveals the polynomial dependence in multi-segment sensors (N>1) instead of linear dependence in single-segment sensors. In the limit of $Q \ll Q_0$, T_N is a N-order polynomial function of flow rate Q. In high flow rate range, all segments still saturates towards the entrance temperature of liquid T_{in}, but with a much reduced rate because of the Nth polynomial. Very importantly, such delay indicates the potential to extend measurement range by constructing multiple segments, which is clearly seen in the value of max-sensitive flow rate for each segment, a parameter that characterize the flow rate associated with highest temperature sensitivity.

The temperature sensitivity of multi-segment sensors can be evaluated by taking the first-order derivative of T_N with respect to flow rate Q:

$$S = \frac{\mathrm{d}T_N}{\mathrm{d}(Q/Q_0)} = -N(T' - T_{in})\left(\frac{Q/Q_0}{1+Q/Q_0}\right)^{N-1}\left(\frac{1}{1+Q/Q_0}\right)^2 . \quad (4.26)$$

Max-sensitive flow rate locates the point where the derivation of S equals to zero, which can be calculated as:

$$\frac{\mathrm{d}S}{\mathrm{d}(Q/Q_0)} = -N(N-1-2Q/Q_0)(T' - T_{in})\left(\frac{Q/Q_0}{1+Q/Q_0}\right)^{N-2}\left(\frac{1}{1+Q/Q_0}\right)^4 = 0. \quad (4.27)$$

By solving Eq. 4.27, we arrive at the expression of max-sensitive flow rate:

$$Q_s = 0.5 \cdot (N-1)Q_0. \quad (4.28)$$

When treating flow sensors operating at completely different measurement range, it can be unfair to compare their sensitivity directly. For example, a sensor working in 1-

10 L/min cannot have the same temperature sensitivity as another sensor in 1-10 nL/min unless its temperature rise being 10^9 times greater. Instead, we use relative sensitivity ($\mathrm{d}T/(\mathrm{d}Q/Q)$) to compare them. Thus, we introduce another parameter Q_{rs}, which refers to the flow rate associated with highest relative sensitivity. Q_{rs} can be calculated by following a similar procedure as how we calculated Q_s, and it turns out to be:

$$Q_{rs} = NQ_0. \tag{4.29}$$

As we can see from Eq. 4.29 and Eq. 4.28, both Q_s and Q_{rs} grow linearly with segment index *N*, suggesting that we can construct longer hot films with multiple segments to delay saturation without affecting the high sensitivity of the first several segments.

Estimation of axial heat loss

The hot film temperature of a single-segment sensor is 45 ^{o}C at zero flow rate and 1.67 mA injected current. Thus total heat conduction rate H_0 is obtained from Eq. 4.8 as 2.9 mW/K. By following the same procedure, we calculate H_0 for an eight-segment to be 0.94 mW/K, much less than the value for a single-segment sensor. One main reason for this significant different is the axial heat loss into adjacent colder contact regions, as we can see in Figure 4.7. Contact regions are much colder than adjacent sensor regions because of a larger heat dissipation rate as well as near zero heat generation (P=I^2R). A single-segment sensor has two contact regions, whereas an eight-segment sensor has 7/6 contact regions in average.

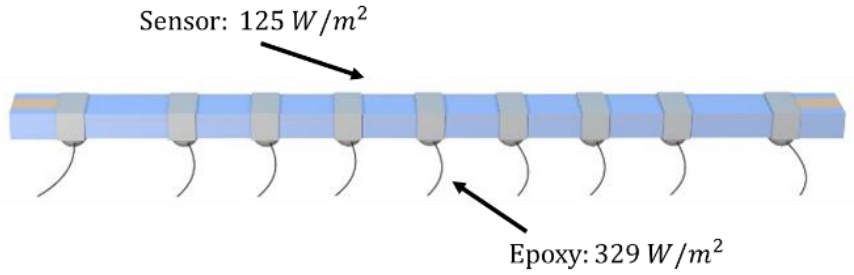

Figure 4.7. Large heat loss at the contact regions.

4.6 FINITE ELEMENT SIMULATIONS

First-order theory usually involves many approximations (see approximation 1,2, and 3), which might lead to completely off results. To validate our model, a first principle finite element calculation is necessary, especially for multi-segment sensor.

4.6.1 Simulation setup for a multi-segment sensor

A 2D first-principle finite-element-method (FEM) analysis [60] is conducted on the side view plane of multi-segment sensors to validate our one-dimensional theory and explain measurement results later. Here we assume the impact of temperature distribution along the width is of secondary important. Conjugate heat transfer module is chosen to simulate the heat transfer process in a system that involves both solids and liquids. The entrance temperature for liquid is 23.56 ºC, and room temperature T_{RT} is 23.98 ºC. The boundary condition for solid/air interfaces is set as $Q = h \cdot (T_{solid} - T_{RT})$, where T_{solid} is the temperature of solids at the interface. The simulations use fitted values for heat transfer rate *h*: 125, 161 and 329 W/(K·m^2) for polycarbonate, silver paint and conductive epoxy, respectively. Device dimensions are also fitted with a maximum 0.2 mm off allowed from designed dimensions to account for fabrication error. The design value is 2 mm for

segment #2 to #7, while the fitted values are 3.7, 1.5, 2.3, 2.1, 2.0, 2.2, 2.2, and 2.8 mm for Segment #1 to #8.

4.6.2 Predicted temperature distribution of a multi-segment sensor

Previously, our first-order theory has revealed that max-sensitive flow rate increases as segment index increases, which can be explained by the evolution thermal boundary layer. Figure 4.8 shows the temperature distribution of an eight-segment sensor at various flow rates. As we can see, the thermal boundary layer, the region with the steepest temperature gradient (~32°C, cyan/green region), extends towards downstream as flow rate increases. Below 42 µL/min, this layer is localized within Segment #2, which produces the highest flow-rate sensitivity among all segments. At flow rates beyond 127 µL/min, this layer moves downstream to Segment #7, which provides high sensitivity while upstream segments are deeply saturated.

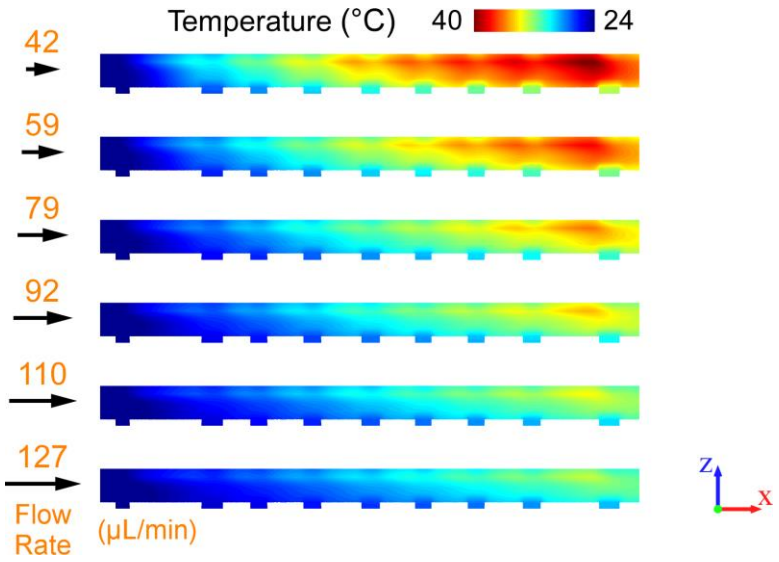

Figure 4.8. Calculated temperature distribution along the length of a multi-segment fiber sensor at various flow rates using a finite-element solver.

4.6.3 Match between FEM and first-order theory

Figure 4.9 shows the distribution of hot film temperature calculated from first-order theory (grey curves) and finite element solver (colored curves) at various flow rates. 1D temperature distribution is extracted from the temperature distribution of solid/air interface (top horizontal edges in Figure 4.8) in 2D FEM simulation. The temperature of each segment (peak values) are used to fit with our first-order theory across all flow rates. The fitted Q_0 and T' are 16.97 μL/min and 39.43 ºC, respectively.

First-order theory doesn't take into account of the contact regions, hence no temperature sink appears in grey curves. Otherwise, our analytical polynomial model matches first-principle FEM simulation very well.

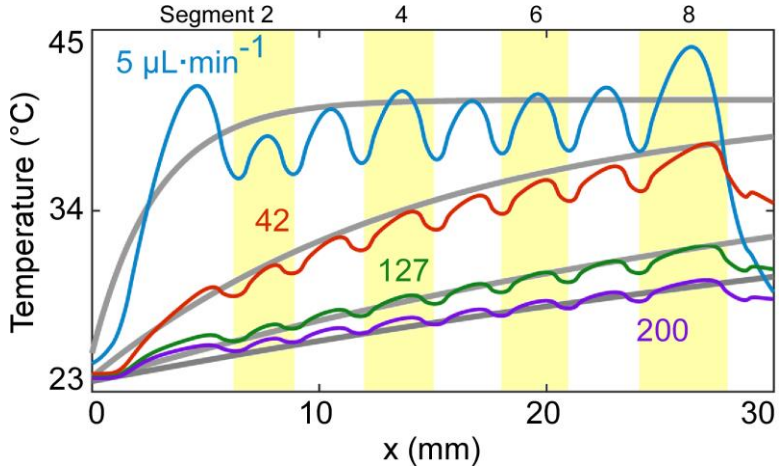

Figure 4.9. Calculated hot-film temperature from the finite-element solver (colored curves) and the analytical polynomial response from Equation 4 (grey curves) at various flow rates. The yellow areas denote Segment #2, #4, #6 and #8.

So far, both FEM simulation and first-order theory have revealed the extension of measurement range in multi-segment sensors. In next section, we will finally validated those predictions experimentally.

4.7 Demonstration of Multi-segment Flow Sensors

Previously, we developed a first-order temperature response theory, and used this theory to predict a multi-segment structure, which could efficiently extend the flow-rate range. In this section, we conduct the test for an eight-segment flow sensor, and explore how much measurement range could get extended.

4.7.1 Device preparation and test condition

Figure 4.10 presents the structure of an eight-segment flow sensor. A 5-cm-long fiber sensor segment was prepared the same way as described in 2.3.1. Nine 1-mm-long surface contacts were constructed as an equal spacing of 2 mm for each sensing segments. The first and last contacts establish a constant heating current in a 3-cm-long hot film, and the middle six segment each provides a voltage signal that reflects the local hot-film temperature. The fiber were tested with the same setup as discussed in 4.4.1 under a constant-current of 1.1 mA.

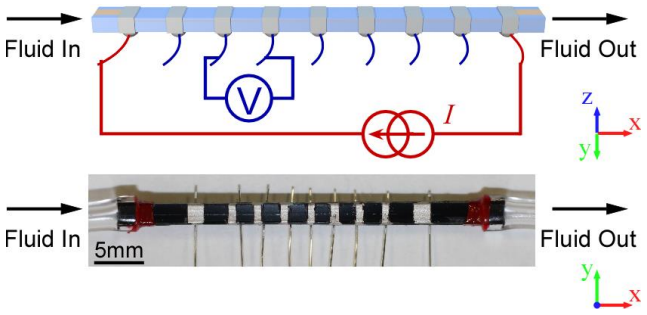

Figure 4.10. Schematic (top panel) and photograph (bottom panel) of an eight-segment sensor.

4.7.2 Responses of multi-segment flow sensors

Under a constant current of 1.1 mA, the temperature responses of an eight-segment flow sensors (six sensing segments) were measured over various flow rates from 0 to 5000

µL/min, and match accurately with both the 2D finite-element simulations (Figure 4.11) and the 1D analytical model (Figure 4.12). Individual segment shows ~2°C temperature inhomogeneity at zero flow (Figure 4.11 left panel), which is consistent with the additional axial conductive heat loss near the fiber ends (Segment #2, #7) and at the electrical contacts (both factors included in the finite-element simulations, see 4.6). Starting from zero flow, the film temperature T' falls with an increasing flow rate and converges to the liquid temperature of 24 °C in the high flow-rate limit. More importantly, as predicted in 4.5.2, the flow rates associated with peak sensitivity increase linearly to segment index N, indicating the delayed on-set of saturation in downstream segments. Here, the fitted effective N closely follows the physical segment index (Figure 4.12 inset), as $N_{\text{effective}} = 1.00 \cdot N_{\text{physical}} + 0.019$. Overall, measured relative flow-rate sensitivity ($\partial T/(\partial Q/Q)$) peaks at 4.96 K in Segment #2 for flow rates between 15 and 35 µL/min, and gradually shifts downstream at higher flow rates, with the sensitivity remains 4.87 K in Segment #7 for a flow rate as high as 120 µL/min.

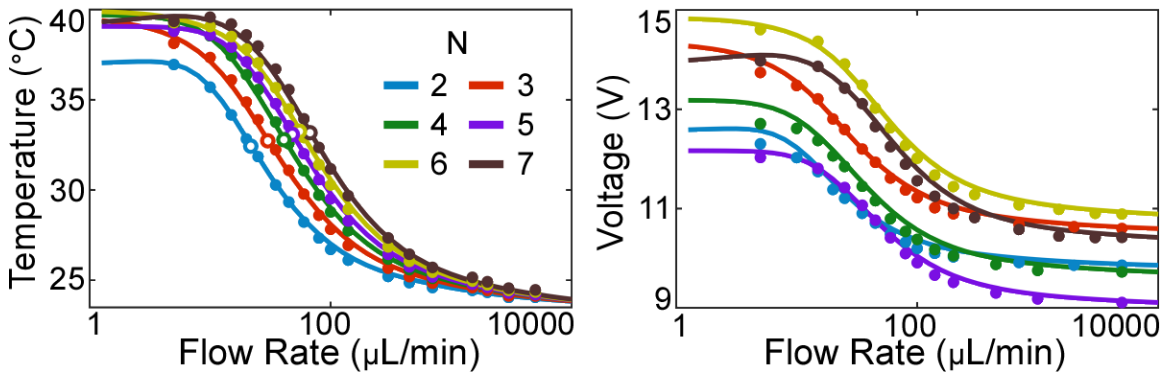

Figure 4.11. Temperature (left panel) and voltage (right panel) responses (dots) of multi-segment flow sensors in good agreement with FEM calculation (curves).

The associated voltage responses exhibit similarly good agreement with finite-element simulations (Figure 4.11 right panel), computed using the measured TCR constant

and the room-temperature resistance R_0 of each segment at low current (0.2 mA). In comparison to the temperature responses, the larger spread in the voltage responses results from length-variation and the associated R_0-variation of the segments manually defined by silver paint. For example, the shortest segment (#5) exhibits lowest voltage response. Nevertheless, flow rate sensitivity ($\partial V/(\partial Q/Q)$) remains greater than 0.75 V between 10 and 200 µL/min. In terms of pressure drop, since the 2 or 3-mm-long individual segment is much shorter than the overall length (5 cm) of a fiber segment tested earlier (see 2.4.2), the pressure drop of the eight-segment sensor is comparable to that of a single-segment sensor, both around 8 Pa at 100 µL/min.

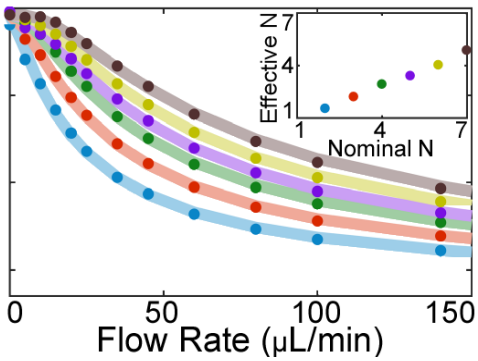

Figure 4.12. Measured temperature responses (dots) in low flow rate region in good agreement with the 1d analytical heat transfer theory. Inset compares the fitted effective segment index and the physical segment index.

The 5-fold increase in the measurement range from a single-segment sensor (5~40 µL/min) to a multi-segment sensor (5~200 µL/min) can be further improved in several ways. From the measurement standpoint, if we measure multiple segments simultaneously, the linear regression of the temperatures T_N, which follows a t_{n-2} distribution with n being the sample size, not only reduces confidence interval of the T_N-N slope (a quantity inverse to the flow rate Q at high flow rate), but also reveals the flow direction and greatly reduces

drift errors (e.g. room temperature fluctuation). For instance, a change in room temperature by 0.1 °C perturbs the hot-film temperature rise by 10-100% at $100Q_0$, as predicted by the analytical temperature response equation, while affecting the T_N-N slope by less than 1%. On the other hand, from the structural standpoint, the fiber fabrication process allows active sensing segments to be separated by exponentially-increasing lengths of heater segments, which helps to distribute the peak sensitivity ranges contributed by each sensing segment in a logarithmic fashion (commensurate with a multi-decade dynamic range). This approach also introduces longer and more powerful heater needed for high flow-rate measurements. In addition, in the low-flow rate regime, sensitivity can be enhanced further by better thermal insulation of the fluidic channel, which can be realized through incorporating additional hollow cores in the fiber.[51], [56]

To summarize this chapter, we have reported a new form of fiber-based integrated flow-rate sensors, which overcome the inherent trade-off between sensitivity, pressure drop and measurement range, using novel materials and structures unique to fiber drawing process [5], [11], [12]. The successful implementation of high-TCR, high-resistance CPE as the temperature-sensitive hot film yields a voltage-temperature response of 0.8 V/K and a flow-rate sensitivity of 384 mV/(uL·min^{-1}) between 0 and 20 μL/min. This ultrahigh voltage-temperature response allows the sensor to operate with a maximum temperature rise of merely 20 °C, 5~10× smaller than that in typical MEMs sensors [58] and especially important for handling biomedical samples. In addition, this ultrahigh voltage response also enables ultralow pressure drop of 8 Pa at 100 μL/min, orders of magnitude lower than conventional MEMs thermal flow sensors. More importantly, we have achieved a high-sensitivity measurement range of 5~200 μL/min through a multi-segment structure where each segment reaches its peak sensitivity at different flow rates. This new form of fiber

flow sensor opens up new opportunities for constructing large-scale multi-chip microfluidics systems especially in temperature-sensitive applications.

Chapter 5: Optimization of Fiber Flow Sensors

In this chapter, we conduct the theoretical optimization of fiber flow sensors, which consists of three steps: cross-sectional design, longitudinal design and novel multi-segment structures. For each case, we first apply and extend our first-order 1D heat transfer model to provide the basic guideline for optimization, and then we verify our analytic guideline with FEM simulations. This part of work is not only a natural extension of previous project in Chapter 4, but also a trailblazer for developing novel devices with distributed sensing in next chapter.

5.1 Motivation of Optimization

Previously, we have reported the world's first fiber-based flow sensors using novel materials and device structures, which resolve a fundamental trade-off between sensitivity, pressure drop, measurement range, and temperature rise in conventional MEMs flow sensors. However, we have not done too much work as regards the geometric optimization of fiber sensors, and a few device parameters, such as sensitivity or dynamic range, remain to be improved. Thus, a systematic optimization of fiber flow sensors becomes necessary.

Current fiber flow sensors still suffer two major limitations: large overlap between the responses of each segment and tedious post-drawing process. As we have measured previously in 4.7.2, the measurement ranges of segment #1 to #7 are 0-20, 10-80, 15-100, 15-140, 15-200, 25-200, 25-200 μL/min, respectively. Over 95% of the flow rate range from 0 to 200 μL/min are coved by multiple segments simultaneously, which is obviously unnecessary. Ideally, the temperature responses of a multi-segment sensor should cover a wider range with less overlap between them, as seen in Figure 5.1. An enhanced sensitivity and an optimized segmentation can potentially help to resolve this issue.

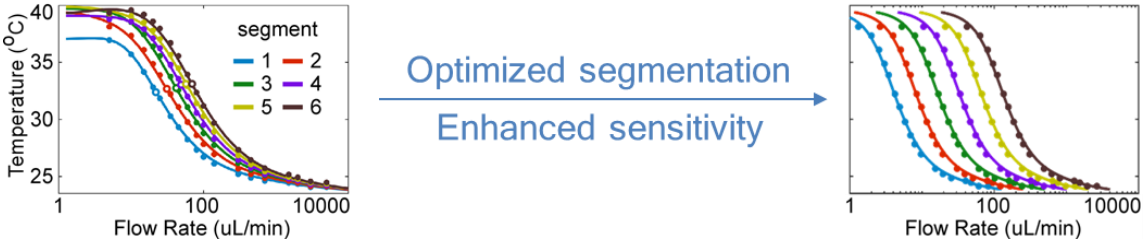

Figure 5.1. Current (left panel) and optimized (right panel) of the temperature responses of each segment in a multi-segment sensor.

Other than large overlap, their tedious post-drawing process not only limits the scalability of current multi-segment sensors, but also reduces the fabrication yield. One of the benefits from fiber drawing is its scalability: kilometers of fiber can be obtained with a single draw. However, the current device configuration requires constructing N+1 external contacts for a N-segment sensor after the fiber drawing (see Figure 5.2), which cannot be scaled up easily. Thus, a smarter segmentation is required to use less surface contacts for the same device performance.

Figure 5.2. Current (left panel) and optimized (right panel) configuration of a multi-segment sensor.

Overall, those associated limitations could affect the future applications of fiber flow sensors as functional microfluidics interconnects. It is hence important to conduct a theoretic optimization to resolve those potential issues. Specifically, the optimization in this chapter consists of three steps: a cross-sectional design, as well as a longitudinal design to boost sensitivity, and a segmentation design to decreases the complexity of post-drawing process.

5.2 Cross-sectional Design

Previously, we have presented the fabrication of fiber sensors in Figure 2.2. Such a preform assembly has required the cross-sectional geometry being based on two rectangles: one for the fluidics channel, and one for the overall fiber. Thus, there are four designable parameters to be optimized: channel width w, channel height h, cladding width w_c and cladding height h_c, as seen in Figure 5.3.

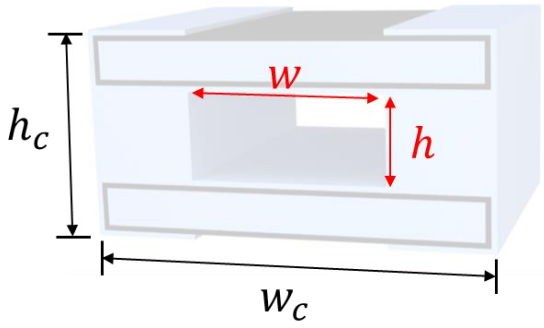

Figure 5.3. Parameters to be optimized in cross-sectional design.

5.2.1 Design guideline from analytic model

As derived in 4.5.1, our analytical heat transfer model predicts the temperature response $T(Q)$ of a single-segment sensor to be:

$$T(Q) = T' - \frac{Q/Q_0}{(1 + Q/Q_0)} \cdot (T' - T_{in}), \tag{5.1}$$

where Q is the volumetric flow rate, T' is the start temperate at zero flow rate, and T_{in} the entrance temperature of liquid. Q_0 is the transition flow rate between linear regime and saturation regime, a parameter defined as:

$$Q_0 \equiv \frac{0.5\eta H_1\big(1 - \alpha \cdot (T' - T_{RT})\big)}{C_{p,v}}. \tag{5.2}$$

where η is the fraction of heat absorbed by the liquid, T_{RT} is room temperature, α is TCR constant, $C_{p,v}$ is the specific heat of liquid, and H_1 is conductive heat dissipation

rate. Among all factors that affect Q_0, H_1 is the one that is closely tied to the geometry of fibers. For a sensor that operates within linear regime, its measurement range is approximately equal to Q_0, and hence its sensitivity is $\Delta T/Q_0$, where ΔT is the temperature rise at zero flow. As a consequent, we can decrease H_1 to increase sensitivity.

H_1 characterizes the overall heat dissipation rate, mainly including two paths: cross-sectional heat loss and axial heat loss (see Figure 5.4). Cross-sectional loss Q_{cs} denotes the heat loss through the entire outer surface of cladding, expressed by fiber length l, cladding surface temperature T_s as:

$$Q_{cs} = l \int_P h_{SG} \, (T_s - T_{RT}) \mathrm{d}P. \tag{5.3}$$

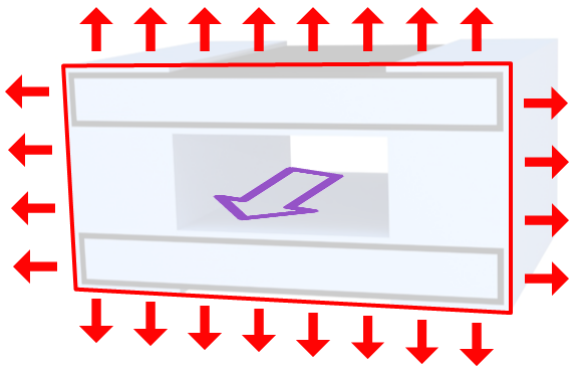

Figure 5.4. Two paths of conductive heat loss: cross-sectional heat loss (red arrow) and axial heat loss (purple arrow).

h_{SG} refers to the free convective heat transfer rate between cladding and air. $\int_P \mathrm{d}P$ denotes the integration over the perimeter of cladding. In most circumstances, the heat conduction within cladding is significantly faster than the free convection into air. As a result, T_s is close to a constant along the perimeter of cladding. We simplify the equation above to arrive at the following equation:

$$Q_{cs} = 2h_{SG} l(w_c + h_c) \cdot (T_s - T_{RT}). \tag{5.4}$$

As for the axial heat loss Q_{ax}, it equals to the integration of heat diffusion rate over the entire cross section *S*:

$$Q_{ax} = \int_S k\left(\frac{\partial T}{\partial l}\right) \mathrm{d}S. \tag{5.5}$$

Similarly, by approximating the temperature distribution to be constant within cladding and channel, we arrive as:

$$Q_{ax} = k_{liquid} wh \cdot (T_l - T_{RT}) + k_{liquid}(w_c h_c - wh) \cdot (T_s - T_{RT}). \tag{5.6}$$

Overall, combine the expression for Q_{cs} and Q_{ax}, and substitute them into the expression for Q_0. Sensitivity becomes:

$$S \propto \frac{1}{\left(2h_{SG} l(w_c + h_c) + k_{liquid}(w_c h_c - wh)\right) \cdot (T_s - T_{RT}) + k_{liquid} wh \cdot (T_l - T_{RT})}. \tag{5.7}$$

Or simply,

$$S \propto \frac{1}{\mathrm{c}_1(w_c + h_c) + c_2 w_c h_c + c_3 wh}, \tag{5.8}$$

where c_1, c_2 and c_3 are all non-geometry-related constants. The equation above reveals that sensitivity S is inverse to device dimensions, which agrees with what we have intensively discussed in 4.2.1. In the rest of this section, we break down this equation to discussion how channel sizes and cladding sizes affect sensitivity separately.

Effects of channel dimensions on sensitivity

Sensitivity is inverse to channel area ($1/S \propto wh$). If we fix channel area, sensitivity does not change with aspect ratio (w/h).

Effects of cladding dimensions on sensitivity

Sensitivity is directly related to both the area and the perimeter of cladding, expressed as:

$$\frac{1}{S} \propto \mathrm{c}_1(w_c + h_c) + c_2 w_c h_c. \tag{5.9}$$

For a short segment, axial dissipation dominates overall conductive heat dissipation ($c_1(w_c + h_c) \ll c_2 w_c h_c$). As segment gets longer, cross-sectional heat dissipation increases, and eventually dominates overall conductive heat dissipation ($c_1(w_c + h_c) \gg c_2 w_c h_c$).

Effects of thin cladding on sensitivity

The discussions above are all based on the assumption that liquid temperature and cladding temperature can both approximated as constants over the entire cross-section. This assumption is usually valid since heat transfer in solids is significantly faster to free convection into air. However, it fails when fiber sensors contain thin cladding structure. As we can see in Figure 5.5, thin cladding structure limits the heat transfer into surrounding solids, and hence focuses the high temperature regions (hot zone) in a limited area. As a result, the associated cross sectional heat loss is usually much smaller for a structure with thin cladding, which makes it an effective way to boost sensitivity.

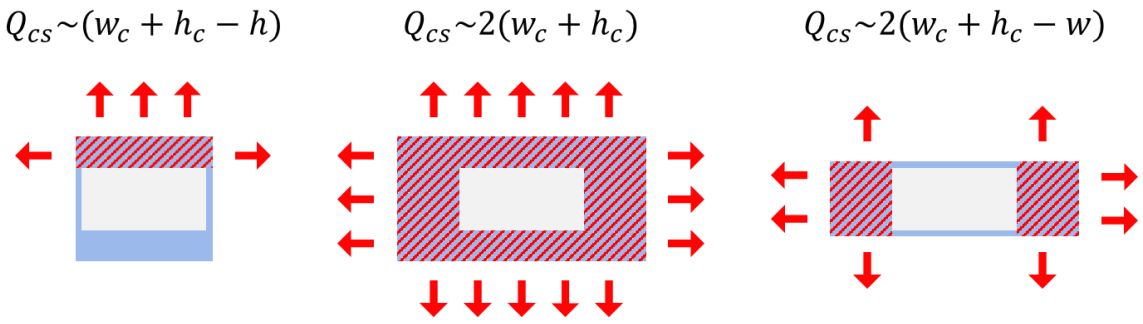

Figure 5.5. Hot zone (pattern-filled region) for cross sections with (left and right) and without (middle) thin cladding. The formulas on the top represent the corresponding cross-sectional heat loss.

5.2.2 Match between FEM and analytical guideline

To validate our design guideline from analytical model, we conduct several FEM simulations to reveal the relation between sensitivity and cross sectional geometry. The simulation setup involves 3D conjugate heat transfer module with stationary solver. Both the entrance temperature for liquid and room temperature are set at 24 ^{o}C. The boundary condition for solid/air interfaces is set as $Q = h \cdot (T_{solid} - T_{RT})$, where T_{solid} is the temperature of solids at the interface. The values of heat transfer rate h are 125, 161 and 329 W/(K·m^2) for polycarbonate, silver paint and conductive epoxy, respectively. Device dimensions are subject to change in each case, as we will discuss in details later.

FEM simulations at various channel geometries

To validate analytical prediction of $1/S \propto wh$, we conduct intensive simulations to sweep the three parameter spaces as listed in Table 5.1. By the analytical formula, the reciprocal of sensitivity is linear to w, or h, and is not sensitive to w/h.

Table 5.1. Parameter spaces for FEM simulations at various channel geometries.

Parameter Space	**Constant**	**Dependence**	**Start Point B ($\alpha = 0$)**	**End Point A ($\alpha = 1$)**
Width w	Height h	Linear	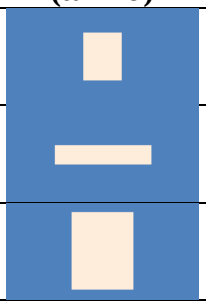	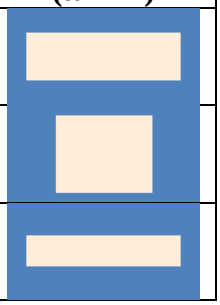
Height h	Width w	Linear		
Aspect ratio w/h	Area wh	Insensitive		

Figure 5.6 shows the simulated dependence of 1/S on channel geometries. $1/S$ behaves linear to w and h, and indeed not sensitive to w/h. In other words, we achieved near-perfect agreements between FEM and analytical guideline.

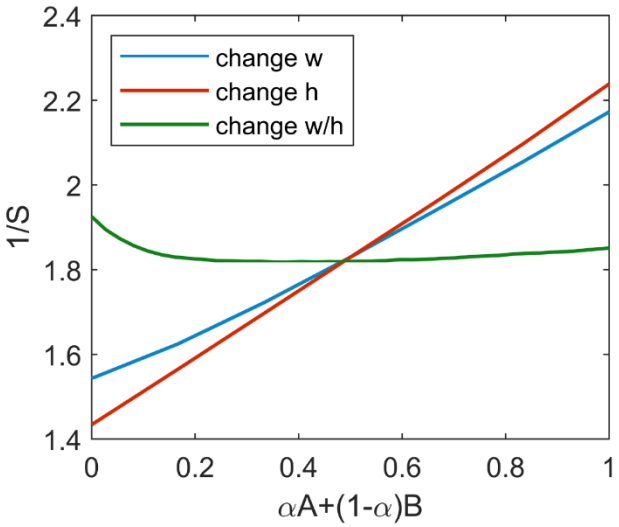

Figure 5.6. Dependence of the reciprocal of sensitivity on channel geometries simulated with a FEM solver.

FEM simulations at various cladding geometries

By our analytical formula, the reciprocal of sensitivity $1/S$ is linear to $c_1(w_c + h_c) + c_2 w_c h_c$. To validate it, we conduct a number of simulations to sweep parameter spaces of cladding geometry, as listed in Table 5.2.

Table 5.2. Parameter spaces for FEM simulations at various cladding geometries.

Parameter Space	**Constant**	**Dependence**	**Start Point B ($\alpha = 0$)**	**End Point A ($\alpha = 1$)**
Width w_c	Height h_c	Linear	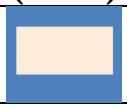	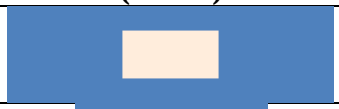
Height h_c	Width w_c	Linear		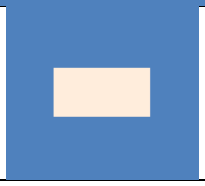
Aspect ratio w_c/h_c	Area $w_c h_c$	Sensitive	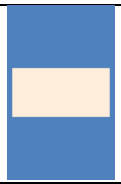	

Our analytical formula predicts that $1/S$ increases linearly to cladding width and height. It is also sensitive to cladding aspect ratio, unlike channel aspect ratio. Moreover, as we seen from the fourth and fifth columns in Table 5.2, the two ends of all three parameter spaces contain thin cladding structures, especially for the last parameter space of aspect ratio. Consequently, we expect that in the results from FEM 1/*S* does not strictly follow the predictions listed in Table 5.2. Instead, the results should exhibit valleys at two ends of each parameter space.

Figure 5.7 shows the simulated dependence of 1/*S* on cladding geometries. 1/*S* behaves quasi-linear to *w* and *h*, and sensitive to *w*/*h* as well. More importantly, we observe two valleys at the ends of each parameter space, especially for the case of aspect ratio.

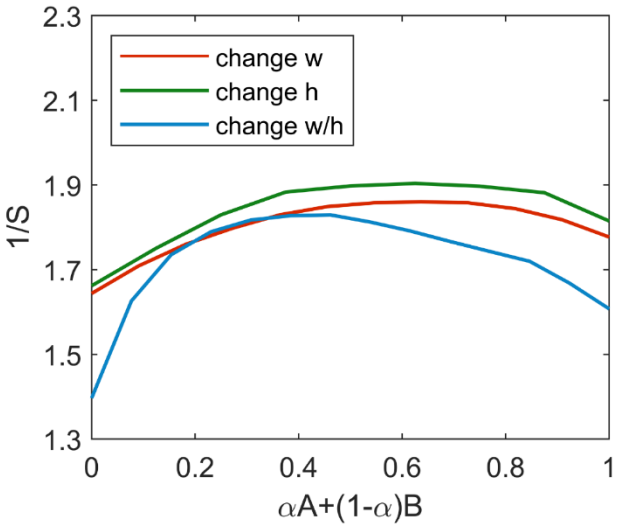

Figure 5.7. Dependence of 1/*S* on cladding geometries simulated with a FEM solver.

5.2.3 Optimized design for cross-sectional geometry

With the knowledge of how cross-sectional geometry affects sensitivity, we can optimize the cross-sectional design for fiber flow sensors, which should follow two basic rules:

- Optimized geometry cannot bring extra pressure drop;
- Optimized can still be connected to Tygon tubes of 1/16" ID;

The first rule prevents us to increase sensitivity by shrinking channel sizes; whereas the second rule fixes the cladding area to be the same as the inner channel area of Tygon tubes (2 mm^2). Thus, the two designable parameters left are channel aspect ratio (green line in Figure 5.6) and cladding aspect ratio (blue line in Figure 5.7). Since channel aspect ratio influences both sensitivity and pressure drop at the same time, we plot both parameters together in Figure 5.8 at various aspect ratios. We choose the optimized aspect ratio to be 2 because it offers relatively larger sensitivity and lower pressure drop simultaneously.

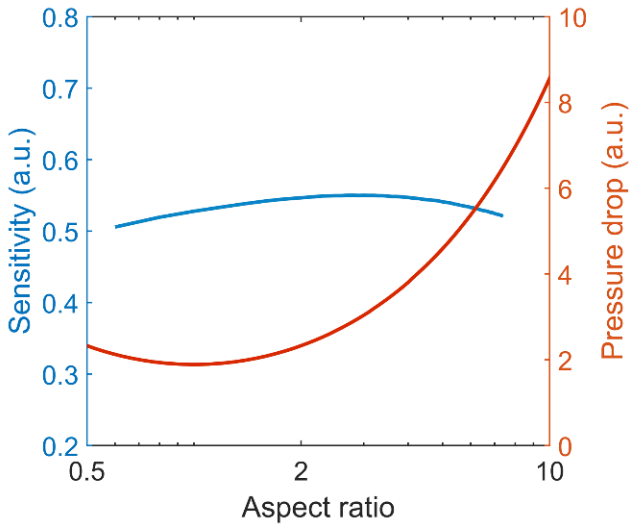

Figure 5.8. Sensitivity (blue line) and pressure drop (red line) of fiber flow sensors at various aspect ratios.

The aspect ratio of cladding does not affect pressure drop. Consequently, we simply pick the lowest point of the blue line in Figure 5.7 – a cladding width of 1.2 mm and a cladding height of 1.67 mm. Overall, the optimized cross section is given in Figure 5.9, which offers 16% improvements on sensitivity.

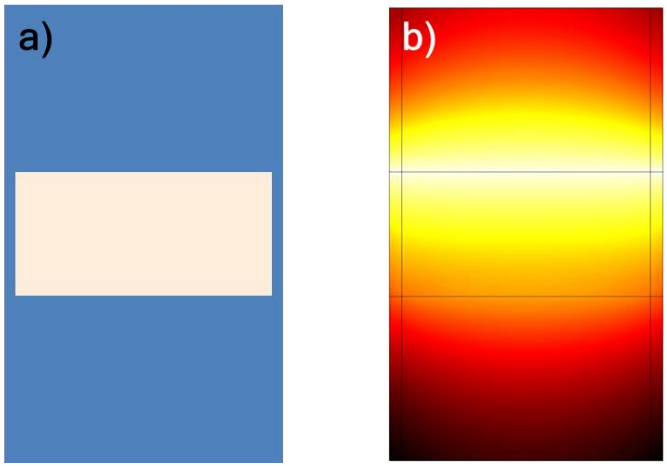

Figure 5.9. (a) Optimized cross sectional geometry and (b) corresponding temperature distribution at zero flow.

5.3 LONGITUDINAL DESIGN

Unlike cross sectional design, longitudinal design only involves one design parameter: the segment length L. Our previous discussion in 4.5 shows that Q_0 is proportional to L, hence sensitivity is inverse to L. However, this conclusion relies on the assumption that hot film temperature is constant within the segment, which obviously fails as L becomes larger. Therefore, in this section, we first extend our previous 1D temperature response theory to account for the situation where film temperature is not constant. Then with the extended analytical model, we provide the guideline for longitudinal design and verify it with FEM simulations. At last, we give the optimized longitudinal geometry.

5.3.1 Extended first-order temperature response theory

The first-order temperature response we discussed in 4.5 assumes that the temperature of hot film is constant within the segment. This assumption is valid for a short segment. As segment length becomes longer, there exists a distribution of film temperature. To resolve this distribution, we mathematically treat a single-segment sensor as a multi-segment sensor (i.e. *N* segments in Figure 5.10). As the number of segments becomes large enough, the temperature of hot film in each segment is constant. Thus, the previous model for a multi-segment sensor becomes valid.

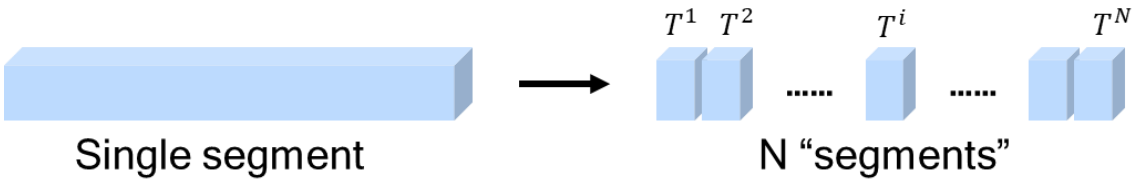

Figure 5.10. Mathematically treat a single segment as *N* segments.

With the 1D temperature response theory for multi-segment sensors given in 4.5.2, we write down the temperature response for segment #*i* to be:

$$T_i = T' - \left(\frac{Q/Q_0}{1+Q/Q_0}\right)^i \cdot (T' - T_{in}). \tag{5.10}$$

Again, Q_0 is the transition flow rate defined as:

$$Q_0 \equiv \frac{0.5\eta l \int_P h_1 \, \mathrm{d}P\left(1 - \alpha \cdot (T' - T_{RT})\right)}{C_{p,v}} \propto l. \tag{5.11}$$

Since Q_0 is proportional to the length of each segment $l = L/N$, we can re-write Q_0 as:

$$Q_0 = q_0 \cdot \frac{L}{N} \tag{5.12}$$

Substituting the above expression into the temperature response for segment #*i*, we arrive at:

$$T_i = T' - \left(\frac{NQ}{q_0 L + NQ}\right)^i \cdot (T' - T_{in}). \tag{5.13}$$

Now considering a random point *x* away from the fluidic entrance, the point locates at segment $\#i_x$, where i_x equals to $\text{round}(Nx/L)$. Substitute $\text{round}(Nx/L)$ to the temperature response for segment $\#i$, we arrive at the temperature distribution along the sensor as:

$$T(x,N) = T' - \left(\frac{NQ}{q_0 L + NQ}\right)^{\text{round}(Nx/L)} \cdot (T' - T_{in}). \tag{5.14}$$

As N approaches infinite, we derive out the limit as:

$$T(x) = \lim_{N\to\infty} T(x,N) = T' - e^{-\frac{q_0}{Q}x} \cdot (T' - T_{in}). \tag{5.15}$$

The above equation reveals an exponential distribution of hot film temperature. The temperature response is then defined as the average temperature across the entire segment, which is found to be:

$$T_{avg} = \frac{1}{L}\int_0^L T(x)\mathrm{d}x = T' - \frac{Q}{q_0 L}\left[1 - e^{-\frac{q_0 L}{Q}}\right](T' - T_{in}). \tag{5.16}$$

Fortunately, the equation above shows that sensor response still scales to $Q/q_o L$, or Q/Q_o (see Figure 5.11 for the responses predicted by two models). Thus, its sensitivity is still proportional to sensor length L.

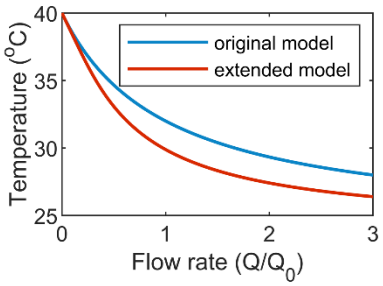

Figure 5.11. Temperature response of a single-segment sensor with original (blue line) and extended model (red line).

Discussions on short sensor segment

As sensor segment L becomes too short, we start facing a different issue: surface contact cannot establish a uniform current distribution across the sensing region. Figure 5.12 shows the current distribution for sensors of various lengths simulated with a FEM solver. At a short segment length, i.e. 0.2 mm, current only flows through the top and bottom areas, where side walls locate instead of fluid channel. For the middle region where fluid channel locates, the average current density I_{avg} is only 60% of the values calculated from a uniform distribution. As L keeps increasing, I_{avg} reaches 92% at 2 mm and 99% at 20 mm. Figure 5.13 shows the relation between I_{avg} and segment length L. As we can see, I_{avg} quickly drops as segment length shrinks.

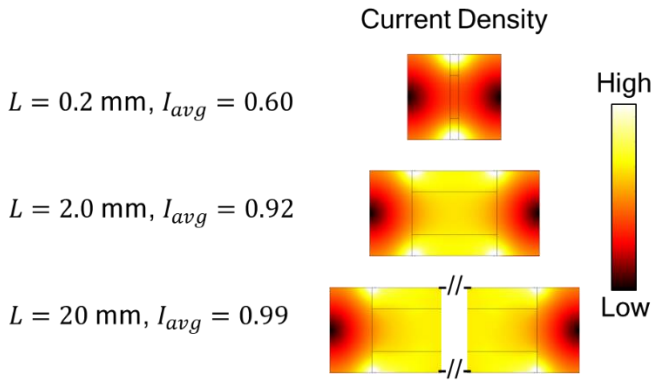

Figure 5.12. Current distribution for sensors of various length.

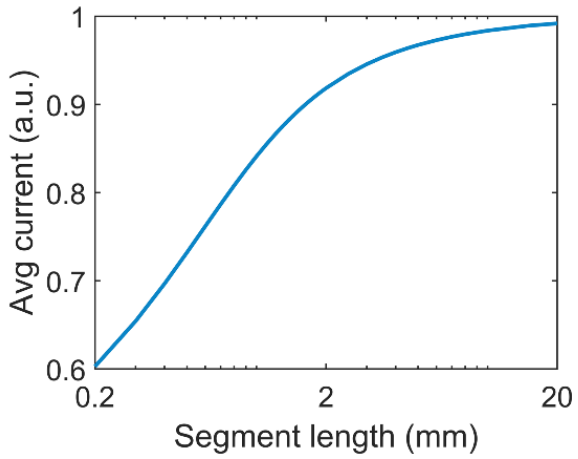

Figure 5.13. Average current amount passing through fluidic channel region at various segment length.

In other words, with a shorter segment, less current passes through the fluid channel, which subsequently reduces the sensitivity of flow sensors. Therefore, we expect to see a less steep slope at short segment length ($L < 2$ mm).

5.3.2 FEM simulations at various segment lengths

To validate the analytical prediction of $1/S \propto L$, we conduct a few simulations to sweep the segment length L from 1 to 8 mm. Figure 5.14 presents the dependence of the reciprocal of sensitivity $1/S$ on segment length L. As we see, $1/S$ is mostly proportional to L, except when the segment is short. With short segments where $L < 2$ mm, $1/S$ has a smaller slope. Both behaviors agree with our first-order predictions.

Based on the simulation results in Figure 5.14, we choose an optimized segment length to be 1 mm, which offers 4% improvements on sensitivity.

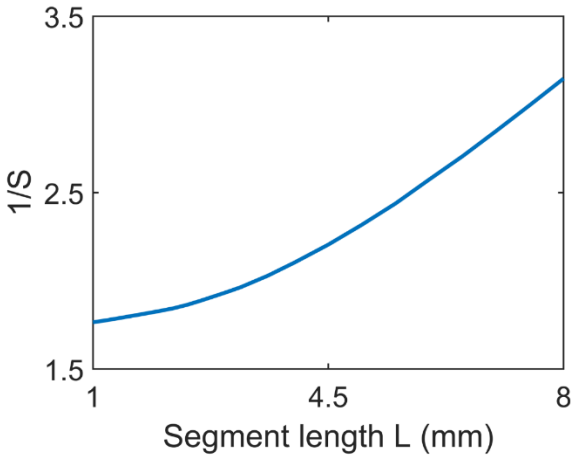

Figure 5.14. Dependence of the reciprocal of sensitivity on segment length simulated with a FEM solver.

Putting cross-sectional design and longitudinal design together, we achieve ~22% increase on sensitivity. Figure 5.15 shows the temperature responses and sensitivity before and after optimization.

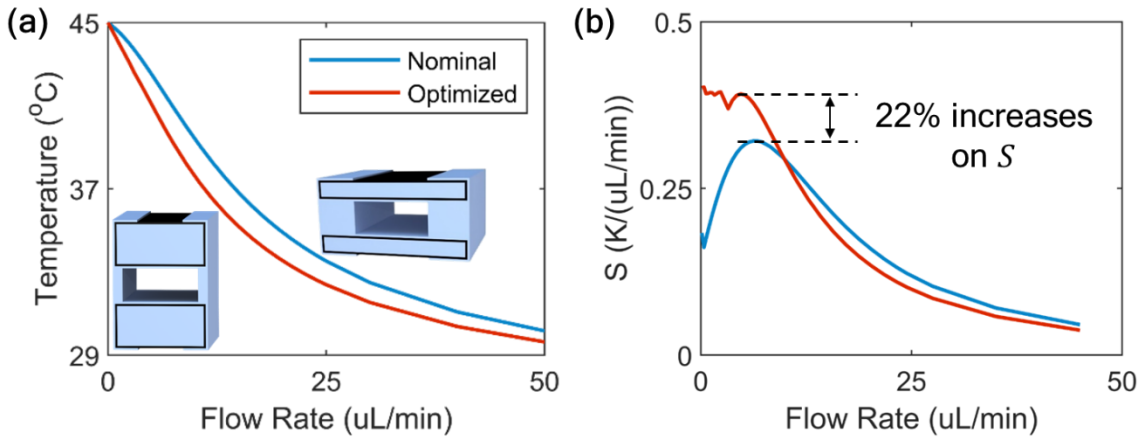

Figure 5.15. (a) Temperature responses and (b) sensitivity of nominal design (blue line) and optimized design (red line).

5.4 NOVEL MULTI-SEGMENT STRUCTURES

So far, we have arrived at an optimized geometry design for single-segment sensors (w_c=1.2 mm, h_c=1.67 mm, w=1 mm, $h = 0.5$ mm, L=1 mm), which give us 20% improvements on sensitivity over original design (w_c=2 mm, h_c=1 mm, w=1 mm, $h = 0.5$ mm, L=2 mm). Another limitation yet to be optimized is the segmental design. In this section, we explore novel device structures for multi-segment sensors to simplify the post-drawing process while maintaining or even improving the device performances.

5.4.1 Design of two-segment sensors

In multi-segment sensors as discussed in 4.5.2, each segment servers as a sensor, as well as a pre-heater for downstream segments. If we can construct a pre-heater that can adjust its heating power, a single sensing segment is enough to achieve a large dynamic range. This becomes the inspiration of two-segment sensors design.

Figure 5.16 presents the structure of a two-segment sensor, with the first segment being preheating segment and the second segment being sensing segment. The preheating segment is connected to a variable resistor R in parallel to divide a fraction of current flow. At the low limit of R ($R \to 0$), near 100% current flows through the variable resistor and no current flows through preheating segment. Thus, sensing segment behaves like a single-segment sensor, or the first segment of an N-segment sensor. At the high limit of R ($R \to \infty$), near 100% current flows through preheating segment, and sensing segment behaves like the last segment of the N-segment sensor. Overall, by adjusting the value of R, we can tune the behavior of sensing segment from the first to the last segment in a N-segment flow sensor.

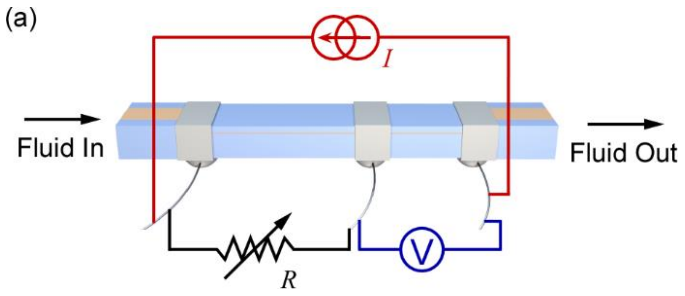

Figure 5.16. Schematic of a two-segment sensor.

Figure 5.17 shows the temperature responses of a two-segment flow sensor with an 8-mm-long preheating-segment and a 1-mm-long sensing segment. Various fractions of current passing through the preheating-segment from 0% to 54%. As we can see, when 0% current passes through the preheating segment, the sensing segment responses at low flow rate region, and the behavior is very close to the segment #2 in Figure 4.11. As current fraction increases, the response moves towards higher flow rate regions. At a current fraction of 54%, we observe a small peak on the temperature response curve, caused by the large heating power from pre-heating segment. Note that 54% is the highest current fraction we can add to an 8-mm-long preheating segment, beyond which the preheating segment will burn.

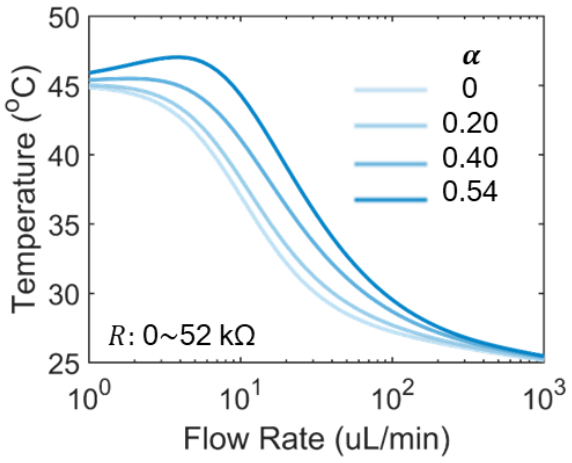

Figure 5.17. Temperature responses of two-segment flow sensors at various fraction of current passing through an 8-mm-long pre-heating segment.

The upper bound of measurement range is determined by the curve with maximum possible current fraction passing through the pre-heating segment, i.e. 54% in Figure 5.17. To reveal the extension of measurement range as a function of preheating length, we plot the temperature responses with maximum possible fraction of current at various preheating length from 0 to 12 mm. As we can see in Figure 5.18, the longer preheating segment we use, the wider measurement range we can achieve. At a preheating length of 12 mm, we achieve a measurement range that extends to 180 μL/min, about the same range as previous 8-segment sensors. To further understand the response of such two-segment sensors, we conduct a first-order heat transfer analysis.

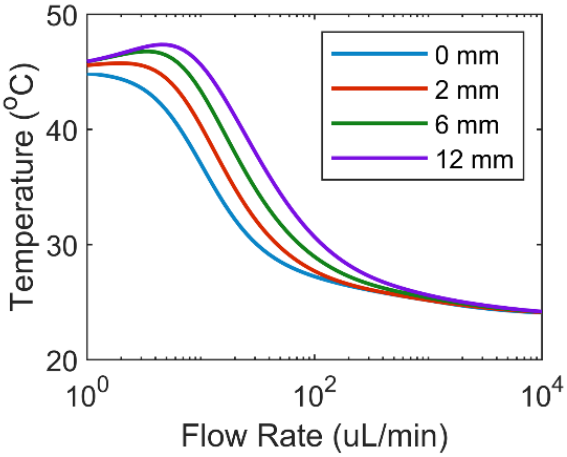

Figure 5.18. Temperature responses of two-segment flow sensors at various preheating segments with maximum possible fraction of current passing though the pre-heating segments.

5.4.2 First-order temperature response theory for a two-segment sensor

A two-segment sensor consists of a long preheating segment (NL) and a short sensing segment (L). Apply the extended analytical model discussed in 5.3.1 to the preheating segment, and we have

$$T_{film}(x) = T_p' - e^{-\frac{q_0}{Q}x} \cdot \left(T_p' - T_{in}\right). \tag{5.17}$$

$$T_{liquid}(x) = T_p' - (1+c)e^{-\frac{q_0}{Q}x} \cdot \left(T_p' - T_{in}\right). \tag{5.18}$$

Thus, we use the analytical model discussed in 4.5.1 to derive the temperature response for the sensing segment of length L:

$$T_{film} = T_s' - \frac{Q/q_0L}{(1+Q/q_0L)} \cdot (T_s' - T_{in}). \tag{5.19}$$

The zero-flow temperature for the preheating segment T_p' and the sensing segment T_s' are associated with the Joule heating I^2R at the segment. Because the current passing through preheating segment is αI, we can relate T_p' and T_s' together by the current fraction α as:

$$q_p = (\alpha I)^2 R = k\left(T_p' - T_{RT}\right) = \alpha^2 k(T_s' - T_{RT}). \tag{5.20}$$

Given that the entrance temperature of liquid equals to room temperature for the pre-heating segment, and $T_{liquid}(NL)$ for the sensing segment, we derive out the temperature response of a two-segment sensor as:

$$T = T' - \frac{Q/q_0L}{(1+Q/q_0L)} \cdot \left(1 - \left(1 - (1+c)e^{-\frac{q_0NL}{Q}}\right) \cdot \alpha^2\right) \ (T' - T_{RT}). \qquad (5.21)$$

Low α limit

At the low limit of α ($R \to 0$), the equation above reduces to

$$T = T' - \frac{Q/q_0L}{(1+Q/q_0L)}(T' - T_{RT}). \qquad (5.22)$$

The temperature response is exactly the same as the response of a single-segment sensor discussed in 4.5.

$\alpha \to 1$ limit

At the limit of $\alpha \to 1$ ($R \to \infty$), the equation above reduces to

$$T = T' - \frac{(1+c)Q/q_0L}{(1+Q/q_0L)}e^{-\frac{q_0NL}{Q}} \ (T' - T_{RT}). \qquad (5.23)$$

Max extension of measurement range

The higher bound of measurement range is defined as the flowrate at which temperature response T equals to $0.5 \cdot (T' + T_{RT})$ at $\alpha \to 1$ limit. By the equation above, we derive out the max extension of measurement range to be:

$$Q_{max} = \frac{q_0}{\ln 2}NL. \qquad (5.24)$$

Similar to multi-segment sensors, the equation above reveals that the extension of measurement range is proportional to the length of preheating element NL.

Match with FEM simulations

We revisit the simulated results in Figure 5.17, and use it for the data fitting with our analytic model. Figure 5.19 shows the simulated responses (dots) and fitted responses (lines) at various current fractions, demonstrating a good match between FEM simulations and analytical model. Table 5.3 lists the fitted values of various device parameters, together with the original values feed into FEM simulations. As we can see, the fitted values for zero flow temperature T' and room temperature T_{RT} are both very close the corresponding values used in FEM simulations. However, N is only a quarter of the set value, indicating a much shorter effective length for preheating segment. Fitted current fraction values are also quite off. To resolve these two issues, we will propose an analytical model for effective length of preheating segment in next section.

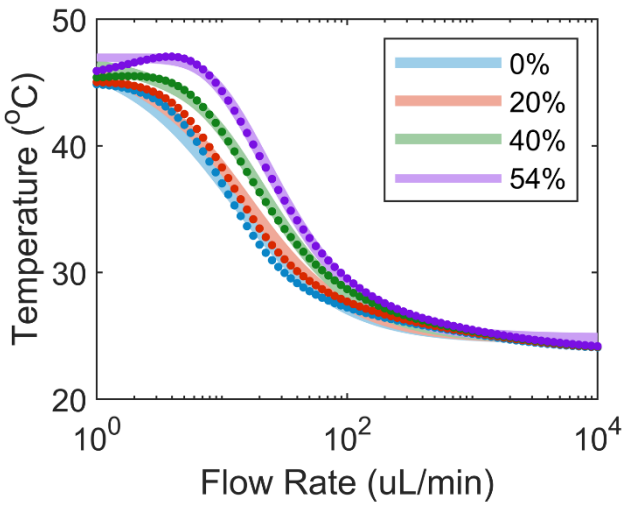

Figure 5.19. Simulated (dots) and fitted (lines) temperature responses of a two-segment sensor.

Table 5.3. Original device parameters in FEM simulations and fitted parameters with analytic model.

	FEM simulations	**Fitted results**
Zero flow temperature T'	45 ºC	47.17 ºC
Room temperature T_{RT}	24 ºC	24.76 ºC
Q_0	--	11.18 μL/min
N	8	1.99
Current fraction $\alpha 1$	0%	22.90%
Current fraction $\alpha 2$	20%	45.90%
Current fraction $\alpha 3$	40%	74.88%
Current fraction $\alpha 4$	54%	97.29%

5.4.3 Effective length of preheating segment

Table 5.3 reveals that the effective length of preheating segment is much shorter than its physical length. One of the possible reason is due to the non-uniform temperature distribution of hot film at zero flow. In this section, we first propose an analytical model to describe this non-uniform distribution, and then verify our first-order model with FEM simulations.

Non-uniform temperature distribution at zero flow

The non-uniform temperature distribution arises from the non-uniform axial heat loss. To describe it with an analytic model, we consider an infinitesimal segment in the middle of preheating segment, as shown in Figure 5.20. The heat generation rate equals $q\delta x$, where q is heat generation rate per unit length, and δx is the length of the segment. Axial heat flux equals the second derivative of temperature $k\frac{\partial^2 T}{\partial x^2}$. Heat dissipation into

surrounding air is proportional to the temperature difference between T and room temperature T_{RT}. Overall, at the equilibrium state, we have:

$$k\frac{\partial^2 T}{\partial x^2} + q - k'(T - T_{RT}) = 0. \tag{5.25}$$

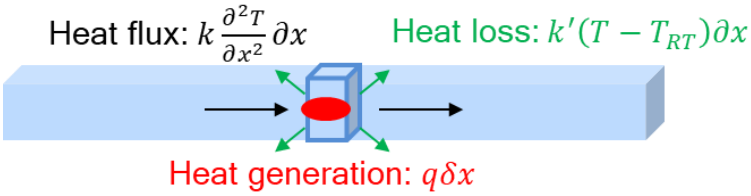

Figure 5.20. Heat generation and dissipation for an infinitesimal segment.

When using Joule heat for the heat generation on CPE, q becomes temperature dependent. With the same assumption made in 4.5.1, we rewrite the equation above as:

$$k\frac{\partial^2 T}{\partial x^2} + \left(q_0 + q'(T - T_{RT})\right) - k'(T - T_{RT}) = 0$$

Or,

$$k\frac{\partial^2 T}{\partial x^2} + q_0 - (k' - q')(T - T_{RT}) = 0. \tag{5.26}$$

To solve the above equation, we rearrange it as follows:

$$\frac{\partial^2}{\partial x^2}\left(T - T_{RT} - \frac{q_0}{k' - q'}\right) = \frac{(k' - q')}{k} \cdot \left(T - T_{RT} - \frac{q_0}{k' - q'}\right). \tag{5.27}$$

The general solution to the equation above is:

$$T - T_{RT} - \frac{q_0}{k' - q'} = c\left(\exp\left(\sqrt{\frac{(k' - q')}{k}}\left(x - \frac{L}{2}\right)\right) + \exp\left(\sqrt{\frac{(k' - q')}{k}}\left(\frac{L}{2} - x\right)\right)\right)$$

The constant c needs to be solved by boundary conditions. As shown in Figure 5.21, axial heat flux comes from one side, and the other side is simplified as $k''(T - T_{RT})$. At equilibrium, we write down the boundary condition as:

$$T(0) = T(L) = T_{RT} + \frac{k}{k''}\left(\frac{\partial T}{\partial x}\right)_{x=0} \tag{5.28}$$

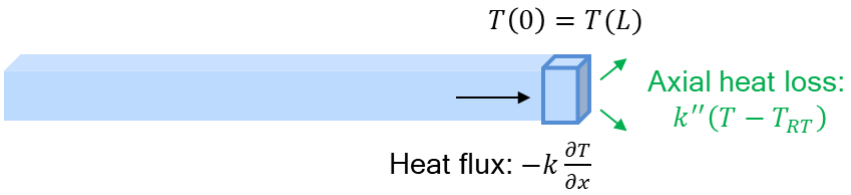

Figure 5.21. Heat generation and dissipation at the boundary.

Substituting the boundary conditions into the general solutions, we arrive the final solution for the temperature distribution at zero flow:

$$T - T_{RT} - \frac{q_0}{k' - q'} = c\left(\exp\left(\sqrt{\frac{(k' - q')}{k}}\left(x - \frac{L}{2}\right)\right) + \exp\left(\sqrt{\frac{(k' - q')}{k}}\left(\frac{L}{2} - x\right)\right)\right), \tag{5.29}$$

where the constant c is defined as:

$$c = \frac{\frac{q_0}{k' - q'}\exp\left(\sqrt{\frac{(k' - q')}{k}}\frac{L}{2}\right)}{\left(\frac{\sqrt{k(k' - q')}}{k''} - 1\right)\left(1 - \exp\left(\sqrt{\frac{(k' - q')}{k}}L\right)\right)}$$

In most cases, we do not need to resolve each parameters in the above equation. Instead, we are more interested in the general shape of the distribution. Thus, we rewrite the above equation as:

$$T = T_0 - c_0\left(\exp\left(c_1\left(x - \frac{L}{2}\right)\right) + \exp\left(c_1\left(\frac{L}{2} - x\right)\right)\right), \tag{5.30}$$

where T_0 is the maximum temperature at the center $x = L/2$, c_0 and c_1 are both geometry-related parameters. Figure 5.22 shows a cutline of temperature distribution at

zero flow calculated from a FEM solver. Obtained temperature distribution is fitted with the equation above, demonstrating a near-perfect match between FEM simulations and analytical model. The fitted curve is describe explicitly as: $y = 45.8 - 0.47\left(e^{0.84(x-4)} + e^{-0.84(x-4)}\right)$.

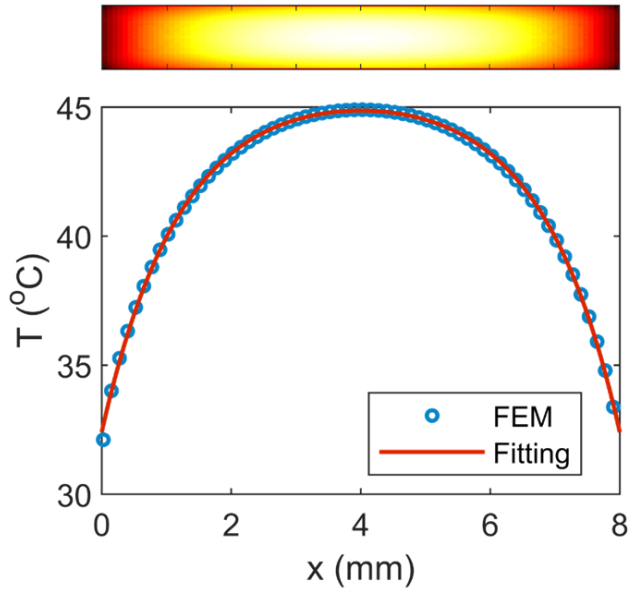

Figure 5.22. (top panel) Temperature distribution on the surface of an 8-mm-long preheating segment at zero flow. (bottom panel) a cutline plot of the 2D temperature distribution with its fitted curve.

Injected power of Joule heating

In an ideal situation where there is no axial heat loss, the preheating segment has a constant temperature of T_0. The injected power of Joule heating equals to:

$$P_{ideal} = I^2 r(T_0) L \tag{5.31}$$

When axial heat loss presents, the temperature distribution is not uniform. Consequently, the overall injected power needs to be integrated from 0 to L:

$$P = \int_0^L I^2 r(T_x) L \mathrm{d}x = I^2 r(T_0) \left(L - \alpha T_0 L + \alpha \int_0^L T \mathrm{d}x \right) \tag{5.32}$$

Substitute the analytical formula for non-linear temperature distribution, and we derive out the integration of T to be:

$$\int_0^L T\mathrm{d}x = T_0 L - \frac{2c_0}{c_1}\left(\exp\left(\frac{c_1 L}{2}\right) - \exp\left(-\frac{c_1 L}{2}\right)\right) \tag{5.33}$$

Combing the two equations above, we arrive at a simpler expression for injected power:

$$P = \int_0^L I^2 r(T_x) L\mathrm{d}x = I^2 r(T_0)\left(L - \frac{2c_0\alpha}{c_1}\left(\exp\left(\frac{c_1 L}{2}\right) - \exp\left(-\frac{c_1 L}{2}\right)\right)\right) \tag{5.34}$$

The equation above reveals a lower heating power than an ideal situation, which translates into a shorter effective length of preheating segment. The effective preheating length when subject to non-uniform axial heat loss is then defined as:

$$L_{eff} = L - \frac{2c_0\alpha}{c_1}\left(\exp\left(\frac{c_1 L}{2}\right) - \exp\left(-\frac{c_1 L}{2}\right)\right) \tag{5.35}$$

Maximum allowed temperature

The extension of measurement range requires the increase of injected Joule heating power. One way to do this is to increase effective length L_{eff}, which needs a lower axial heat loss rate and might be difficult to achieve. Another way is to increase the temperature of hot film, which also increases its resistance. However, the temperature rise of both preheating segment and sensing segment are limited to a certain value, beyond which the system becomes instable and CPE films get burned.

Fiber sensors operate under constant current (cc) mode, which puts the system in a positive feedback loop. Suppose a small temperature rise ΔT is added to the equilibrium state. Hot film temperature will increase by an amount of $\Delta R = \alpha R \Delta T$. At constant current, the Joule heating also increases by $\Delta Q = \alpha I^2 R \Delta T$, which causes the temperature to increase again by another amount of $\Delta T' = (T - T_{RT})\alpha\Delta T$. If $\alpha(T - T_{RT}) < 1,\ \Delta T' < \Delta T$, and the system is stable. If $\alpha(T - T_{RT}) > 1,\ \Delta T' > \Delta T$, and the temperature keeps

increasing until CPE films get burned. Therefore, we derive out a maximum allowed temperature to be:

$$T_{max} = T_{RT} + \frac{1}{\alpha} \tag{5.36}$$

With the equation above, T_{max} is calculated to be 45.16 ^{o}C, and experimentally verified to be 46.5 ^{o}C.

5.4.4 Two-segment sensors with a constant temperature heater

From previous discussions, we found that the upper bound of measurement range is 180 μL/min, about the same as an eight-segment sensor. To further extend measurement range, we can increase the length of preheating segment ($Q_{max} \propto L$). However, this is highly inefficient because measurement range spans across multiple decades, but we cannot increase length across multiple decades easily. An better way to extend measurement range is to increase sensor's effective length N_{eff}. To do this, we could introduce an external heater with constant heating temperature.

Figure 5.23 shows the schematics of a two-segment sensor with a constant temperature heater attached to the first segment. Such a heater can be bulk materials with high thermal conductivity, e.g. metals. Or it can be an array of fibers with active temperature sensing and heating control.

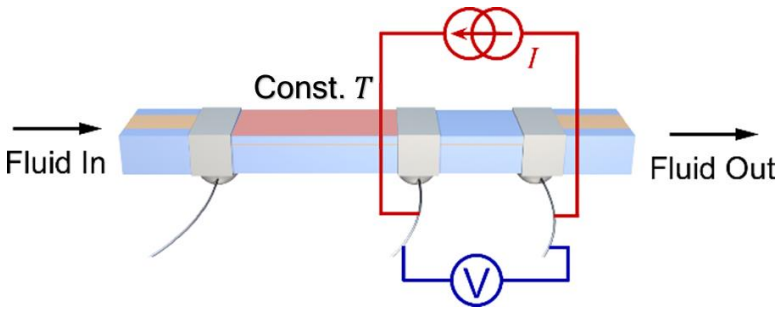

Figure 5.23. Schematics of a two-segment sensor with a constant temperature heater.

Figure 5.24 shows the temperature responses of two-segment sensors with no preheating, with preheating from fiber segment and with preheating from constant temperature heater at 45 ºC. Although the center temperature of fiber preheater is also at 45 ºC, the increase of effective length offers a significant extension of measurement range from 180 to 580 μL/min.

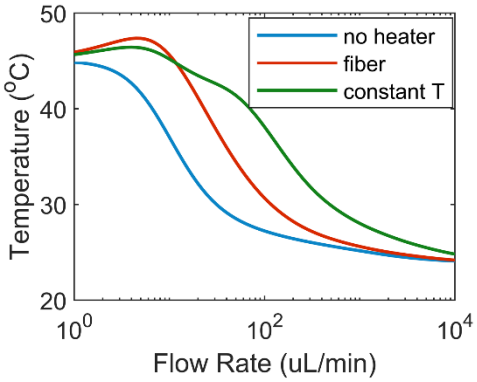

Figure 5.24. Temperature responses of fiber sensors without pre-heater (blue line), with fiber segment as pre-heater (red line), and with constant temperature pre-heater (green line).

In the case of two-segment sensors with constant temperature preheater, the tunability of sensor response is achieved through adjusting the temperature of heater. Since we use an external heating segment instead of CPE hot films, the max heating temperature is not limited by 45 ºC anymore. Moreover, we can even apply a cooler for liquid pre-cooling. Figure 5.25 shows the temperature responses of fiber sensors with constant temperature preheater at various temperatures. Altogether, a great extension of measurement range is achieved with constant temperature heater. Table 5.4 lists the measurement ranges of fiber sensors with constant temperature pre-heater at various temperatures from 0 to 60 ºC. As we can see, the upper bound of measurement range reaches 1412.5 μL/min with the heater temperature at 60 ºC, and the lower bound is as low

as 1.6 μL/min with the heater temperature at 0 ºC. Overall, we achieved a measurement range across three decades with only 2 surface contacts necessary.

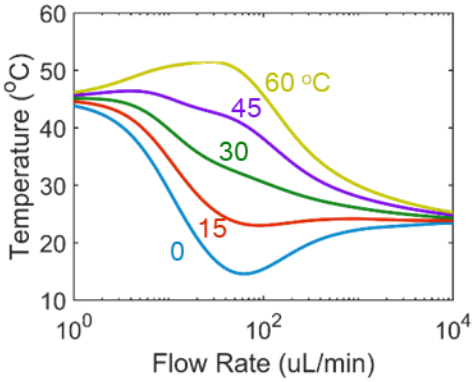

Figure 5.25. Temperature responses of fiber sensors with constant temperature pre-heater at various temperatures from 0 to 60 ºC.

Table 5.4. Measurement ranges of fiber sensors with constant temperature pre-heater at various temperatures from 0 to 60 ºC.

Preheater temperature (ºC)	**Measurement range (μL/min)**
0	1.6 ~ 44.7
15	2.5 ~ 44.7
30	4.0 ~ 125.9
45	10.0 ~ 631.0
60	44.7 ~ 1412.5

5.5 Unification of Two Temperature Distribution Theories

So far, we have developed two analytical models to describe the temperature distribution of CPE films. One aims to solve the temperature distribution of a single-segment sensor that is too long to be approximated as a constant. Another one aims to calculate the temperature distribution of a preheating segment at zero flow rate. Table 5.5

and Table 5.6 lists basic descriptions of these two models. As we can see, the main difference of them is that one only considers cross sectional heat loss; whereas the other one only considers axial heat loss. In this section, we will develop a new model that unifies both of those two model.

Table 5.5. Description of temperature distribution model for a long single-segment sensor.

	Temperature distribution for a long single-segment sensor
Typical distribution	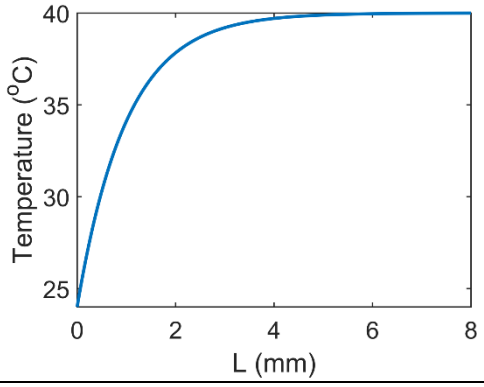
Physics	Heat generation equals cross sectional heat loss.
Solver	One-way Coupling
PDE	$q_0 - (k - q')(T - T_{RT}) = k"(T - T2)$ $k'''(T - T2) = Q\frac{\partial T2}{\partial x}$
Solution	$T = T_p' - e^{-\frac{q_0}{Q}x} \cdot (T_p' - T_{in})$

Table 5.6. Description of temperature distribution model for a preheating segment.

	Temperature distribution for a preheating segment
Typical distribution	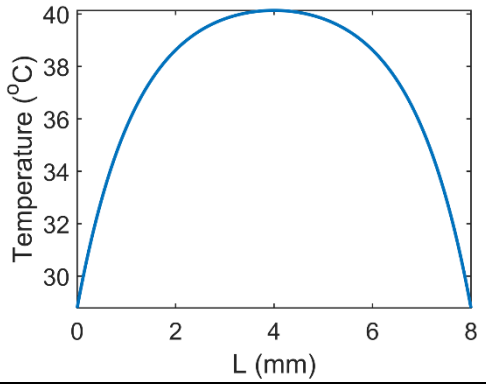
Physics	Heat generation equals axial heat loss.
Solver	Two-way Coupling
PDE	$k\frac{\partial^2 T}{\partial x^2} + q_0 - (k' - q')(T - T_{RT}) = 0$
Solution	$T = T_0 + c_0\left(\exp\left(c_1\left(x - \frac{L}{2}\right)\right) - \exp\left(c_1\left(\frac{L}{2} - x\right)\right)\right)$

Now consider a differential segment that is subject to both axial heat loss and cross sectional heat loss. We can express the equilibrium state as:

$$k\frac{\partial^2 T}{\partial x^2} + q_0 - (k' - q')(T - T_{RT}) = k"(T - T2)$$
$$k'''(T - T2) = Q\frac{\partial T2}{\partial x} \tag{5.37}$$

where T and $T2$ are hot film temperature and liquid temperature, respectively. All rest parameters follow the same symbol as we used in 5.4.3. Take the derivative of the first equation above with respect to x, and we arrive at:

$$k\frac{\partial^3 T}{\partial x^3} - (k' - q')\frac{\partial T}{\partial x} = k"\frac{\partial T}{\partial x} - k"\frac{\partial T2}{\partial x}$$

Subsitituting the expresion for $\partial T2/\partial x$, the equation above becomes:

$$k\frac{\partial^3 T}{\partial x^3} - (k' + k'' - q')\frac{\partial T}{\partial x} = -\frac{k'''}{Q}k''(T - T2) \tag{5.38}$$

Combine the two equations above and eliminate the term of $k''(T - T2)$. We have:

$$k\frac{\partial^3 T}{\partial x^3} - (k' + k'' - q')\frac{\partial T}{\partial x} = -\frac{k'''}{Q}k\frac{\partial^2 T}{\partial x^2} - \frac{k'''}{Q}q_0 + \frac{k'''}{Q}(k' - q')(T - T_{RT}) \quad (5.39)$$

Rearrange the equation above, and we arrive at the final partial differential equation:

$$k\frac{\partial^3 T}{\partial x^3} + \frac{kk'''}{Q}\frac{\partial^2 T}{\partial x^2} - (k' + k'' - q')\frac{\partial T}{\partial x} - \frac{k'''}{Q}(k' - q')T + \frac{k'''}{Q}\left((k' - q')T_{RT} + q_0\right) = 0 (5.40)$$

Low Q limit

At the limit of low flow rate ($Q \to 0$), the equation above is simplified to

$$k\frac{\partial^2 T}{\partial x^2} - (k' - q')T + (k' - q')T_{RT} + q_0 = 0 \quad (5.41)$$

This equation is the same as the PDE in Table 5.6, indicating that cross-sectional heat loss is negligible at low flow rate.

High Q limit

At the limit of high flow rate ($Q \to \infty$), the equation above reduces to

$$k\frac{\partial^3 T}{\partial x^3} - (k' + k'' - q')\frac{\partial T}{\partial x} = 0 \quad (5.42)$$

The temperature distribution becomes constant T_{in}, which agrees with the solution in Table 5.5.

General cases

In all other cases, the temperature distribution needs to be solved from Eq. 5.40. To solve it, we first need to find all roots for equation as follows:

$$kt^3 + \frac{kk'''}{Q}t^2 - \left(k' + k'' - q'\right)t - \frac{k'''}{Q}\left(k' - q'\right) = 0 \quad (5.43)$$

Suppose the roots are t_1, t_2 and t_3. Then the general solution of temperature distribution becomes:

$$T(x) = c_1 e^{t_1 x} + c_2 e^{t_2 x} + c_3 e^{t_3 x} + T_{RT} + \frac{q_0}{k' - q'}, \quad (5.44)$$

where c_1, c_2, and c_3 are all constants determined by boundary conditions.

To summarize this chapter, we have theoretically optimized the geometry of single-segment sensors, with over 20% improvements on sensitivity over original geometries. Novel structures of a preheating segment and a sensing segment significantly reduces the complexity of post-drawing fabrication, without sacrificing measurement range. Furthermore, we propose that by introducing an external heater with constant temperature, the measurement range extends more than 10 times. More importantly, we conducted two temperature distribution analyses to understand the evolution of hot film temperature along the segment, and unified them together as well. This offers us great knowledge to develop distributed sensors in next chapter.

Chapter 6: Distributed Fiber Sensors

In this chapter, we investigate a general strategy to achieve distributed sensing with electronic sensors. The general strategy applies to many sensing modalities, such as temperature sensors, acoustic sensors, flex sensors and flow sensors. We develop a first-order current flow model to estimate the spatial resolutions for such distributed sensors, and point out the direction for future optimization based on our model. Then we focus on flow sensors for the demonstration of distributed sensing. A complete demonstration of distributed flow sensors is provided with FEM simulations.

6.1 Motivation of Distributed Sensors

6.1.1 Limitations of Optical Distributed Sensors

Distributed sensing refers to a sensing technology with continuous measurements along the entire length of a fiber. [61]–[64] Its popularity in oil and gas industry arises from its high spatial and temporal profiling over long lengths, large areas, as well as locations where conventional point sensing cannot reach. Distributed optical fiber sensors (DOFS) are the most popular distributed fiber sensors and have been widely used in civil engineering. DOFS utilize light scattering, for example Raman and Brillouin scattering, to acquire information about the fiber properties, and subsequent environmental parameters [61]. Both Raman and Brillouin scattering are highly dependent on propagation medium temperature and strain. Hence, two main applications of DOFS are distributed temperature sensors or distributed strain sensors.

Typical DOFS suffer from the low spatial resolution, i.e. tens of centimeter to meter. For example, the spatial resolution ΔZ_{min} for a time-domain reflectometry (OTDR) based DOFS is dependent on the pulse width τ and the refractive index of the fiber n:

$$\Delta Z_{min} = \frac{c\tau}{2n}. \quad (6.1)$$

For a typical pulse width of 10 ns and refractive index of 1.5, Equation 5.1 gives a spatial resolution of ~1 m. Many research groups have proposed various techniques to improve the spatial resolution to tens of cm level [62], [65]. However, those techniques inevitably bring out many other problems, such as expensive laser system, low measurement range in length or low measurement precision in temperature/strain. And none of those techniques can bring down the spatial resolution to sub-cm level. Other than low spatial resolution, it is rather difficult to integrate high-precision laser system into low-cost wearable electronics.

6.1.2 Previous work on electrical fiber sensing Over Large Area

Multipoint Surface Contact

Fibers are inherently uniform along its axial direction, thus fundamentally difficult to resolve the location information along the fibers. Researchers have proposed various methods to detect the signal strength together with location information using electrical fibers. Sorin *et. al.* proposed a photo detecting fiber that resolves optical illumination distributions by scanning the potential profile along the fiber. When an optical signal is impingent on the fiber, the local resistivity will change, which alters the surrounding potential distribution. Thus, the signal strength and location information can both be acquired through measuring the potential at various locations along the fibers.

However, this method requires multiple surface contacts constructed along the entire fiber. The density of surface contacts directly determines the spatial resolution. For a signal that impinges between two adjacent contacts, this method cannot resolve its location information. What is worse, this method also requires the establishment of electrical connection to all contacts along the fiber, which needs to be built after thermal

drawing. As a consequent, it is rather difficult to use it cover large area or long distance. Overall, this technique does not achieve distributed sensing since it cannot resolve information continuously with signal received at the end of the fiber.

2N Sensor Grid

Another popular way to resolve location information is to form a sensor grid with 2N fibers. Bayindir *et. al.* reported such a sensor grid of N horizontal fibers resolving x coordinate and N vertical fibers detecting y coordinate [12]. Thus, a sensor grid of 2N fibers is able to detect the location (x, y) as well as the strength of a signal (touch point and finger temperature).

However, this method is limited to one signal input at a time. When signals come to multiple points at the same time, this sensor grid cannot resolve any of them. For example, two signals of strength A_1 and A_2 arrive at two different points $(x_1,\ y_1)$ and $(x_2,\ y_2)$. On the fibers' side, two horizontal fibers (corresponding to x_1 and x_2) and two vertical fibers (corresponding to y_1 and y_2) detect the signal simultaneously. The sensor grid cannot tell if the signals locate at $(x_1,\ y_1)$ & $(x_2,\ y_2)$ or at $(x_1,\ y_2)$ & $(x_2,\ y_1)$. Thus, the applications of this sensor grid is strongly limited to the assumption that only one signal source exists at a time, which is not practical for many real-world applications such as thermal mapping or remote sensing.

Overall, these substantial limitations with current optical distributed sensors limit their applications in wearable devices or microfluidics systems, which requires easy setup, portable distributed sensing techniques. Meanwhile, electrical fibers are not capable to achieve distributed sensing, or sensing over a long distance or large area. Thus, it important to explore new structures for electrically active distributed sensing.

6.2 MECHANISMS OF FIBER DISTRIBUTED SENSORS

6.2.1 Fundamental requirements of distributed sensing

Although intensive research work has been done to enable electrical fibers with distributed sensing, none of them really achieves it. Essentially, a truly distributed fiber sensor should satisfy two fundamental requirements as follows:

- Breaking of axial uniformity;
- Ability to record a signal of two degrees of freedom at the near or far end;

Thermal drawn fibers are inherently uniform along the axial direction, thus cannot resolve impingement locations of incoming signals. Optical distributed fibers either utilize a Bragg gratings integrated on a short segment within the fibers [66], or employ optical time (or frequency) domain reflectometry measurement principles [61], [63] to break axial uniformity. As to electrically active fibers, current method to break axial uniformity is to construct multiple surface contacts along the fiber (as we mentioned in 4.7 and 6.1.2). This process requires post-drawing fabrication, and can be extremely tedious when dealing with a long segment.

Other than the breaking of axial uniformity, fiber distributed sensors also requires the ability to record a signal of at least two degrees of freedom at the near/far end. This is because the location and the strength of incoming signals are completely independent variables. Thus, at least two degrees of freedom is required to describe incoming signals. Optical distributed fibers record both the strength and the time duration (or frequency) of backscattered light. However, it is quite difficult for electrical fibers to record signals with two degrees of freedom. Consequently, previous work relies on N signals with one degree to freedom to interpolate 2D distribution, which is done through N surface contacts or 2N independent fiber sensors (see 6.1.2 for details).

Taken as a whole, to achieve truly distributed sensing in fiber sensors, we need to come up with completely novel device structures, which not only break the axial symmetry, but also allow to record signals of at least two degrees of freedom.

6.2.2 Microfluidics-enabled fiber distributed sensors

We address those challenges by introducing a microfluidics droplet to locally activate fiber sensors, hence breaking the axial uniformity. The droplet slides along the entire fiber for sensing at various locations. Recorded signals have two degrees of freedom: amplitude and time. Therefore, microfluidics-enabled fiber distributed sensors resolve both of those two fundamental requirements mentioned earlier.

Specially, our proposed fiber distributed sensors consist of three components:

1. Two metal strips that offer ultra-high axial conductivity;
2. Conductive polymeric films that offer low cross-sectional conductivity;
3. A microfluidics droplet that forms a closed-loop path for current flow;

Figure 6.1 shows the schematics of a general fiber distributed-sensor. The top plate and the bottom plate are electrically connected through the droplet in the fluidic channel. Due to the significant contrast of conductivity between metal (~10^7 S·m) and conductive polymeric films, i.e. CPE (~2 S·m), metal strips are treated as equipotential objects. The crosswise resistance of CPE films dominates the overall resistance from terminal A to B, and current flows through CPE films locally around the droplet. By moving the droplet along the entire fiber, we obtain the distribution of CPE resistance along the fiber, which is highly sensitive to many environment parameters, such as temperature, flowrate, strain, or acoustic pressure.

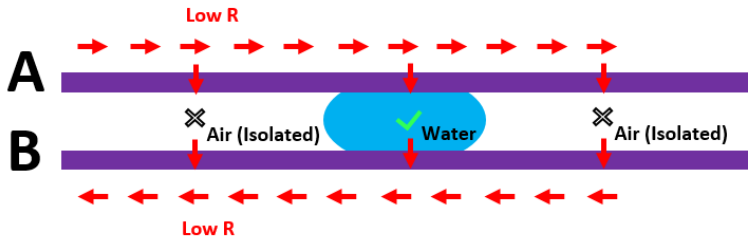

Figure 6.1. Schematics of a general fiber distributed sensor.

6.2.3 Potential fiber distributed sensors and their applications

With the knowledge we have known, as well as the materials available, we proposed the following fiber distributed sensors possible with the general strategy mentioned above:

1. Distributed thermal/temperature sensors;
2. Distributed flexion/bend sensors;
3. Distributed flowrate sensors;
4. Distributed acoustic sensors;

In this section, we focus on the first two distributed sensors and discuss their potential applications. Distributed temperature sensors utilize the high temperature coefficients of resistance (TCR) of CPE films (see 2.4.3). One of the potential application for distributed temperature sensors could be intelligent cloth to protect firefighters. Firefighters start experiencing discomfort or pain when skin temperature reaches 44 ^{o}C, and would suffer first-degree burn at only 4 degrees above this value. At 11 degrees above this value, it becomes second-degree burn and more serious burn[47]. The minor temperature difference between discomfort and burn injures makes it extremely important to put temperature sensors on firefighters' clothes. Using fiber distributed-sensors for intelligent cloth can closely map the temperature distribution over the whole surface with only one or

a few sensor units. Moreover, the high temperature spot is detected together with its location, which could be crucial to protect firefighters in time.

Distributed flex sensors, on the other hand, take the advantage of the stress dependent resistance of CPE films. One main application for distributed flex sensors could be wearable devices as video game touchless controller or robotic control. Current widely used flex sensors only extract the overall bending status, hence cannot resolve complex shapes or gestures. Distributed flex sensors, however, can reconstruct the local curvature information along the entire fibers, regardless of the overall complexity. Thus, it could significantly improve the performance of current wearable touchless controller.

In later sections of this chapter, we demonstrate the concept of distributed sensors for flow monitoring. Among the four potential sensors mentioned here, we choose distributed flow sensors for demonstration not only because we have accumulated enough knowledge about fiber flow sensors from previous chapters, but also because distributed flow sensing is the most complicated one among the four, which involves many physics being coupled together.

6.3 Electrical Current Profile of Distributed Flow Sensors

In this section, we investigate the electrical current profile of distributed flow sensors. We first analyze the lumped-element circuit model to valid previous assumption that crosswise CPE resistance dominates the overall resistance between two terminals at the near end of the fibers. Then we develop a first-order current distribution model to estimate the spatial resolution of fiber distributed sensors, which also poses the direction for future optimization.

6.3.1 Lumped-element circuit model

The basic structure of a distributed flow sensor (as shown in Figure 6.2) follows a similar design strategy as regular fiber flow sensors. The inner channel consists of a droplet that slides along the entire fiber to locally heat up the hot film CPE, and hence resolves the local flow rate outside of the fiber. Comparing to the structure of regular fiber flow sensors, we removed the dielectric layers adjacent to the inner channel to allow current flow into the droplet. On the outer surfaces, we add extra dielectric layers to protect CPE films from shorted by streaming fluid. The CPE films are cut open to force electrical current flows through a longer distance before flows into the droplet.

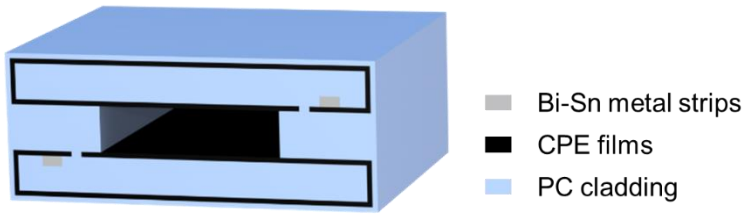

Figure 6.2. Schematics of cross sectional geometry for fiber distributed sensors.

With the device structures ready, we conduct a circuit model analysis of fiber distributed sensors. Figure 6.3 shows the lumped-element circuit model for fiber distributed sensors. Here r_1 represents the distributed resistance of Bi-Sn metal strips, estimated to be 10 Ω/m. R_2 indicates the crosswise resistance of CPE films, estimated to be 10 kΩ. And R_3 arises from the resistance of the sliding droplet, estimated to be 10 Ω. The overall resistance between two terminals on the left end equals:

$$R_T = 2r_1 \cdot x + 2R_2 + R_3, \tag{6.2}$$

where x is the distance from the droplet to current injection point.

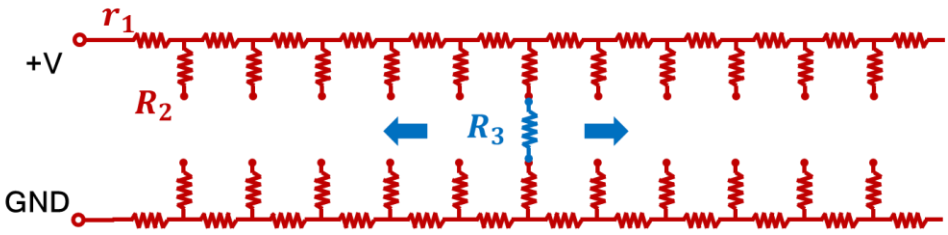

Figure 6.3. Lumped-element circuit model for fiber distributed sensors

Substitute the resistance of CPE measured in 2.3.1, we rewrite the equation above as:

$$R_T = \left(\frac{2x}{\text{cm}} + 10\right)\ \Omega + \left(0.87 \cdot e^{0.091(T-25)} + 9.1\right)\ \text{k}\Omega. \tag{6.3}$$

This equation reveals that the overall resistance only varies by less than 1% for a 50-cm-long sensor segment at constant temperature. Thus, local resistance of CPE films dominate the overall resistance.

6.3.2 First-order current distribution theory

The spatial resolution of a distributed flow sensor deeply inherits from the spread of its current distribution, which cannot be explained by previous lumped-element circuit model. Thus, we developed a first-order current distribution theory to estimate the spatial resolution.

Figure 6.4 shows the illustration for this first-order current flow model. From the cross section of fiber distributed sensors (Figure 6.4a), we first extract the structures involve current flow, i.e. metal, CPE, and droplet (Figure 6.4b). Due to the symmetry between top place and bottom plate, we only keep half of the structures (Figure 6.4c). Unfolding CPE films, we arrive at a large CPE plane with metal electrode on the left end and droplet on the right end. In first-order approximation, we treat the metal electrode and

droplet both as equal potential regions. Therefore, the current distribution can be solved within the 2D plane of CPE films.

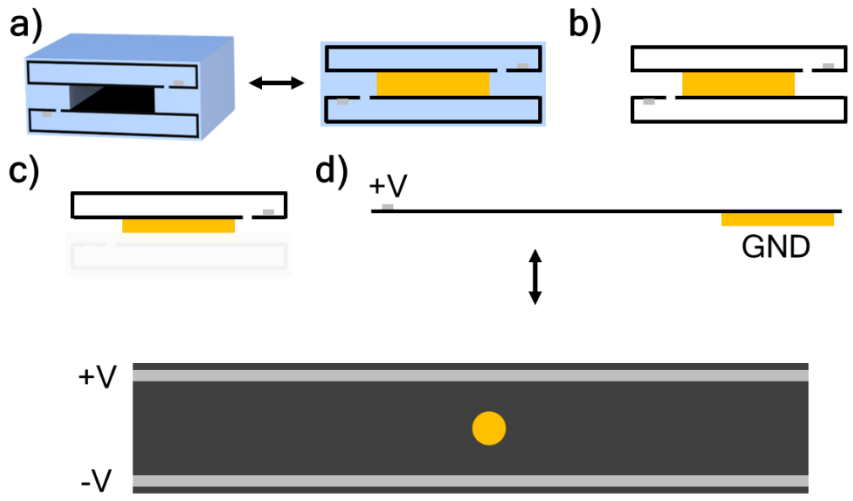

Figure 6.4. Illustrations for first-model current flow model.

We apply the method of image current sources to solve the 2D current distribution in a system described in Figure 6.4d. This method creates a series of image current sources to analog the effect of metal electrodes. As we can see in Figure 6.5, each current source is adjacent to two other sources of the same amplitude but opposite sign at a distance of $2d$, where d is the distance between original current source to either metal electrode. In first-order approximation, we treat the droplet as a point current source, thus the current distribution of a source I located at (x_0, y_0) equals

$$j(x,y) = \frac{I}{2\pi} \cdot \frac{1}{\sqrt{(x-x_0)^2 + (y-y_0)^2}}. \quad (6.4)$$

It is quite trivial to conclude that current spreads out the most at the middle between two opposite current sources, e.g. $y = 0$, where metal strips locate. Thus, we only consider the projection of current distribution on y axis at $y = 0$.

$$j(x,0) = \frac{I}{2\pi} \cdot \frac{1}{\sqrt{(x-x_0)^2 + (y-y_0)^2}} \cdot \frac{y_0}{\sqrt{(x-x_0)^2 + (y-y_0)^2}}.$$

Or,

$$j(x,0) = \frac{I}{2\pi} \cdot \frac{y_0}{(x-x_0)^2 + (y-y_0)^2}. \tag{6.5}$$

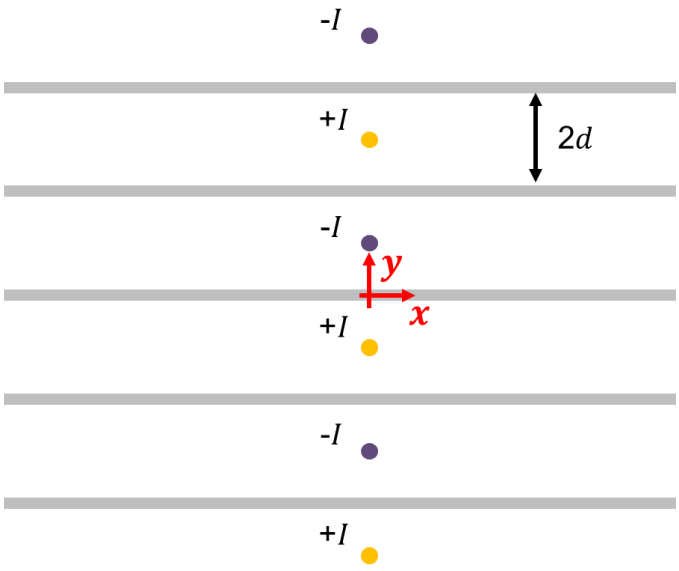

Figure 6.5. Diagram for the method of image current sources.

With the equation above, we sum up the current distribution from all image sources. The overall current distribution becomes:

$$j = -\frac{I}{\pi}\left(\frac{d}{x^2+d^2} - \frac{3d}{x^2+9d^2} + \frac{5d}{x^2+25d^2} - \cdots\right) = \frac{I}{\pi}\sum_{n=1}^{\infty}\left(\frac{(-1)^n(2n-1)d}{x^2+\left((2n-1)d\right)^2}\right) \tag{6.6}$$

The sum of this series converges to:

$$j = \frac{I}{2d}\left(\frac{1}{\cosh\left(\frac{\pi}{2d}x\right)}\right), \tag{6.7}$$

which becomes the final current distribution model for distributed fiber sensors.

Current distribution at an arbitrary point

Without delving too deep into math derivation, here we only briefly describe our strategy to calculate the distribution at an arbitrary point. We first translate the current distribution problem to a potential distribution problem, which requires solving the Laplace equation with boundary conditions defined at two metal lines. We then separate the two variables x and y in this Laplace equation, which can be solved with Green's function. Finally, we derive out the potential distribution described as:

$$\phi - \phi_0 = \frac{I\rho}{\pi} \ln \frac{\left(\cosh\left(\frac{\pi}{2d}x\right) - 0.5\cos\frac{\pi}{2d}(y-d)\right)}{\left(\cosh\left(\frac{\pi}{2d}x\right) - 0.5\cos\frac{\pi}{2d}(y+d)\right)} \tag{6.8}$$

From this point, we can calculate the current distribution at an arbitrary point:

$$j_x = \frac{1}{\rho}\frac{d\phi}{dx} = \frac{I}{2d}\left(\frac{\sinh\left(\frac{\pi}{2d}x\right)}{\left(\cosh\left(\frac{\pi}{2d}x\right) - 0.5\cos\frac{\pi}{2d}(y-d)\right)} - \frac{\sinh\left(\frac{\pi}{2d}x\right)}{\cosh\left(\frac{\pi}{2d}x\right) - 0.5\cos\frac{\pi}{2d}(y+d)}\right)$$

$$j_y = \frac{1}{\rho}\frac{d\phi}{dy} = \frac{I}{2d}\left(\frac{\sin\left(\frac{\pi}{2d}(y-d)\right)}{\cosh\left(\frac{\pi}{2d}x\right) - 0.5\cos\frac{\pi}{2d}(y-d)} - \frac{\sin\left(\frac{\pi}{2d}(y+d)\right)}{\cosh\left(\frac{\pi}{2d}x\right) - 0.5\cos\frac{\pi}{2d}(y+d)}\right)$$

6.3.3 Current distribution claculated from FEM

To validate our first-order current distribution theory, we simulate the current distribution of distributed fiber flow sensors with a FEM solver. Figure 6.6 shows the reuslts on CPE films with droplets located at four different locations (bottom blue squares). Metal trips locate at the top of each subplots. Color varies from yellow to blue indicating the amplitude of the current. Red arrows show the direction of current flow. As we move the droplet from right to left, it also focuses the current distribution around it. As a result, only local CPE films have current flowing through.

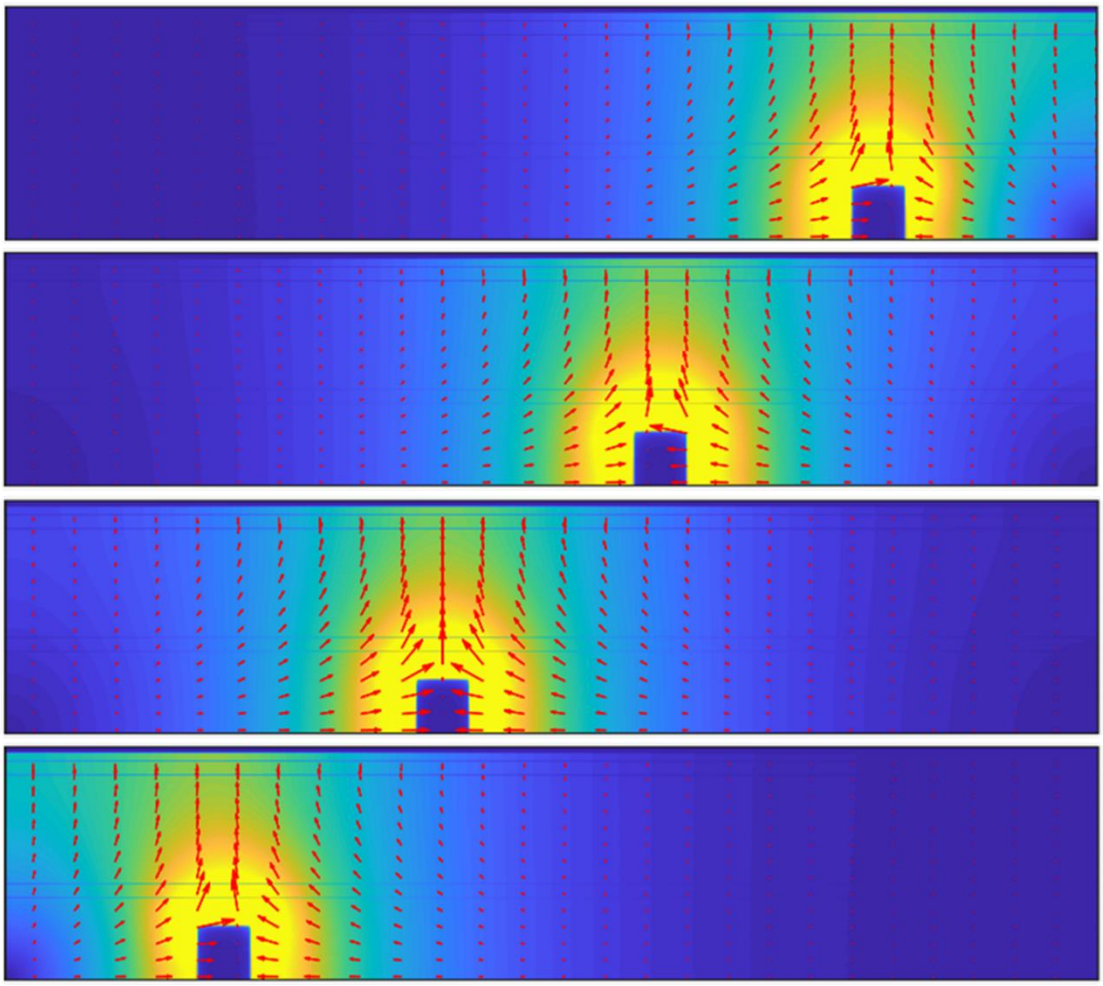

Figure 6.6. Current disstributions of distributed fiber flow sensors.

We extract the current distribution at the interface between CPE films and metal strip, and fit simulated results with analytical model we discussed in 6.3.2. Figure 6.7 shows the results with droplet located at two different locations (blue and red). As we can see, fitting curves match FEM simulations very well between 5 cm to 15 cm. Beyond this region, fittng curves are a little off from FEM results becuase it is too close to the edges (0 cm and 20 cm) of FEM simulated domain.

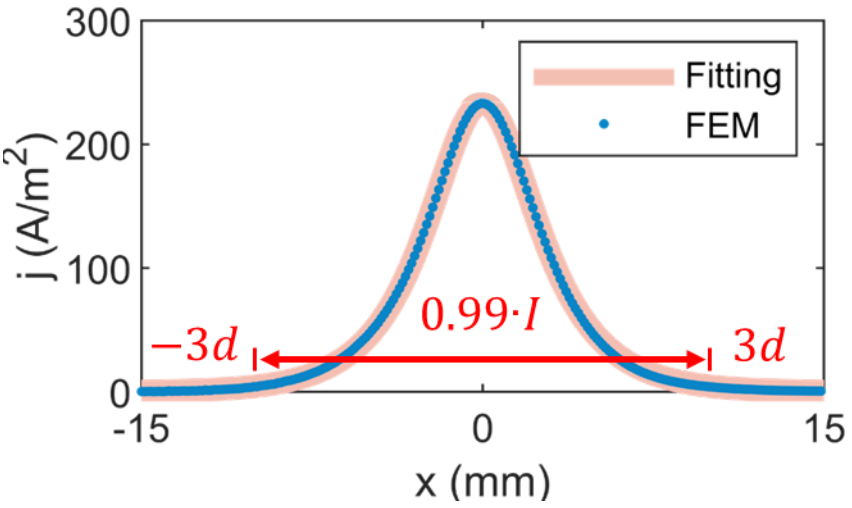

Figure 6.7. Simulated (dots) and fitted (lines) current disstribution at CPE/metal interface.

6.3.4 Spatial resolution of fiber distributed sensors

The Joule heating is proportional to the square of current distribution. As a result, Joule heating mainly happens at the region with large current flow. On the other hand, the voltage responses of fiber distributed sensors are directly related to current flow. Thus, we define the spatial resolution as the region that includes 99% current contributions. To solve this region, we calculate the integration of the equation above from $-w$ to w:

$$I_{active} = \int_{-w}^{w} \frac{I}{2d}\left(\frac{1}{\cosh\left(\frac{\pi}{2d}x\right)}\right)\mathrm{d}x = \frac{2I}{\pi}\arctan(e^{\frac{\pi}{2d}w} - e^{-\frac{\pi}{2d}w}). \qquad (6.9)$$

With this equation, we can conclude that:

- Region from -∞ to ∞, $I_{active} = I$;
- Region from $-3d$ to $3d$, $I_{active} = 0.989 \cdot I$;
- Region from$-2d$ to $2d$, $I_{active} = 0.945 \cdot I$;
- Region from$-d$ to d, $I_{active} = 0.739 \cdot I$;

Thus, we estimate the spatial resolution to be 3*d*, which equals to 8 mm, from first-order current distribution theory. To get a more accurate result, we set the temperature of CPE films as a step function from T_0 to T_1 (see Figure 6.8). Then the droplet slides inside of fluidic channel and senses the temperature distribution.

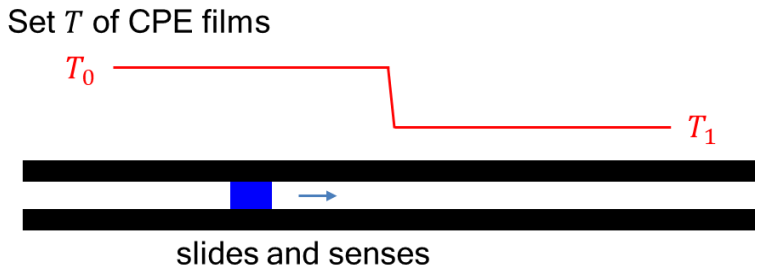

Figure 6.8. Simulation setup for step response of fiber distributed sensors.

Figure 6.9 shows the simulated step responses of fiber distributed sensors with a sudden change of 10 degree happens at 0 mm. At 5 mm away, the measured temperature is less than 0.5% different from set temperature of CPE films. At 8 mm away, the difference drops to ~0.05%. In other words, FEM results reveal a much finer spatial resolution than first-order theory. The difference comes from the overestimate of current spread in first-order theory, where we only consider the maximum current spread at metal/CPE interface.

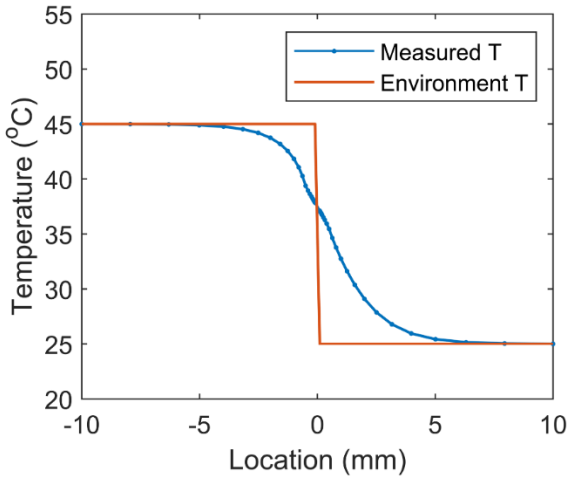

Figure 6.9. Step response of fiber distributed sensors.

So far, we have analyzed the electrical behaviors of fiber distributed sensors. We verify that such distributed sensors satisfy both of the two fundamental requirements in 6.2.1. Moreover, we developed a first-order current flow theory to describe the current spread on CPE films, from where we estimate the spatial resolution to be 8 mm. Later FEM simulations also corroborate a sub-cm spatial resolution. With those knowledge ready, we will start demonstrating distributed fiber sensors in next section.

6.4 Demonstration of Distributed Fiber Flow Sensors in Simulations

In this section, we demonstrate the concept of distributed flow sensors with FEM simulations. The demonstration consists of three steps: first we show the temperature and voltage responses of distributed flow sensors to flow rate; next we provide the temperature and voltage responses with the droplet located at various locations; last we conduct a scan of fully developed laminar flow profile and reconstruct the flow velocity profile with recorded data.

6.4.1 Simulation Setup

A 3D first-principle finite-element-method (FEM) analysis [60] is conducted to demonstrate the concept of distributed flow sensors. The complete model involves the coupling of at least three physics modules:

- electric currents module for current flow in metal strips and droplet;
- electric currents, shell module for current flow on CPE films;
- conjugate heat transfer module for heat transfer in solids and fluids;
- laminar flow module is optional for the establishment of a flow profile; (it is necessary when only a portion of laminar flow profile is needed in conjugate heat transfer module)
- moving mesh module is optional for the movement of the droplet; (it is necessary when we are interested in time-dependent solution)

The geometry setup of simulated structure is shown in Figure 6.10. Note that only half of the structure is simulated due to the xy-plane symmetry. For preliminary demonstration, we only simulate a device of 60-mm-long, and the streaming liquid passes through a rectangular tank sits on the top of the device. The side surfaces are subject to free convection to air, which follows $Q = h \cdot (T_{solid} - T_{RT})$. T_{solid} is the temperature of solids at the interface, and T_{RT} is room temperature at 24 ^{o}C. We use the same values for heat transfer rate *h* as previous simulations in 4.6.1: 125 W/(K·m2). The droplet is simply treated as a rectangular bar of 1-mm-long and fills the entire fluidic channel. Note that we have shown that 1.9-cm-long segment is sufficient to cover active fiber region for thermal analysis, and we will also show that 6-cm-long segment is sufficient for electrical analysis.

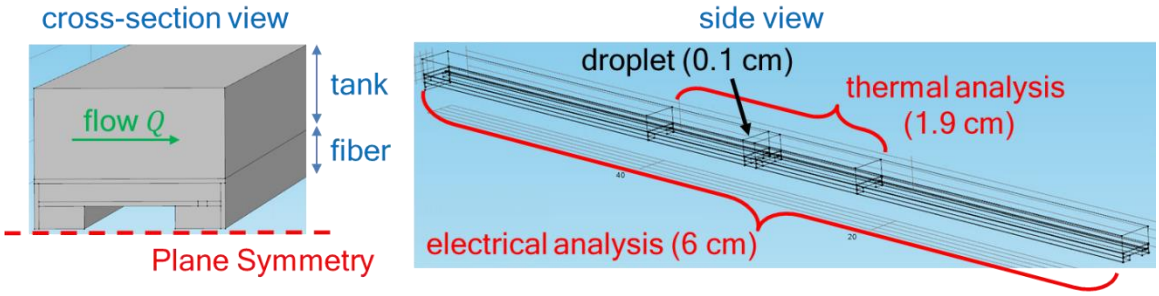

Figure 6.10. Geometry setup for the demonstration of fiber distributed sensors.

6.4.2 Responses of distributed sensors to flow rate

We first calculate the temperature and voltage responses with the droplet locates at the center (y = 10 mm), as shown in Figure 6.11. Notice that the x-axis is now flow velocity (m/s) instead of flow rate (μL/min), since the device senses the out-of-channel flow and volumetric flow rate is not clear in this case. Three flow regimes are clearly seen in Figure 6.11: a dead regime below 0.02 mm/s, a sensitive regime between 0.1 to 10 mm/s and a saturation regime beyond 10 mm/s. The average sensitivity within sensitive regime is calculated to be 0.82 ^{o}C/(mm/s), which translates to a voltage sensitivity of 0.27 V/(mm/s). In other words, fiber distributed flow sensors behavior similar to single-point fiber flow sensors in Chapter 3. Overall, the temperature and voltage responses have demonstrated that fiber distributed sensors are sensitive out-of-channel streaming fluid. In next section, we will demonstrate that this response is insensitive to the location of droplet.

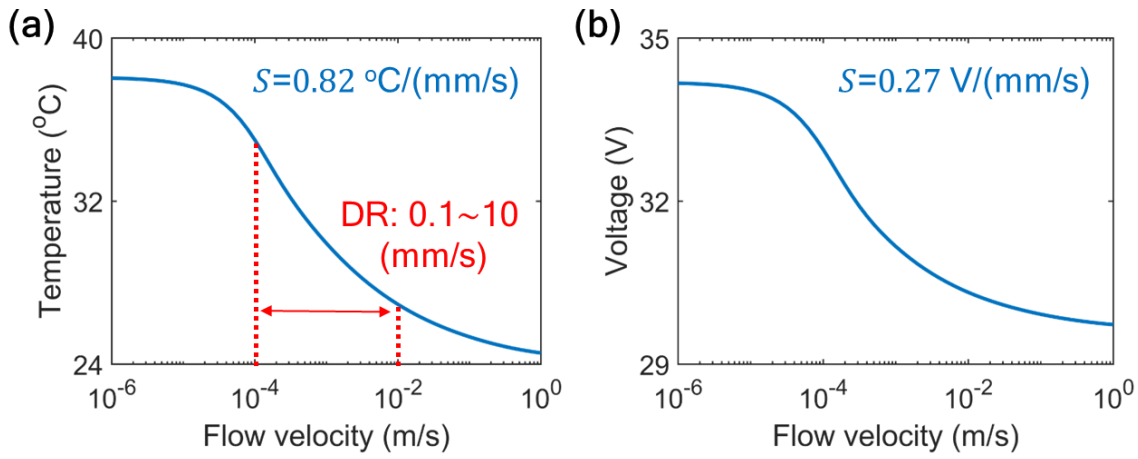

Figure 6.11. Temperature (a) and voltage (b) responses of fiber distributed sensors.

6.4.3 Responses of distributed sensors to droplet locations

We picked up three specific flow velocities from Figure 6.11: 0.1, 1 and 200 mm/s, which correspond to three film temperatures of 35, 30 and 25 °C, respectively. Then we simulate the temperature and voltage responses to droplet locations, subject to those three flow velocities. In an ideal case, the temperature responses should be completely independent of droplet locations, whereas the voltage responses should also be insensitive (<1% change, see 6.3.1 for details).

Figure 6.12 shows the simulated temperature and voltage responses. As we can see, both the temperature and voltage responses are indeed insensitive to droplet locations. The voltage responses are subject to a relatively larger variation, but still within 0.03% change. This relatively larger variation is mostly caused by the different contribution of metal resistance at different droplet locations, which can be further eliminated by a linear de-trending.

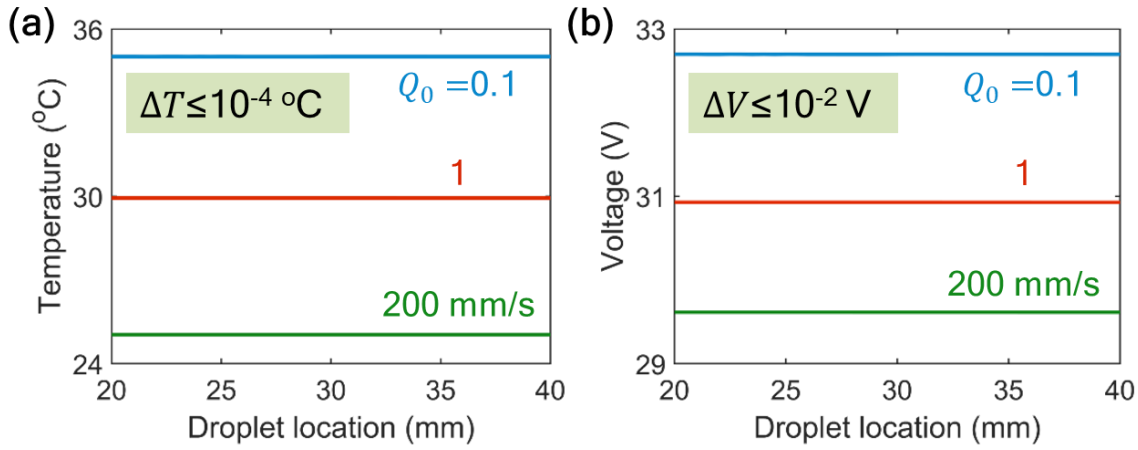

Figure 6.12. Temperature (a) and voltage (b) responses of fiber distributed sensors with droplet located at various locations.

Required lengthwise dimensions for accurate simulations

As we mentioned earlier, the inconsistence of voltage responses to droplet at different locations is directly related to the size of our simulated structures. To verify it and find out the minimum lengthwise dimensions required, we conducted a similar scan with a much longer segment of 6 cm. The temperature of CPE is set at constant room temperature to get the nominal resistance as a function of droplet location. The simulation results in Figure 6.13 perfectly match our expectation: the large resistance change only exists around two edges of the fiber. In a long segment of 6 cm (Figure 6.13b), we obtain a wide region from 15 mm to 45 mm where nominal resistance stays near constant. We further zoom in this region, and re-plot it in Figure 6.13c. As we can see, nominal resistance gradually increases at a constant rate of 20 Ω/m, or 0.21% per meter. This agrees with our lumped-element model in 6.3.1, where metal strips have a conductivity of 10^7 S/m and a cross-sectional area of 100x50 μm. At a location 15 mm away from the edge of fiber, nominal resistance drops to less than 0.005% off predictions from lumped-element model. Thus, the required lengthwise dimensions is 1.5 cm before and after active sensing region. For

example, to test a 2-cm-long distributed sensor, the lengthwise dimensions needs to be at least 5 cm.

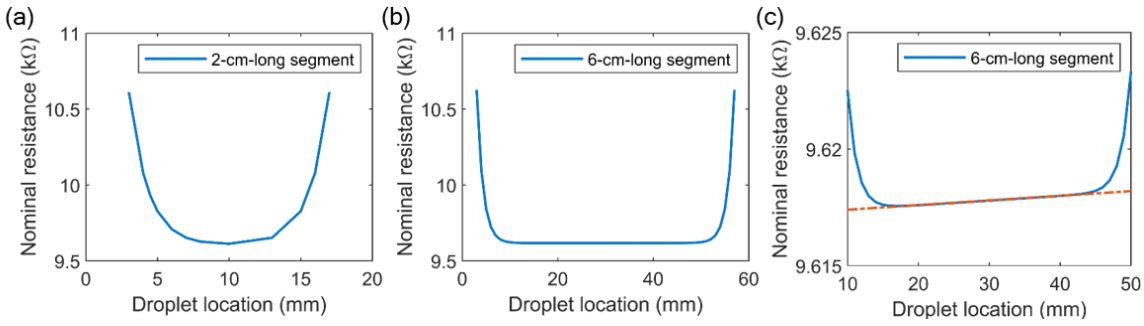

Figure 6.13. Dependence of nominal resistance on droplet location for (a) a 2-cm-long segment and (b, c) a 6-cm-long segment.

6.4.4 Demonstration of scanning flowrate distribution

For the final demonstration, we would like to show the scan of flow velocity distribution along the axial direction of the fiber. Figure 6.14 shows the simulation setup for such demonstration. A laminar flow profile is applied to the streaming fluid in the tank, with flow velocity to be $v = -0.036(x - 10)^2 + 1$ mm/s. The droplet slides from 5 mm to 15 mm to sense the flow velocity distribution within this region. Note that the droplet scan range is carefully chosen to minimize the effects from two edges of the fiber. Moreover, the flow velocity only varies from 0.1 to 1 mm/s within this scan range, matching the most sensitive region in Figure 6.11.

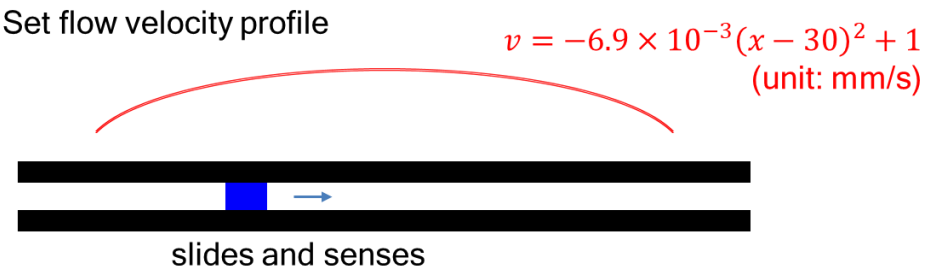

Figure 6.14. Simulation setup for scanning flowrate distribution.

Figure 6.15 shows simulated temperature and voltage profile. Each profile translates into a flow velocity profile independently using results we acquired in Figure 6.11. We plot the reconstructed flow profiles together with environment flow profiles in Figure 6.16. As we can see, all simulated points match local flow velocities near perfectly. In the profile reconstructed from sensor temperature (Figure 6.16a), the maximum error is below 0.05 mm/s. The relatively larger error from sensor temperature is caused by the way we extract temperature response: we use the maximum hot-film temperature as the temperature response. However, the maximum hot-film temperature does not occur at where the center of droplet locates when profiling a non-uniform temperature distribution. Instead, it occurs towards the side that has lower flow velocity, which causes the underestimated flow velocity in Figure 6.16a. Fortunately, for the profile translated from sensor voltage (Figure 6.16b), the maximum error is below 0.008 mm/s, or 1.4%, still demonstrating a good match and small uncertainty.

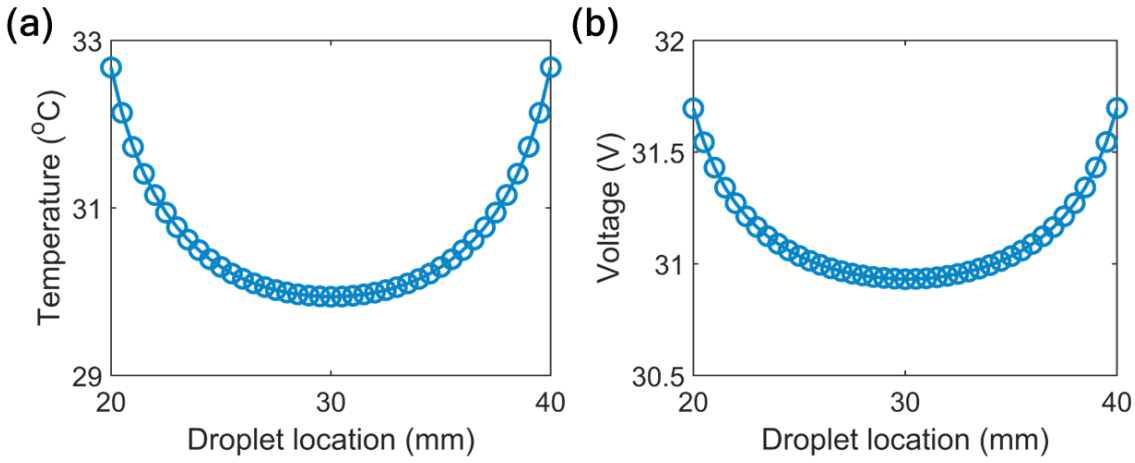

Figure 6.15. Measured (a) temperate and (b) voltage responses when scanning a laminar flow profile.

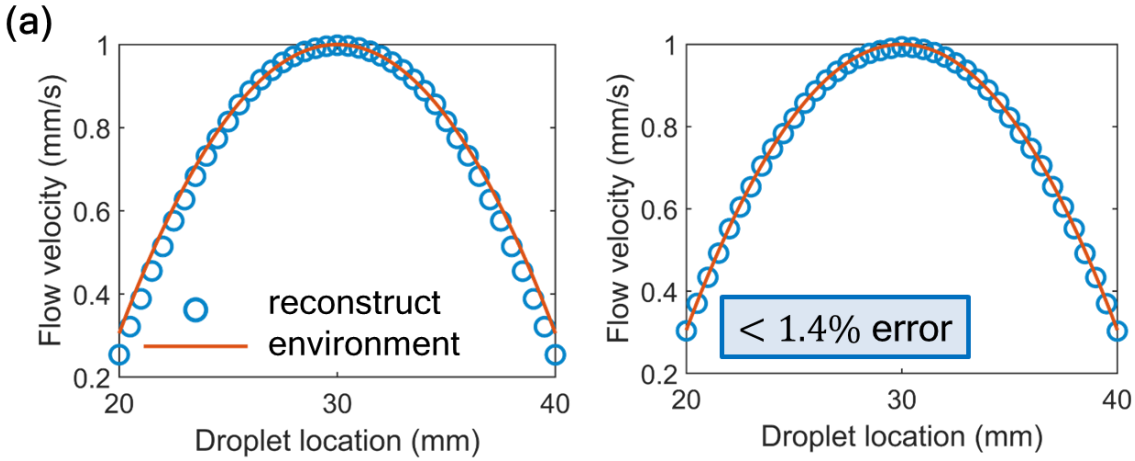

Figure 6.16. Original flow profile (red line) and reconstructed flow profile (circles) from measured temperature (left) and voltage (right) responses.

To conclude this chapter, we have demonstrated the concept of distributed flow sensors with FEM simulations. We reported mm-level spatial resolution, as well as 9% accuracy of flow velocities between 0.1 to 1 mm/s. A first-order current distribution theory is proposed to estimate spatial resolution, and also points out the direction for future

optimization. Voltage responses still suffer large error, which can be reduced by increasing lengthwise dimensions of simulated structures. Overall, we successfully demonstrated the soundness of electrically active distributed sensors for the first time, which opens up tremendous opportunities in developing novel distributed sensors.

Chapter 7: Conclusion

In this chapter, we conclude the entire dissertation and talk about electrically active microfluidic fibers altogether. We review the questions we asked in introduction, and answer them with the contents of this dissertation. For future work, we address remaining improvements to be done on current microfluidic fibers. Afterwards, we also propose a few new microfluidic fibers available based on the contents in this dissertation.

7.1 SUMMARY

Overall, this dissertation focuses on a hybrid technology called electrically active microfluidic fibers, which marry microfluidics and multimaterial fibers together (see Figure 7.1). This work starts by trying to find a better solution for fluidic chip-to-chip interconnects, where simple plastic tubing is currently used with no active functionalities integrated. As we add more and more units on those hollow fibers, we are excited to find out this novel devices enjoy the benefits from both microfluidics side and multimaterial fibers side. Furthermore, with this novel technology, we develop novel distributed sensors that do not exist before: electrically active fiber distributed sensors.

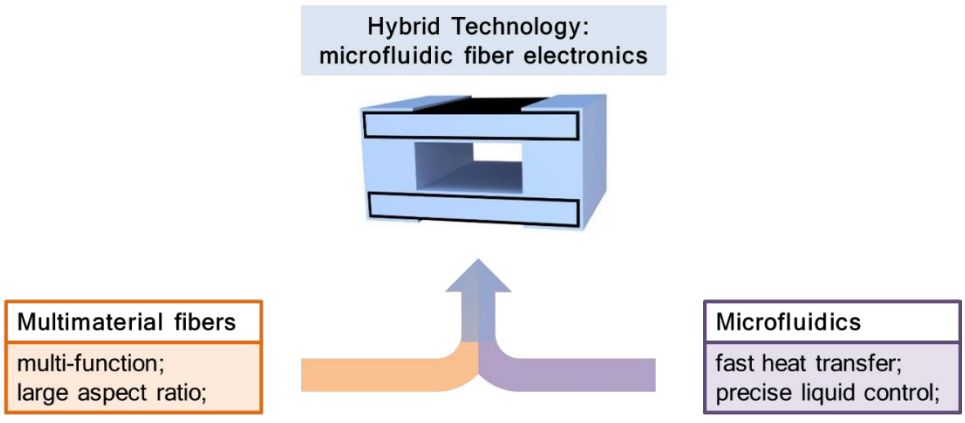

Figure 7.1. Electrically active microfluidic fibers as the marriage of multimaterial fibers and microfluidics.

Back to the questions we asked in Chapter 1, have we solved all of them?

The first question is "*Can microfluidic fibers form a closed-loop flow control system, i.e. a system consists of active flow controllers and flow monitors?*". We obviously proved it by using exactly the same device for both demonstrations of fiber flow sensor in Chapter 2 and fiber pumps in Chapter 3.

The next question is "*Can devices made with microfluidic fibers outperform state-of-the-art commercial sensors/actuators?*". The answer is yes. We demonstrated fiber flow sensors that exhibit record-setting flow sensitivity, with ultra-low pressure drop and less than 20 degree temperature rise. We also shown fiber pumps that behaves sub-100-ms initialization time and predictable flow response. All of those performances inevitably outperform state-of-the-art commercial sensors/actuators.

Then we asked "*Can microfluidic fibers, as a hybrid technology, marry the benefits from both microfluidics and multimaterial fibers?*". And the answer again is yes. We use fiber pumps (Chapter 2) to demonstrate precise liquid control and fiber flow sensors (Chapter 3) to demonstrate rapid heat transfer, both benefits are from microfluidics technology. Then we also use flow sensors optimization (Chapter 4) to show adjustable device length in axial direction and distributed sensors (Chapter 5) to show exceptional aspect ratio, both benefits are from multimaterial fibers.

The last question is "*Can microfluidic fibers, as a novel technology, offer new opportunities for sensing/actuating modalities that do not exist before?*". We use microfluidic fibers to demonstrate the first ever implementation of distributed sensing in electrically active fibers (Chapter 5). This device does not exist before.

Altogether, as a novel hybrid technology, electrically active microfluidic fibers pave the way towards a complete functional overhaul of microfluidics feed lines needed in

large-scale multi-chip integration in microfluidics and open new possibilities in lab-on-fiber technologies.

7.2 FUTURE WORK

7.2.1 Low voltage actuated fiber pumps

The minimum driving voltage for fiber pumps is 220 V, which is not safe for many biomedical applications. Thus developing low voltage actuated fiber pumps is of great interest to us. To provide enough pumping force at a low voltage, we need to create a thin and uniform dielectric layer to increase the interfacial capacitance (see 3.3.2). However, the dielectric layer we currently use, low-density polyethylene (LDPE), suffers a low melting temperature of 105~115 ^{o}C. It completely melts when we draw our fibers at 290 ^{o}C, which is necessary due to the high glass-transition temperature of cladding materials. As a result, we cannot create a thin and uniform dielectric layer adjacent to fluid channel. Instead, we add silicone oil to protect conductive polymeric films from shorting, which forms a thick protective layer that significantly brings down the interfacial capacitance.

To develop low voltage actuated fiber pumps, it is necessary to find new materials that is compatible with the thermal drawing of polycarbonate fibers. This new materials should also be hydrophobic for a large starting contact angle at zero potential.

7.2.2 Droplet-based flow injection with fiber pumps

All EWOD actuated micro pumps suffer the same problem: liquid can only be pumped into the system, and cannot be pumped out. From the thermodynamic standpoint (see details in 3.2.1), EWOD can only reduce contact angle instead of increasing it. Thus, net force always point inward to the fluid channel. From the electromechanical standpoint, electrostatic force always attract more liquid into the capacitor instead of pulling them out.

Fortunately, in a droplet-based system, we can overcome this fundamental challenge by switching on and off multiple (at least two) independent pumps connected in series, thanks to the exceptional aspect ratio of fibers. Here, we provide two possible configurations for such systems.

In Figure 7.2, three independent micro pumps are connected in series. The entire pumping process starts with the first droplet enters into fiber segment #1 while the second droplet already leaves fiber segment #1. We switch segment #1 on and continually pump the first droplet into the system until the second droplet enters segment #3. Then switch off segment #1 and switch on segment #3 until the first droplet enters segment #2. The last step is to switch segment #3 off and segment #2 on until the system evolves back to the start state of step 1. Such configuration requires uniform droplet distribution, which might be difficult to achieve in many applications.

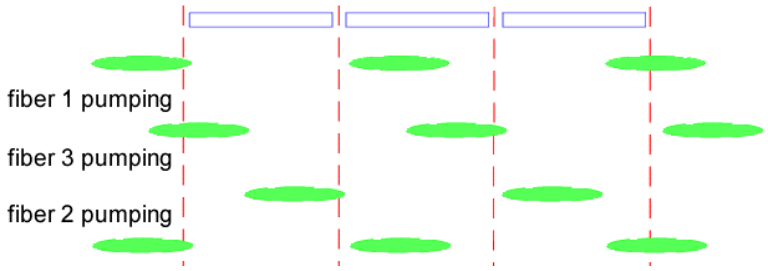

Figure 7.2. Configuration of droplet-based flow injection.

Alternatively, if we can segment the same piece of fiber into three independent pumps with negligible gaps between them, the requirements are much easier to accomplish. For example, the configuration shown in Figure 7.3 only requires the length of each droplet being larger than the length of each pump segment.

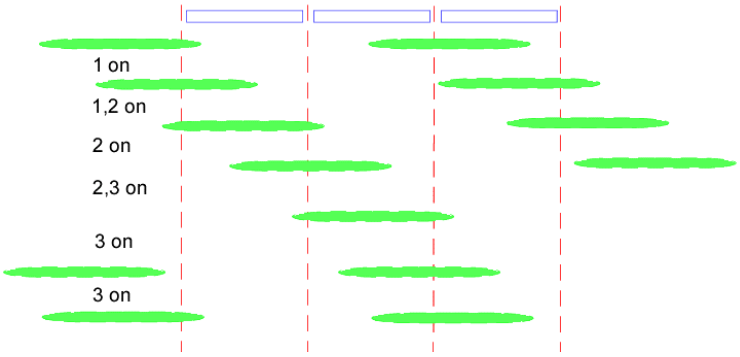

Figure 7.3. Alternative configuration of droplet-based flow injection.

7.2.3 Demonstration of two-segment flow sensors in experiments

In Chapter 5, we demonstrated the concept of two-segment flow sensors in FEM simulations, with the same dynamic range but much reduced number of surface contacts. Moreover, if external heater with constant temperature is allowed, we can significantly extend dynamic range by another 7x. Thus, a natural extension of flow sensor project would be the demonstration of two-segment flow sensors in experiments.

7.2.4 Demonstration of distributed flow sensors in experiments

In Chapter 6, we demonstrated the concept of distributed flow sensors with sub-cm spatial resolution, which is the first electrical distributed sensors. Future work can be conducted to demonstrate it in experiments.

7.2.5 Other forms of distributed sensors

In section 6.2.3, we introduced four possible forms of distributed sensors, and focused on the potential applications of distributed thermal sensors and distributed flex sensors. Future work can be carried out around those sensors, especially distributed flex sensors. Distributed flex sensors have great potential in gaming industry as wearable game controllers.

Other distributed sensors, such as distributed flow sensors, distributed impedance sensors, distributed acoustics sensors, also have many applications in biomedical devices. Many biomedical instruments require the measurement of tomography, where distributed sensors can be greatly useful. For example, distributed flow sensors can be applied in velocimetry; distributed impedance sensors are favorable for complete blood count; and distributed acoustics sensors can highly benefit high-resolution ultrasound imaging.

7.2.6 Alternative methods of breaking axial uniformity

Our proposed distributed sensors utilize a droplet to break axial uniformity, which is an effective method but can be slow in a long segment. Inspired by the fiber Bragg grating in optical fiber, we here proposed some similar strategies for electrical fibers.

One way to create such periodic pattern on electrical fibers is by laser cutting. We noticed that the cladding materials polycarbonate is mainly transparent between 450~1000 nm, whereas the conductive polymeric films CPE have a strong absorption within this range. Thus, a white-light laser can selectively cut off black CPE films without affecting transparent cladding material. A periodic pattern can be obtained by switching a pulsed laser on and off during thermal drawing process.

Alternatively, we can break axial uniformity with an electrical method: droplet-based electroplating. Conventionally, it is rather difficult to create uniform or patterned metal films on the inner surfaces of a hollow fiber. To address this challenge, we can create hollow fibers with CPE films adjacent to the inner surfaces. Then droplets that contain electrolyte pass through the inner channel at a constant speed. By carefully setting up the electrical current pulse, we can deposit metal films on the surface of CPE films with designed pattern.

7.3 FINAL REMARKS

I do not know if anyone will ever read this section. Nevertheless, if you do, whether I know you or not, I would like to express my deepest appreciation for your interest. It is also my sincerest hope that you read this dissertation because you would like to continue the work I addressed here.

I started my research in 2014 with the project of fiber pumps. At that point, I had no clue about the applications this work would eventually fit in. Through my perennial and reckless optimism in science and engineering, I continued to fabricate and optimize those pumps aimlessly. In the summer of 2015, I proposed the project of fiber flow sensors, and assigned it to one of my mentees, Corey. His diligence and hard-work resulted in very promising results for this project. And it was not until then that I started realizing the opportunities of electrically active microfluidic fibers. The possibility of forming a closed-loop flow control system got me excited, and drove me to think more about developing novel devices that did not exist before. Then it came droplet-enabled distributed sensors.

Now that I look back, I cannot say that the work I have done have the same reach as I intended originally. Nevertheless, although I was not sure about the scope of this dissertation when I started, after many years of continuous work, it inevitably found me. At the end, I would like finish this dissertation with a Chinese poem:

回首向来萧瑟处，也无风雨也无晴。 --- 苏轼

References

[1] Y. Liu and X. Jiang, "Why microfluidics? Merits and trends in chemical synthesis," *Lab Chip*, vol. 17, no. 23, pp. 3960–3978, Nov. 2017.

[2] J. C. T. Eijkel and A. van den Berg, "Nanofluidics: what is it and what can we expect from it?," *Microfluid Nanofluid*, vol. 1, no. 3, pp. 249–267, Jul. 2005.

[3] C. J. Easley *et al.*, "A fully integrated microfluidic genetic analysis system with sample-in–answer-out capability," *PNAS*, vol. 103, no. 51, pp. 19272–19277, Dec. 2006.

[4] P. Liu and R. A. Mathies, "Integrated microfluidic systems for high-performance genetic analysis," *Trends in Biotechnology*, vol. 27, no. 10, pp. 572–581, Oct. 2009.

[5] A. F. Abouraddy *et al.*, "Towards multimaterial multifunctional fibres that see, hear, sense and communicate," *Nature Materials*, vol. 6, no. 5, pp. 336–347, May 2007.

[6] F. Sorin and Y. Fink, "Multimaterial fiber sensors," presented at the Fourth European Workshop on Optical Fibre Sensors, 2010, vol. 7653, p. 765305.

[7] G. Tao, A. M. Stolyarov, and A. F. Abouraddy, "Multimaterial Fibers," *Int J Appl Glass Sci*, vol. 3, no. 4, pp. 349–368, Dec. 2012.

[8] L. Wei *et al.*, "Optoelectronic Fibers via Selective Amplification of In-Fiber Capillary Instabilities," *Adv. Mater.*, vol. 29, no. 1, p. n/a-n/a, Jan. 2017.

[9] M. Rein, E. Levy, A. Gumennik, A. F. Abouraddy, J. Joannopoulos, and Y. Fink, "Self-assembled fibre optoelectronics with discrete translational symmetry," *Nature Communications*, vol. 7, p. 12807, Oct. 2016.

[10] W. Yan *et al.*, "Semiconducting Nanowire-Based Optoelectronic Fibers," *Advanced Materials*, vol. 29, no. 27, p. 1700681, Jul. 2017.

[11] F. Sorin *et al.*, "Multimaterial Photodetecting Fibers: a Geometric and Structural Study," *Adv. Mater.*, vol. 19, no. 22, pp. 3872–3877, Nov. 2007.

[12] M. Bayindir, A. F. Abouraddy, J. Arnold, J. D. Joannopoulos, and Y. Fink, "Thermal-Sensing Fiber Devices by Multimaterial Codrawing," *Adv. Mater.*, vol. 18, no. 7, pp. 845–849, Apr. 2006.

[13] N. Chocat, G. Lestoquoy, Z. Wang, D. M. Rodgers, J. D. Joannopoulos, and Y. Fink, "Piezoelectric Fibers for Conformal Acoustics," *Advanced Materials*, vol. 24, no. 39, pp. 5327–5332, Oct. 2012.

[14] S. Egusa *et al.*, "Multimaterial piezoelectric fibres," *Nature Materials*, vol. 9, no. 8, pp. 643–648, Aug. 2010.

[15] B. Chen, C. Kwok, T.-A. N. Nguyen, and Z. Wang, "Integrated Fiber Flow Sensors for Microfluidic Interconnects," *Advanced Materials Technologies*, vol. 3, no. 11, p. 1800175, 2018.

[16] A. Canales *et al.*, "Multifunctional fibers for simultaneous optical, electrical and chemical interrogation of neural circuits *in vivo*," *Nature Biotechnology*, vol. 33, no. 3, pp. 277–284, Mar. 2015.

[17] P. Mach *et al.*, "Tunable microfluidic optical fiber," *Applied Physics Letters*, vol. 80, no. 23, p. 4294, 2002.

[18] J. Zhang *et al.*, “Laser-Induced In-Fiber Fluid Dynamical Instabilities for Precise and Scalable Fabrication of Spherical Particles,” *Advanced Functional Materials*, vol. 27, no. 43, p. 1703245, Nov. 2017.
[19] B. Lundberg and B. Sundqvist, “Resistivity of a composite conducting polymer as a function of temperature, pressure, and environment: Applications as a pressure and gas concentration transducer,” *Journal of Applied Physics*, vol. 60, no. 3, pp. 1074–1079, Aug. 1986.
[20] M. Narkis, A. Ram, and Z. Stein, “Effect of crosslinking on carbon black/polyethylene switching materials,” *J. Appl. Polym. Sci.*, vol. 25, no. 7, pp. 1515–1518, Jul. 1980.
[21] H.A. Stone, A.D. Stroock, and and A. Ajdari, “Engineering Flows in Small Devices,” *Annual Review of Fluid Mechanics*, vol. 36, no. 1, pp. 381–411, 2004.
[22] M. Piotto, M. Dei, and P. Bruschi, “Low pressure drop, CMOS compatible liquid flow sensor with sub ml/h resolution,” *Procedia Chemistry*, vol. 1, no. 1, pp. 96–99, Sep. 2009.
[23] Z. Li, S. Y. Mak, A. Sauret, and H. C. Shum, “Syringe-pump-induced fluctuation in all-aqueous microfluidic system implications for flow rate accuracy,” *Lab Chip*, vol. 14, no. 4, pp. 744–749, Jan. 2014.
[24] W. Zeng, I. Jacobi, D. J. Beck, S. Li, and H. A. Stone, “Characterization of syringe-pump-driven induced pressure fluctuations in elastic microchannels,” *Lab Chip*, vol. 15, no. 4, pp. 1110–1115, Feb. 2015.
[25] Y. Anis, J. Houkal, M. Holl, R. Johnson, and D. Meldrum, “Diaphragm pico-liter pump for single-cell manipulation,” *Biomed Microdevices*, vol. 13, no. 4, pp. 651–659, Aug. 2011.
[26] R. Yokokawa, T. Saika, T. Nakayama, H. Fujita, and S. Konishi, “On-chip syringe pumps for picoliter-scale liquid manipulation,” *Lab on a Chip*, vol. 6, no. 8, pp. 1062–1066, 2006.
[27] N.-T. Nguyen, X. Huang, and T. K. Chuan, “MEMS-Micropumps: A Review,” *J. Fluids Eng*, vol. 124, no. 2, pp. 384–392, May 2002.
[28] S. F. Bart, L. S. Tavrow, M. Mehregany, and J. H. Lang, “Microfabricated electrohydrodynamic pumps,” *Sensors and Actuators A: Physical*, vol. 21, no. 1, pp. 193–197, Feb. 1990.
[29] A. Richter and H. Sandmaier, “An electrohydrodynamic micropump,” in *IEEE Proceedings on Micro Electro Mechanical Systems, An Investigation of Micro Structures, Sensors, Actuators, Machines and Robots.*, 1990, pp. 99–104.
[30] D. J. Harrison, A. Manz, and P. G. Glavina, “Electroosmotic pumping within a chemical sensor system integrated on silicon,” in *, 1991 International Conference on Solid-State Sensors and Actuators, 1991. Digest of Technical Papers, TRANSDUCERS ’91*, 1991, pp. 792–795.
[31] H. Matsumoto and J. E. Colgate, “Preliminary investigation of micropumping based on electrical control of interfacial tension,” in *IEEE Proceedings on Micro Electro Mechanical Systems, An Investigation of Micro Structures, Sensors, Actuators, Machines and Robots.*, 1990, pp. 105–110.

[32] J. Lee and C. J. C. Kim, “Liquid micromotor driven by continuous electrowetting,” in *Proceedings MEMS 98. IEEE. Eleventh Annual International Workshop on Micro Electro Mechanical Systems. An Investigation of Micro Structures, Sensors, Actuators, Machines and Systems (Cat. No.98CH36176*, 1998, pp. 538–543.
[33] H.-W. Lu, F. Bottausci, J. D. Fowler, A. L. Bertozzi, C. Meinhart, and C.-J. “CJ” Kim, “A study of EWOD-driven droplets by PIV investigation,” *Lab Chip*, vol. 8, no. 3, pp. 456–461, Feb. 2008.
[34] W. C. Nelson and C.-J. ‘CJ’ Kim, “Droplet Actuation by Electrowetting-on-Dielectric (EWOD): A Review,” *Journal of Adhesion Science and Technology*, vol. 26, no. 12–17, pp. 1747–1771, Sep. 2012.
[35] “Electrowetting,” *Wikipedia*. 10-Dec-2018.
[36] J. Lee, H. Moon, J. Fowler, T. Schoellhammer, and C.-J. Kim, “Electrowetting and electrowetting-on-dielectric for microscale liquid handling,” *Sensors and Actuators A: Physical*, vol. 95, no. 2, pp. 259–268, Jan. 2002.
[37] D. Brassard, L. Malic, F. Normandin, M. Tabrizian, and T. Veres, “Water -oil core-shell droplets for electrowetting-based digital microfluidic devices,” *Lab on a Chip*, vol. 8, no. 8, pp. 1342–1349, 2008.
[38] G. J. Shah, A. T. Ohta, E. P.-Y. Chiou, M. C. Wu, and Chang-Jin “CJ” Kim, “EWOD-driven droplet microfluidic device integrated with optoelectronic tweezers as an automated platform for cellular isolation and analysis,” *Lab on a Chip*, vol. 9, no. 12, pp. 1732–1739, 2009.
[39] F. Saeki, J. Baum, H. Moon, J. Yoon, C. “cj Kim, and R. L. Garrell, “Electrowetting on dielectrics (EWOD): Reducing voltage requirements for microfluidics, Polym,” *Mater. Sci. Eng*, pp. 12–13.
[40] C. Schaschke, *Fluid Mechanics: Worked Examples for Engineers*. IChemE, 2005.
[41] V. Peykov, A. Quinn, and J. Ralston, “Electrowetting: a model for contact-angle saturation,” *Colloid Polym Sci*, vol. 278, no. 8, pp. 789–793, Aug. 2000.
[42] A. Quinn, R. Sedev, and J. Ralston, “Contact Angle Saturation in Electrowetting,” *J. Phys. Chem. B*, vol. 109, no. 13, pp. 6268–6275, Apr. 2005.
[43] C. W. Extrand and Y. Kumagai, “An Experimental Study of Contact Angle Hysteresis,” *Journal of Colloid and Interface Science*, vol. 191, no. 2, pp. 378–383, Jul. 1997.
[44] J. F. Joanny and P. G. de Gennes, “A model for contact angle hysteresis,” in *Simple Views on Condensed Matter*, vol. Volume 12, 0 vols., WORLD SCIENTIFIC, 2003, pp. 457–467.
[45] K. L. Mittal, *Contact Angle, Wettability and Adhesion*. BRILL, 2009.
[46] P. Abgrall and A.-M. Gué, “Lab-on-chip technologies: making a microfluidic network and coupling it into a complete microsystem—a review,” *J. Micromech. Microeng.*, vol. 17, no. 5, p. R15, 2007.
[47] J. T. W. Kuo, L. Yu, and E. Meng, “Micromachined Thermal Flow Sensors—A Review,” *Micromachines*, vol. 3, no. 3, pp. 550–573, Jul. 2012.
[48] D. Wlodkowic and Z. Darzynkiewicz, “Rise of the micromachines: microfluidics and the future of cytometry,” *Methods Cell Biol.*, vol. 102, pp. 105–125, 2011.

[49] N. T. Nguyen, “Micromachined flow sensors—a review,” *Flow Measurement and Instrumentation*, vol. 8, no. 1, pp. 7–16, Mar. 1997.
[50] M. Dijkstra, M. J. de Boer, J. W. Berenschot, T. S. J. Lammerink, R. J. Wiegerink, and M. Elwenspoek, “Miniaturized thermal flow sensor with planar-integrated sensor structures on semicircular surface channels,” *Sensors and Actuators A: Physical*, vol. 143, no. 1, pp. 1–6, May 2008.
[51] S. Wu, Q. Lin, Y. Yuen, and Y.-C. Tai, “MEMS flow sensors for nano-fluidic applications,” *Sensors and Actuators A: Physical*, vol. 89, no. 1–2, pp. 152–158, Mar. 2001.
[52] J. T. W. Kuo, L.-Y. Chang, P.-Y. Li, T. Hoang, and E. Meng, “A microfluidic platform with integrated flow sensing for focal chemical stimulation of cells and tissue,” *Sensors and Actuators B: Chemical*, vol. 152, no. 2, pp. 267–276, Mar. 2011.
[53] K. R. King, C. Wang, J. P. Vacanti, and J. T. Borenstein, “Biodegradable Polymer Microfluidics for Tissue Engineering Microvasculature,” *MRS Proceedings*, vol. 729, p. U1.4, 2002.
[54] E. K. Sackmann, A. L. Fulton, and D. J. Beebe, “The present and future role of microfluidics in biomedical research,” *Nature*, vol. 507, no. 7491, pp. 181–189, Mar. 2014.
[55] K. W. Kwon *et al.*, “Separation of Human Breast Cancer and Epithelial Cells by Adhesion Difference in a Microfluidic Channel,” *Journal of Semiconductor Technology and Science*, vol. 7, no. 3, pp. 140–150, Sep. 2007.
[56] M. Elwenspoek and R. Wiegerink, *Mechanical Microsensors*. Springer Science & Business Media, 2012.
[57] A. D. Pancrazio, P. Bruschi, and M. Piotto, “Low power, MEMS liquid flow sensor with silicone coating electrical insulation,” in *2014 Symposium on Design, Test, Integration and Packaging of MEMS/MOEMS (DTIP)*, 2014, pp. 1–4.
[58] P. Fürjes, G. Légrádi, C. Dücső, A. Aszódi, and I. Bársony, “Thermal characterisation of a direction dependent flow sensor,” *Sensors and Actuators A: Physical*, vol. 115, no. 2–3, pp. 417–423, Sep. 2004.
[59] C. E. O’connell-Rodwell *et al.*, “A genetic reporter of thermal stress defines physiologic zones over a defined temperature range,” *FASEB J*, vol. 18, no. 2, pp. 264–271, Feb. 2004.
[60] “COMSOL Multiphysics® Modeling Software.” [Online]. Available: https://www.comsol.com/. [Accessed: 11-May-2018].
[61] A. Barrias, J. R. Casas, and S. Villalba, “A Review of Distributed Optical Fiber Sensors for Civil Engineering Applications,” *Sensors (Basel)*, vol. 16, no. 5, May 2016.
[62] T. Sperber, A. Eyal, M. Tur, and L. Thévenaz, “High spatial resolution distributed sensing in optical fibers by Brillouin gain-profile tracing,” *Opt. Express, OE*, vol. 18, no. 8, pp. 8671–8679, Apr. 2010.
[63] “Distributed temperature sensing,” *Wikipedia*. 17-Mar-2018.

[64] X. Bao and L. Chen, “Recent Progress in Distributed Fiber Optic Sensors,” *Sensors*, vol. 12, no. 7, pp. 8601–8639, Jul. 2012.
[65] M. Froggatt and J. Moore, “High-spatial-resolution distributed strain measurement in optical fiber with Rayleigh scatter,” *Appl. Opt., AO*, vol. 37, no. 10, pp. 1735–1740, Apr. 1998.
[66] W. W. Morey, G. Meltz, and W. H. Glenn, “Fiber Optic Bragg Grating Sensors,” in *Fiber Optic and Laser Sensors VII*, 1990, vol. 1169, pp. 98–108.